



# Universidad de Navarra

## Facultad de Ciencias

**Colloidal Phase Transition Dynamics**

Raheema M. Aslam





Universidad de Navarra  
School of Science

**Colloidal Phase Transition Dynamics**

Submitted by **Raheema M. Aslam** in partial fulfillment of the requirements for the Doctoral Degree of the University of Navarra

This dissertation has been written under my supervision in the Doctoral Program in Complex Systems, and I approve its submission to the Defense Committee.

Signed on January 26, 2016

Dr. Wenceslao González-Viñas



Declaración:

Por la presente yo, **Dª. Raheema M. Aslam**, declaro que esta tesis es fruto de mi propio trabajo y que en mi conocimiento, no contiene ni material previamente publicado o escrito por otra persona, ni material que sustancialmente haya formado parte de los requerimientos para obtener cualquier otro título en cualquier centro de educación superior, excepto en los lugares del texto en los que se ha hecho referencia explícita a la fuente de la información.

(I hereby declare that this submission is my own work and that, to the best of my knowledge and belief, it contains no material previously published or written by another person nor material which to a substantial extent has been accepted for the award of any other degree of the university or other institute of higher learning, except where due acknowledgment has been made in the text.)

De igual manera, autorizo al Departamento de Física y Matemática Aplicada de la Universidad de Navarra, la distribución de esta tesis y, si procede, de la "fe de erratas" correspondiente por cualquier medio, sin perjuicio de los derechos de propiedad intelectual que me corresponden.

Signed on January 26, 2016

Raheema M. Aslam

© Raheema M. Aslam

Derechos de edición, divulgación y publicación:

© Departamento de Física y Matemática Aplicada, Universidad de Navarra



To my great mother  
Bakhtawar



## Acknowledgements

I would like to express my special appreciations and thanks to my supervisor Prof. Wenceslao González-Viñas for his tremendous encouragement, advice and support in my research. His dedicated efforts on my research as well as on my career have been priceless. Without his supervision and constant help this dissertation would not have been possible.

My sincere thanks to the staff members and Professors of the Department of Physics and Applied Mathematics for their cooperation, support and teaching during this period. My special thanks to Dr. M. Pichumani for his tremendous support. I would like to appreciate Silvia Olza and LuisFer Urrea for their technical support in time. I should mention the tremendous help and unconditional encouragement of my friends and PhD fellows, who have always been available during the needed time. I would like to thank Prof. J. Ramón Isasi and Unai Galech from University of Navarra for their generous help and loan of DLS. I strongly acknowledge Dr. M. López and Prof. J. Burguete for their assistance with PIV analysis and for providing Gaussimeter. My sincere thanks to Prof. J.J. Irigoyen and T. Kizildeniz from University of Navarra for their generous loan of Spectrophotometer (CM-2500d, SpectraMagic.NX). My sincere thanks to Dr. M.A. Miranda, Claudia, Hugo and T. Kizildeniz for reading deeply different parts of this thesis to correct grammatical and sentence errors. I would especially like to thank Prof. J. de Vicente (University of Granada, Spain) for providing carbonyl iron particles and for his collaboration in the study of Magnetorheology project.

Last but not the least, many thanks go to the Soft Matter group of Memorial University of Newfoundland, Canada: Prof. A. Yethiraj, Payam Bagheri, Swomitra, Zena Aljabal, Tatsuo Izawa and Somayeh who supported me a lot during my visit at Memorial University. I would like to express my special thanks to Prof. A. Yethiraj for his kind support and collaboration during my stay at Memorial University.

Especial thanks go to University of Navarra, Faculty of Science and Department of Physics and Applied Mathematics which provide me a ground for pursuing this research; to the “Asociación de Amigos de la Universidad de Navarra” for financial support and moral guidance to carry out this thesis work. My strong gratitudes to the Spanish Government national research projects, FIS2011-24642 and FIS2014-54101-P that helped to perform experiments and to share our results to the international research groups.

Lastly, it would not be possible for me to carry out this task without the prayers and the continuous encouragement of my family that, despite the distances support to achieve this goal. I would like to express my special thanks to all my family members. I deliver a lot of thanks to my friends: Hena, Kashif, Nazia, Iqra, Rubab, Ghulam Murtaza and Tefide who made my stay in Pamplona a second home. Personally, I would like to express my deepest gratefulness to Muhammad Iqbal for his moral motivation and encouragement. I would like to thank Prof. Maria Jesus and Prof. M. Carmen for showing the natural beauties of Navarra and the surroundings.

All my gratitude is also going to the referee Dr. M. Pichumani for spending his precious time for reviewing the thesis. His precious contribution has increased significantly the quality of the thesis. I appreciate particularly all jury members for the precise and efficient reviewing of the complete thesis they will perform for the defense.



Yesterday I was clever, so I wanted to change the world.  
Today I am wise, so I am changing myself.

Rumi,



# Contents

Preface	xiii
Glossary	xvii
<b>1. General Introduction</b>	<b>1</b>
1.1. Some control parameters in colloidal systems . . . . .	1
1.2. Electrowetting . . . . .	2
1.3. Rosensweig instability in ferrofluids . . . . .	3
1.4. Hydrophobic and Hydrophilic surfaces . . . . .	4
<b>I Vertical deposition-like configuration of colloidal systems</b>	<b>5</b>
<b>2. Introduction</b>	<b>7</b>
2.1. Vertical Deposition-like Configuration (VD) . . . . .	7
2.1.1. Evaporation . . . . .	8
2.2. Electric Double Layer (EDL) . . . . .	9
2.3. Electrokinetics . . . . .	9
2.3.1. Electrophoresis . . . . .	10
2.3.2. Electroosmosis . . . . .	11
2.4. Electrowetting theory . . . . .	12
2.4.1. AC electrowetting . . . . .	13
<b>3. Experimental Setup</b>	<b>15</b>
3.1. Materials . . . . .	15
3.2. Experimental system . . . . .	15
3.3. Cleaning procedure . . . . .	16
3.4. Experiments at room temperature . . . . .	17
3.4.1. Characterization . . . . .	18
3.4.2. Electrokinetic characterization . . . . .	18
3.4.3. Evaporation characterization . . . . .	19
3.4.4. Particle Image Velocimetry . . . . .	19
3.4.5. Short term closed flows and PIV analysis . . . . .	22
3.4.6. Long term flows and PIV analysis . . . . .	22
3.5. Experiments at higher temperatures . . . . .	23

3.5.1. Characterization . . . . .	25
<b>4. Results and Discussions</b>	<b>27</b>
4.1. Low evaporation and evolution of clusters . . . . .	27
4.1.1. Discussion . . . . .	28
4.1.2. Behavior of clusters . . . . .	33
4.2. High evaporation and colloidal deposits . . . . .	35
4.2.1. Discussion . . . . .	37
4.2.2. Mechanisms . . . . .	40
<b>II Spin-coating of colloidal systems</b>	<b>43</b>
<b>5. Introduction</b>	<b>45</b>
5.1. Spin-coating basics and theory . . . . .	45
5.2. Spin-coating of colloids . . . . .	47
5.3. Colloids under shear stress . . . . .	50
<b>6. Experimental Setup</b>	<b>53</b>
6.1. Magnetorheology experiments . . . . .	53
6.1.1. Materials . . . . .	53
6.1.2. Experimental system . . . . .	56
6.1.3. Experiment . . . . .	56
6.1.4. Measurements . . . . .	57
6.2. Spin-coating of colloids on photo-patterned substrate . . . . .	58
6.2.1. Surface treatment and hydrophilic substrates . . . . .	59
6.2.2. Suspension . . . . .	59
6.2.3. Experiments . . . . .	59
6.2.4. Characterization of spin-coated deposit . . . . .	59
6.2.5. Surface treatment and hydrophobic substrates . . . . .	61
<b>7. Results and Discussions</b>	<b>63</b>
7.1. Magnetorheology of hybrid colloids by spin-coating . . . . .	64
7.1.1. Simple model for magnetorheology of colloids by spin-coating . . . . .	68
7.1.2. Model for the magnetorheology of mixture or hybrid colloids . . . . .	69
7.2. Spin-coating of colloids on a photo-patterned substrate . . . . .	73
7.2.1. Structural analysis of spin-coated films . . . . .	75
7.2.2. Effect of the scaling spacing geometry of patterning . . . . .	79
<b>Conclusions and Outlook</b>	<b>83</b>
<b>Bibliography</b>	<b>85</b>
<b>Summary</b>	<b>95</b>
<b>Resumen</b>	<b>96</b>

# Preface

At ICTP (Italy), while doing postgraduate in theoretical condensed matter physics, I got an opportunity to attend several scientific conferences, workshops and schools including those based on experimental work. In this way, my interest developed to observe in-situ those imaginative physical systems that I were studying theoretically. ICTP played an important role for recognizing my strength, abilities and motivated to choose experimental research as a career. There are two reasons for pursuing PhD in experimental colloidal systems. First, these systems are an excellent experimental framework to test the fundamental physics of theoretical models for hard spheres atomic-like systems. Secondly, I could bring this knowledge to my home country Pakistan, where it would be easy to integrate this research in the laboratory. As for establishing this research, the experimental set-ups are simple, relatively cheap and efficient in the scientific community.

## Objectives

The aim of this work is to study the colloidal phase transition dynamics, using two different experimental setups, at different conditions and time scales, involving evaporation of the solvent. Those experimental setups are: vertical deposition like configuration (VD, large time scale) and spin-coating (SC, short time scale).

The conditions for VD experimental setup are: to observe phase transitions in diluted colloidal suspensions of negatively charged particles, in weak AC fields at different temperatures. At low evaporation (room temperature), the objectives are: on the one hand, to study the effect of initial particle concentrations on phase transition (from liquid phase to clusters evolution) in the meniscus region. As well as to investigate in depth the flow dynamics involved in the phase transitions with PIV analysis. On the other hand, at higher evaporation (higher temperatures) the main goal is to correlate clusters with columns formation in the phase transition (from liquid phase to dried deposit) at various external field strengths [1].

The conditions for SC experimental setup are: to make colloidal thin films at very short time scales in such a way that the fluid is made to evaporate very fast. On the one hand, with SC technique we perform experiments in magnetic fields using diluted magnetic colloids. The main goal is to extend generalized magneto-rheology by spin-coating to both suspensions of ferromagnetic particles and hybrid colloids at different experimental conditions: for a range of spinning velocities (2000 to 7000 rpm) and magnetic fields (0.05 to 72.7 mT). On the other hand, spin-coating of concentrated colloidal suspension yields polycrystalline deposit where the microscopic domains are arranged in radial orientational registry due to the axial symmetry imposed by spin-coating [2]. We make colloidal films using concentrated suspension of nonmagnetic colloidal particles by

spin-coating on photo-patterned substrates. The objective is to introduce a very simple technique in order to improve the quality of colloidal monolayer polycrystals by spin-coating without appearance of axial symmetry, at various experimental conditions that include: the influence of scaling spacing of the patterning on the structural order of colloidal films. The obtained structures are analyzed in depth with bond orientational order parameters [3] and with Minkowski structure metrics [4].

## Colloidal structure formation

Research in colloidal structure formation has attracted many groups from the scientific and technological community because of its promise to new and advanced materials in optoelectronics and photonics [5]. Yablonovitch [6] reported the existence of photonic bandgap in a three dimensional periodic structure which is called photonic crystal. Besides, their technological applications, colloidal systems provide an excellent experimental framework to analyze basic theoretical models for hard spheres atomic-like systems in order to study defect formation and their dynamics.

Various techniques have been used to obtain well ordered dried structures of colloidal systems for several years. The main purpose was to obtain colloidal structure over large area and to avoid the defects in these structure. These methods involve the transition from a fluid suspension to the dried structure which is finally controlled by a balance between the capillary forces and the interaction forces between the particles and with their surroundings. Some popular methods are those inspired from Langmuir-Blodgett method [7] that are based on the evaporation of the solvent. In this method colloidal particles deposit on the substrate which is immersed vertically in colloidal suspension as a result of phase transition (from liquid phase to solid phase). In this out-of-equilibrium phase transition, the important parameter involved is the time scale at which the transition takes place. This time period may be large or short depending on the liquid phase to evaporate from the dispersion and transform it to a solid state which can determine the final structure.

## Scope

Well-ordered colloidal structure can be achieved if the systems is closer to thermal equilibrium allowing the fluid phase to evaporate slowly. Understanding of the mechanisms involved in the dynamics of these transition is a key parameter to control the process of structure formation. In colloidal systems which are far-from-equilibrium, phase transition can allow to control final structure formation by applying the external forces. The external forces include: a thermal gradient, an electric field, a magnetic field, gravity or rotation, among many others. Here, during the phase transition (from liquid phase to solid phase) of colloidal suspension, we apply an external force. This external force induced deposition of colloidal particles will advance the structure formation process and will make more easy the fabrications of the multiple-scale structured materials. With this small modification we can prepare materials that are necessary for the technological applications with less economy. Thus, this new technology will be accessible to every one in the field.

In this work, we investigate the out-of-equilibrium phase transition in colloidal systems of

---

various physical-chemical properties when external forces are applied.

## Outline

In the introductory chapter 1, the contents of general physics of colloidal systems are briefly introduced. This thesis is composed of two parts, each part encloses the subject of the study dealing with two different experimental setups. The first part starts with an introductory chapter which briefly reviews the main characteristic of colloidal systems of charged particles in external fields in vertical deposition-like configuration. In this part the following two chapters presents the detailed description of the experimental setup and results and discussions. The second part focuses on the spin-coating experimental setup. In its introductory chapter, I review the basics and the theory of spin-coating method including the contents for spin-coating of colloids. Then, two different experimental setups and procedures are explained in detail in the following chapter to carry out spin-coating experiments with and without magnetic fields. The last chapter presents results and discussions relative to spin-coating experiments. Lastly, the conclusions and the outlook compile the obtained objectives and outline the future work.



# Glossary

$\nu_c$	Critical frequency
$\varsigma$	Conductivity
$Re$	Reynolds number
$Ca$	Capillary number
$Pe$	Péclet number
$\sigma$	charge density
$\eta$	Absolute viscosity
$\epsilon$	Permittivity
$\gamma$	Surface tension
$\theta_Y$	Young's equilibrium contact angle
$\epsilon$	Permittivity
$\tau_{rz}$	Shear stress
$\nu$	Kinematic viscosity
$UV$	Ultraviolet
$u$	Velocity
$V$	Voltage
$VD$	Vertical Deposition
$SC$	Spin-coating
$DC$	Direct current
$1 - d$	one dimensional
$2 - d$	two dimensional
$3 - d$	three dimensional
$px$	pixel
$AC$	Alternating current
$AWG$	Arbitrary Waveform Generator
$\bar{\lambda}$	Mean characteristic length between the clusters
$\varepsilon^2$	Occupation factor
$C$	Concentration
$E$	Evaporation
$\omega$	Rotation rate
$rpm$	Rotation per minute
$\zeta$	Zeta potential
$CEH$	Compact equivalent height
$\kappa^{-1}$	Debye length



# Chapter 1

## General Introduction

### Stability of Colloidal suspensions

Simple colloidal systems are composed of hard-spherical particles of diameter in the range of 10 nm to 10  $\mu\text{m}$  suspended in liquids (water, ethanol, ethylene glycol or mixture of them, for example the mixture of ethanol and water). Colloidal particles almost have larger densities than the suspended fluids that cause sedimentation because of gravity. Also, the inter-particles interaction forces such as electrostatic London-Van der Waals attractive forces result into accumulation or clustering [8]. In order to avoid agglomeration and sedimentation and to achieve stability of colloidal suspension, particles with dominating repelling force between them are prepared. This force stabilizes the suspension for larger periods than the experimental time-scales. On the basis of repulsive force two mechanisms of the colloids stability are commonly used: electrostatic and polymeric stabilization of colloids. Moreover, one of the most important parameter that describes the phase behavior of colloidal hard-sphere particles is the concentration or the volume fraction of particles. Generally, in diluted colloidal suspensions, the particles are supposed to be far from each other and can not easily interact.

### 1.1. Some control parameters in colloidal systems

Normally, real colloidal systems are more complex than hard spheres systems as other interaction forces also exist between them along with short range repulsive forces. These interaction forces also have critical importance to study phase transition dynamics in colloidal systems. Some of those control parameters or the interaction forces include: forces between colloidal particles and solvent and inter-particle forces.

- Viscous force on a particle dragging with a velocity  $u$  through a medium of viscosity  $\eta$  is  $\eta\sigma u$  (in order of magnitude), where  $\sigma$  is a representative length (e.g. particle diameter) [9].
- Brownian force determines the thermal energy of molecular chaos. It is  $K_B T/\sigma$  (in order of magnitude), where  $\sigma$  is the same as before,  $K_B$  is the Boltzmann constant<sup>1</sup>,  $T$  is absolute temperature [10].

---

<sup>1</sup> $K_B = 1.3806 \times 10^{-23} \text{ m}^2 \text{ kg s}^{-2} \text{ K}^{-1}$

- The London-Van der Waals attractive forces are inter-particle interaction forces of colloidal dispersion that cause aggregation for colloidal particles. To estimate these forces, the contribution over Van der Waals forces from all pairs of molecules of different particles is considered [11]. It is  $H\sigma/h$  (in order of magnitude) for small separations between particles, where  $H$  is Hamaker constant which depends on the nature of the particles and the suspended medium [11] and  $h$  is the separation between two particles ( $\sigma$  is the same as defined before).
- Electrostatic double-layer forces are the repulsive forces that may stabilize colloidal systems against the Van der Waals attractive forces [12–14]. In colloids the particles are electrically charged which is balanced by an opposite charge in the surrounding fluid. The particles gain negative electric charge when negatively charged ions of the dispersed medium are adsorbed on the particles surface. A negatively charged particle attracts the positive counterions surrounding the particle. These ions gather in the electric double layer around the particle (see Fig. 1.1). The electric potential decreases across the electric double layer. This voltage drop is called zeta potential that is an important parameter for a colloidal system and strongly depending on the colloids properties.



Figure 1.1: A schematic representation of electric double-layer on the particle surface of a colloidal system. © from Colloidal Dynamics LLC.

- DLVO (Deryagin, Landau, Vewey and Overbeek) theory explains the stability of colloidal systems. This theory describes the interaction between two approaching particles by combining the attractive van der Waals force and repulsive electrostatic double-layer force [15]. According to DLVO theory, a potential barrier resulting from the repulsive force forbids two approaching particles to adhere with each other. On the other hand, if the particles collide with sufficient energy to exceed that barrier, the Van der Waals attractive force will support them to accumulate with each other.

## 1.2. Electrowetting

Electrowetting is a phenomenon related to electric field-induced wetting properties of a conducting liquid droplet on a solid electrode. An electrowetting experimental set up is composed of a conducting liquid droplet on a metal electrode that sandwich a thin layer of insulator and works as a parallel plate capacitor. The application of a constant potential decreases the contact angle of the conducting droplet that results in a distribution of charge which changes its free energy [16–18]. Therefore, the droplet wets the surface of electrode. Electrowetting theory explains this change in the contact angle of a liquid droplet on homogeneous substrates by applying a voltage.

We follow the Verheijen and Prins [16] electrowetting theory that is based on the principal of virtual displacement of charge and assuming the system in the equilibrium at constant potential. The equation for electrowetting is derived (for further details see 2.4) as

$$\cos \theta(V) = \cos \theta_Y + \frac{\epsilon_0 \epsilon_r}{2d\gamma_{LV}} V^2 \quad (1.1)$$

where  $\theta(V)$  is the mean contact angle at applied voltage ( $V$ ),  $\theta_Y$  is Young's equilibrium contact angle at zero voltage,  $\epsilon_0$  is the permittivity of the free space,  $\epsilon_r$  is the relative permittivity of the insulating layer,  $\gamma_{LV}$  is the surface energy of liquid-vapor interface at zero voltage and  $d$  is the thickness of the insulating layer. Eq. 1.1 can be expressed as a function of dimensionless electrowetting number  $\eta = \frac{\epsilon_0 \epsilon_r}{2d\gamma_{LV}} V^2$ , that measures the strength of stored electrostatic energy with respect to surface tension depending on the thickness and properties of insulating layer [19].

### 1.3. Rosensweig instability in ferrofluids

Ferrofluids are colloids composed of nanoscale ferromagnetic particles in a carrier fluid. They have strong interaction with magnetic fields and become strongly magnetized in the presence of a magnetic field. The free surface of the ferrofluid experiences a transition from a flat surface to a stationary pattern of surface spikes above a certain threshold of an applied normal magnetic field. This instability is known as normal field instability or the Rosensweig instability [20–22]. Fig. 1.2 shows a periodical peak-shaped structure which is formed on the fluid surface when the applied magnetic field exceeds a critical value. The new free surface of the layer indicates a modified static state. Cowley *et al.* were the first who observed this phenomenon experimentally [20]. Later on, Rosensweig instability was investigated analytically and numerically assuming a uniform ferromagnetic particle distribution in the bulk of the magnetic fluid for any applied field intensity [23]. This unique property of ferrofluids to change shape and retain properties of a liquid when a magnetic field is applied, allows them to be utilized in a wide range of technological applications. For example, it is used in the loudspeaker technology for better power handling and audio response.

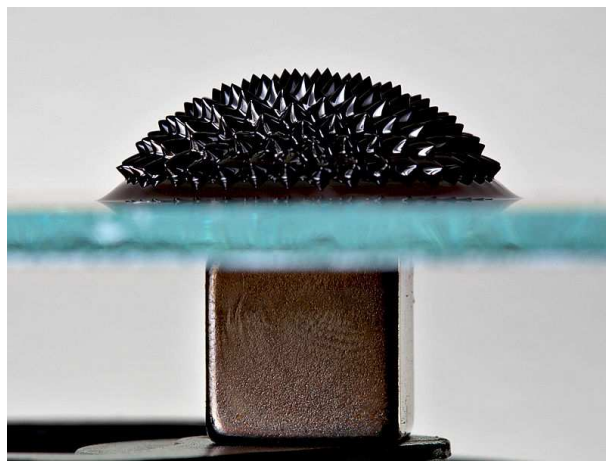


Figure 1.2: Ferrofluid in a normal magnetic field showing normal-field or Rosensweig instability caused by magnet beneath the glass. © from Wikimedia Commons by G.F.Maxwell.

## 1.4. Hydrophobic and Hydrophilic surfaces

Different surfaces (solids) have various wetting characteristics. The behavior of water on solid surface is commonly used for classifying a variety of different solids. The terms hydrophilic surface and hydrophobic surface have been well known in the literature for several decades [24]. Hydrophilic surface has strong affinity to water or other polar liquids whereas hydrophobic surface repel water.

The phrase hydrophobicity comes from the two Greek words; hydro (water) and phobos (fear or does not like it) and it was firstly assigned to the property of molecules. Hydrophobic surface resists water therefore a water droplet exhibits a large contact angle on it. For hydrophobic surface, the contact angle is assumed to be at least  $90^\circ$  or larger. We use ITO coated substrates of hydrophobic character (contact angle larger than  $90^\circ$ ) for all vertical deposition experiments.

Hydrophilic surfaces are those which wet a water droplet completely, visually having  $0^\circ$  contact angle (superhydrophilic surfaces) or less than  $90^\circ$  [24]. Here, for all spin-coating experiments in magnetic fields, substrates with hydrophilic character are used. We use piranha solution for cleaning the substrate to preserve its wetting characteristics as well as to remove any impurity such as moisture, dust and airborne organics.

## Part I

# Vertical deposition-like configuration of colloidal systems



# Chapter 2

## Introduction

### 2.1. Vertical Deposition-like Configuration (VD)

Different techniques have been used to obtain well ordered dried structures of colloidal systems at the mesoscopic characteristics scales since long [2, 25–28]. Those ordered materials have a large number of technological applications such as sensors, optical coatings, storage devices, optoelectronic devices [29, 30]. Vertical deposition method introduced by Colvin *et al.* [26], is one of the simplest and low cost methods and is well known in the scientific community for fabricating colloidal mono-layer or multi-layers films. In VD method involving evaporation of the solvent, colloidal particles deposit on the substrate which is immersed vertically in a dilute colloidal suspension [27].

Vertical deposition method leads to sedimentation method for colloidal particles of larger size [31–33]. VD technique is efficient to obtain patterns from very small colloidal systems ( $\ll 500$  nm) that involve very slow evaporating of the solvent and are closer to equilibrium. The process is long and the rate of sedimentation is greater than the rate of evaporation for the colloidal systems of larger particles because of the big densities mismatch with solvent. Hence, vertical deposition technique is mostly suitable for colloidal suspension of polystyrene or silica microspheres. Even silica microspheres are difficult to vertically deposit if their diameter exceeds several hundreds nanometer. To make vertical deposition technique fruitful for deposition of colloidal particles of large size (micrometer scale), it is better to evaporate the solvent faster by increasing the temperature [34, 35]. Shimmin *et al.* [36] and Giuliani *et al.* [35] proposed a region, correlated with the morphology of the structures deposited on the substrate referred as particle pool zone (PPZ). Giuliani *et al.* [35] performed experiments at higher temperatures (63°C) to favour evaporation using dilute suspension of polystyrene particles. Hence, the contact line receded faster due to evaporation of the solvent. They reported the relevance of the speed of the receding contact line to the obtained deposits of colloidal particles through PPZ, which also depends on the initial concentration of the suspension.

In another attempt to control the process in VD technique, Giuliani *et al.* [37] modified it by applying DC electric fields involving evaporation of the solvent. They performed experiments in external weak DC electric fields using water based dilute colloidal dispersion of negatively charged polystyrene particles. They measured the speed of the receding contact line when the external field is applied, to characterize its effect on the deposition process and to evaluate its potential

to control it.

Similarly, here we further modify VD method by applying weak AC electric fields allowing the fluid phase of the suspension to evaporate, focusing on the interface instead of on the bulk dispersion at different temperatures [1]. We perform the experiments at low evaporation (room temperature and humidity) and at higher evaporation ( $63^{\circ}\text{C}$ ). We focus on the contact line region of colloid to explore the behavior of various pattern formation as a function of applied weak AC fields and initial particle concentrations. The obtained results are discussed in detail in chapter 4 and in reference [1].

In the experiments performed with VD technique, the structure formation is almost due to the interaction between flows in the fluid phase and the particles in suspension. The main forces that control the dynamics of this process are: capillary, viscous, inertial and convective momentum transport. The relative importance of these forces can be evaluated from various dimensionless numbers: Reynolds number, capillary number, Péclet number, Rayleigh number, Marangoni number, etc. Some of the relevant dimensionless numbers are defined as follow.

Reynolds number considers the balance between inertial and viscous forces

$$Re \sim \frac{\rho u L}{\eta} \quad (2.1)$$

where  $\eta$  is dynamical viscosity,  $\rho$  is fluid density,  $u$  is the characteristic velocity and  $L$  is the length scale involved in the proposed dynamics. The flow around the particle is supposed to be laminar flow for  $Re \approx 10^{-2}$  or less, where the Stokes law is a very good approximation and the forces acting on a particle are balanced by the viscous forces [38].

Capillary number compares capillary forces with viscous forces where capillary forces are characterized by the surface tension  $\gamma$ :

$$Ca \sim \frac{\eta u}{\gamma} \quad (2.2)$$

It is found that capillary forces overcome viscous forces for  $Ca \approx 10^{-4}$  or less [38].

Péclet number provides the comparison between the advection of particles following the flows and their natural diffusion. In other words, it is the ratio of convective to diffusive mass transport in a fluid i.e.

$$Pe \sim \frac{uL}{D} \quad (2.3)$$

where,  $D$  is the mass diffusion coefficient of the particles in the solution. This coefficient is taken in order of  $k_B T$  where  $k_B$  is the Boltzmann constant and  $T$  is the absolute temperature. Basically, Peclet number determines the efficiency of the flows to drag the particles with respect to their movement due to thermal fluctuations or Brownian motion [38].

### 2.1.1. Evaporation

Cooling because of evaporation at suspension-air interface causes a vertical gradient of temperature and may also result in horizontal gradient of surface tension. These lead to evaporation induced convection [39, 40]. In these thermally driven flows the driving forces are: surface tension gradients (Marangoni forces) and buoyancy forces [41]. A certain critical temperature difference

(temperature gradient) must exist in order to have convective motion. Evaporation induced convection drives the liquid from hot to cold regions decreasing the temperature gradients along the interface and stabilizing the temperature stratification induced by evaporation [40].

Evaporation induced deposition of colloidal particles has been investigated extensively [25, 36]. In this technique the substrate is soaked vertically into the colloidal suspension. The surface of the dispersion is lowered after evaporation of the solvent. The particles in the meniscus region deposit on the substrate. Dimitrov *et al.* [25] used the same procedure to make centimeter-size polycrystalline monolayer films on wettable substrates. The solvent evaporation from the wetting film causes an inward flux. The evaporated fluid is replaced by an inward flow of dispersion from the bulk suspension. The inward flux brings further particles towards meniscus for deposition as a result of temperature gradient at solvent-air interface. This may generate convective long range flows in the regions near the free surface.

## 2.2. Electric Double Layer (EDL)

Particles in solution exhibit surface charge. The analysis and knowledge of which is important, to predict formulation stability and interactions. Helmholtz introduced the concept of electric double layer for the first time [42]. Later on, Gouy and Chapman reported a theory which is also known as electric double layer model [43]. According to this theory, the presence of a net charge on a particle in solution, influences the distribution of ions in the surrounding region which causes an increase in the concentration of counter-ions (opposite to surface charge). The region where this influence evolves is named as electrical double layer [44]. Generally, this layer is supposed to exist in two separate regions as shown in Fig 2.1-A: Stern layer of counter-ions ((a region of charges opposite to the surface charge)) and diffuse layer of free ions of the dispersed solvent near the particle surface. In solution the particle along with ions moves due to flows or Brownian motion or external forces. From the particle surface at some distance within diffuse layer there is a limit beyond which ions do not drag with the particle. This is called slipping plane. This boundary (slipping plane) holds a potential known as the zeta potential ( $\zeta$ ). The knowledge of zeta potential helps to determine the stability of a colloidal suspension. For large negative or large positive zeta potential values, the particles will repel or attract each other, and so the suspension will be more stable. The tendency for fluctuation will exist for low zeta potential values.

The behavior of electrical potential within the electric double layer from the surface of particle is shown in Fig 2.1-B, where it has maximum value on the particle surface (Stern layer). This potential decreases exponentially across the diffuse layer with a characteristic distance given by the Debye length,  $\kappa^{-1}$ . The Debye length  $\kappa^{-1}$  determines the thickness of the ions region around the particle that screens the charge [43]. Further details for the electrical double layer concept are explained in References [43, 44]

## 2.3. Electrokinetics

Electrohydrodynamics (EHD) is the branch of fluid mechanics which is concerned with electrical force effects [45]. It involves both the influence of fluid motion on the fields and the effect of fields on the fluid motion. It is also known as electrokinetics, which is the study of the dynam-

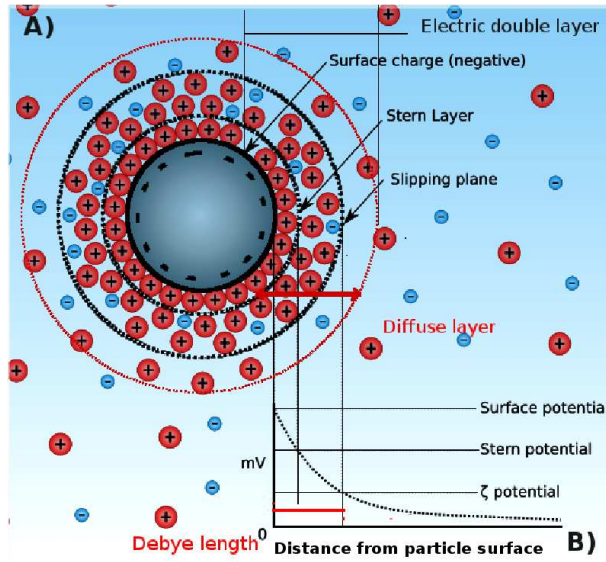


Figure 2.1: Schematic representation of electrical double layer. A) The distribution of ions (counter-ions and co-ions) around a negatively charged particle in solution. B) The electrostatic potential decreases exponentially with a distance from the charged surface within electric double layer with a characteristic distance given by the Debye length. The image is adapted from Wikimedia Commons by Mjones.

ics of electrically charged fluids under the influence of an applied potential difference or electric fields [46]. This phenomenon arises when there is a local displacement of ions in the electrical double layer (see section 2.2) due to some perturbation. That causes the charged surface to move in one direction and the ions of electrical double layer undergo a net migration in the opposite direction resulting in the movement of the solvent [43, 47]. In our VD experiments, we apply weak AC electric fields on the diluted suspension of negatively charged particles placed between the two parallel electrodes, in order to study the influence of electric fields on the dynamics of the colloidal pattern formations at various evaporation. Correspondingly, among the many types of electrokinetic phenomenon, we will focus on those emerging from the interaction with external weak AC-fields and have an affect on our system that include: electrophoresis and electroosmosis.

### 2.3.1. Electrophoresis

Several important properties of colloidal suspensions are directly or indirectly characterized by the surface charge of the colloidal particles [48]. The surface charge and the corresponding electrostatic potential generally yield a repulsive interaction between the particles that stabilizes the suspension. The charged surface of a colloidal particle accelerates relative to the stationary fluid in a constant and homogeneous electric field until the friction force (proportional to the velocity) becomes equal to the electrostatic force. This movement of charged surface in electric field is known as electrophoresis while the electrophoretic mobility  $\mu$  is the ratio between its stationary velocity  $u_c$  and the applied electric field  $E$ .

$$\mu = \frac{u}{E} \quad (2.4)$$

In classical theories, the influence of electric double layer is assumed that screens a part of the surface charge. In 1903 Smoluchowski [49] has reported the most famous and widely used theory of electrophoresis. His theory is based on the set of approximation related to electrophoretic mobility  $\mu$  in terms of Zeta potential ( $\zeta$ ). Using Smoluchowski approximation Zeta potential ( $\zeta$ ) is defined as [49],

$$\zeta = \frac{\eta\mu}{\epsilon_0\epsilon_m} \quad (2.5)$$

where,  $\eta$  is the viscosity,  $\epsilon_0$  and  $\epsilon_m$  the permittivity of vacuum and the relative permittivity of the medium. Introducing eq. 2.5 in eq. 2.4 we obtained the expression for electrophoretic velocity of the particle whose the direction is the same as that of applied fields i.e.

$$u = \frac{E\epsilon_0\epsilon_m\zeta}{\eta} \quad (2.6)$$

The estimated value of electrophoretic velocity for our VD experiments performed at room temperature with weak AC fields as if they were DC fields is calculated i.e. 10  $\mu\text{m/s}$  ( see section 4.1.1 for the estimated values used for the measurements).

### 2.3.2. Electroosmosis

The diffuse layer (Fig 2.1) in an electric field experiences an electrostatic force which displaces the cloud of ions corresponding to the charged surface that move the fluid along with it. This movement yields a flow around the particle which is named as electroosmosis. It depends on the direction of the applied field and the sign of the charges which can induce attraction or repulsion between the particles near a charged surface [50]. Hence, the electric field which is parallel to the charged surface can induce electroosmotic mobility.

The electroosmotic mobility  $\mu_z$  of the ions of the diffuse layer moving with velocity  $u_z$  in the external electric field  $E_z$  in  $z$  direction is given by [51]

$$\mu_z = \frac{u_z}{E_z} \quad (2.7)$$

Electroosmotic mobility  $\mu$  in terms of Zeta potential ( $\zeta$ ) is

$$\mu = -\frac{\epsilon_0\epsilon_m\zeta}{\eta} \quad (2.8)$$

where  $\zeta$ ,  $\eta$ ,  $\epsilon_0$  and  $\epsilon_m$  are the same as discussed before.

### AC electroosmosis (ACEO)

Ramos *et al.* [52] were the first who discovered steady electroosmotic flow using a pair of micro-electrodes in an AC field and named as AC electroosmosis. Later, Green *et al.* [53] investigated the electroosmotic flow employing various kinds of electrode that were designed with sub-micron size fluorescently labelled latex spheres. They applied AC field of 1 Vpp (peak-peak voltage) and 100 kHz frequency to induce charges on the surface of each electrode. They observed that on perfectly polarizable electrodes, the velocity of ACEO flow depends on the applied field frequency, that is zero at high and low frequencies, and have maximum values at the frequency in order of kHz [14]. In our VD experiments, We apply weak AC electric fields in order of magnitude of 1 V/mm and 1 Hz. Therefore, we avoid the effects due to electroosmosis as we apply low frequency electric fields.

## 2.4. Electrowetting theory

The concept of electrowetting phenomenon is introduced before (see section 1.2). Here, we will explain it in more detail. It provides the information about the variation in the contact angle of a liquid droplet on homogeneous substrates by applying external fields. We follow Verheijen and Prins [16] electrowetting model which depends on the principle of virtual displacement of charge, considering the system in the equilibrium at constant electric potential. On applying a voltage  $dU$  an electric double layer (see section 2.2) generates at the solid-liquid interface with a charge density  $\sigma_L$  in the liquid phase and a cloud of oppositely charged counter-ions of density  $\sigma_M$  on the electrode surface. The droplet spreads an area  $dA$  changing its free energy by  $dF$  due to additional charge density  $d\sigma_L$  and  $d\sigma_M$  in the liquid and electrode surfaces respectively (see Fig. 2.3). The applied voltage  $dU$  performs the work  $dW_B$  and the resulted change in the free energy  $dF$  of the droplet is defined as

$$dF = \gamma_{SL} dA - \gamma_{SV} dA + \gamma_{LV} dA \cos \theta + dU - dW_B \quad (2.9)$$

where,  $\gamma_{SL}$ ,  $\gamma_{SV}$ , and  $\gamma_{LV}$  are the surface energies of solid-liquid, solid-vapor, and liquid-vapor interfaces respectively, at zero voltage. In the absence of electric field  $dU = dW_B = 0 \Rightarrow \frac{dF}{dA} = 0$  and eq. 2.9 leads to Young's equilibrium contact angle  $\theta_Y$  given in eq. 2.10 and is obtained by

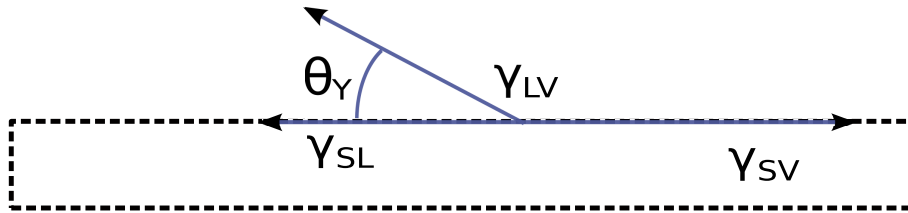


Figure 2.2: Surface forces per unit length on the three phase contact line balancing each other at zero voltage with  $\theta_Y = 30^0$  [19]

balancing the horizontal component of the surface forces acting on the contact line (see Fig. 2.2).

$$\cos \theta_Y = \frac{\gamma_{SV} - \gamma_{SL}}{\gamma_{LV}} \quad (2.10)$$

On applying a voltage the electrostatic energy per unit area that supply extra charges due to charge distribution is

$$\frac{U}{A} = \int_0^d \frac{1}{2} \vec{E} \cdot \vec{D} dz = \frac{1}{2} d E D \quad (2.11)$$

where,  $d$  is the width of the insulating layer,  $\vec{E}$  the electric field,  $\vec{D} = \sigma_L$  the charge displacement and  $z$  the direction perpendicular to the electrode. The change in the electrostatic energy per unit area is

$$\frac{dU}{dA} = \frac{1}{2} d \frac{V}{d} \sigma_L \quad (2.12)$$

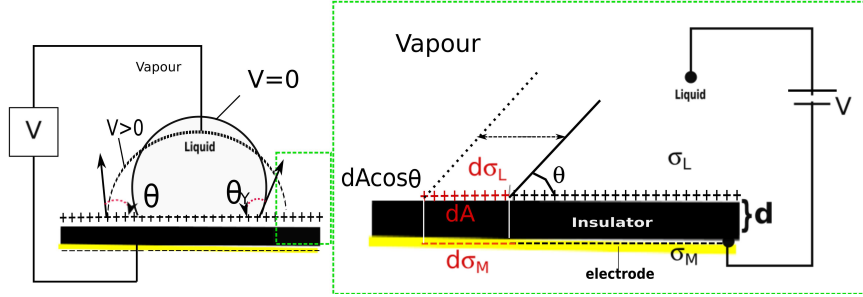


Figure 2.3: Sketch of electrowetting experimental set up (Sessile drop for electrowetting) showing the virtual displacement of the contact line across the dielectric on applying a voltage  $V$ . The free energy of the droplet changes due to infinitesimal increase in its area by  $dA$  and the placement of extra charge densities  $d\sigma_L$  and  $d\sigma_M$ . The sketch is adapted from [16] and further explained in the text.

$$\frac{dU}{dA} = \frac{1}{2}V\sigma_L \quad (2.13)$$

and the work done for the redistribution of charge is

$$\frac{dW_B}{dA} = V\sigma_L \quad (2.14)$$

Performing the minimization of the free energy  $F$  ( $\frac{dF}{dA} = 0$ ) and substituting eqs. 2.14 and 2.13 in eq. 2.9, we obtain electrowetting term in the Young's equation

$$\begin{aligned} \frac{dF}{dA} &= \gamma_{SL} - \gamma_{SV} + \gamma_{LV} \cos \theta + \frac{1}{2}V\sigma_L - V\sigma_L = 0 \\ \gamma_{LV} \cos \theta &= \gamma_{SL} - \gamma_{SV} + \frac{1}{2}V\sigma_L \\ &= \gamma_{SL} - \gamma_{SV} + \frac{\epsilon_0 \epsilon_r}{2d} V^2 \end{aligned} \quad (2.15)$$

introducing eq. 2.10 we get

$$\cos \theta - \cos \theta_Y = \frac{\epsilon_0 \epsilon_r}{2d\gamma_{LV}} V^2 \quad (2.16)$$

where, from Gauss's law  $\sigma_L = \epsilon_0 \epsilon_r \frac{V}{d}$ ,  $\epsilon_0$  is the permittivity of vacuum and the  $\epsilon_r$  is the relative permittivity of the insulating layer. Eq. 2.16 gives the resulted change in the contact angle on applying a voltage  $V$ .

#### 2.4.1. AC electrowetting

The electrowetting theory discussed above is based on the static assumptions, such that the liquid is considered as a perfect conductor and the contact angle and the shape of droplet remain

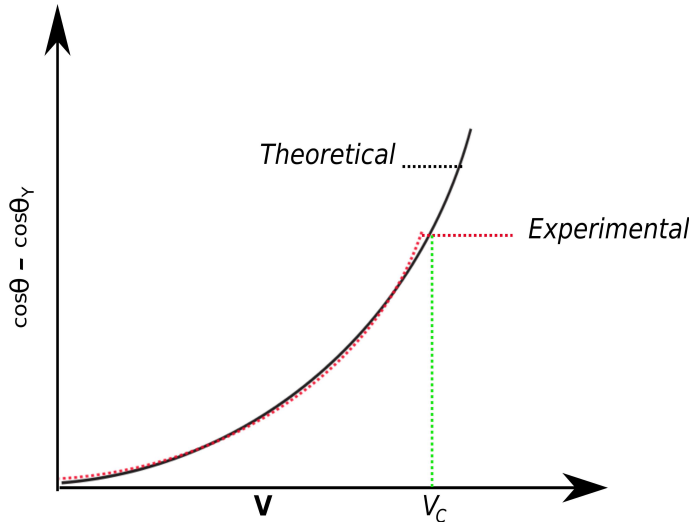


Figure 2.4: Sketch of electrowetting curve indicating theoretical and experimental results for the change in contact angle on applying a voltage( $V$ ) and  $V_C$  is critical voltage where the contact angle becomes constant [54].

in equilibrium at slow changes in the applied voltage. Eq. 2.16 is valid as far as the applied DC voltage does not exceed a certain critical value  $V_C$  (Fig. 2.4), above which the contact angle remains saturated [54, 55]. The electrowetting can also be observed on applying AC field. Where, at low-frequency AC field, the oscillation of a droplet is observed and the hydrodynamic response of the droplet depend on the periodic change of the electric force at the contact line [56]. Certain critical frequency  $\nu_c$  has been considered, below which the droplet behaves as a perfect conductor and above it as a dielectric. Also, a transition from low frequency electrowetting to the high frequency dielectrophoretic behavior is observed, for a homogeneous bulk liquid it is defined as [19]

$$\nu_c = \frac{\varsigma_L}{\epsilon_L \epsilon_0} \quad (2.17)$$

where,  $\varsigma_L$  and  $\epsilon_L$  are the liquid electric conductivity and dielectric permittivity respectively. The electrowetting critical frequency also depends on geometric and electric properties of the insulating layer. All experiments of vertical deposition-like configuration in this thesis have been performed at weak AC field that causes very small effect on the contact angle and behaving as a low DC electric field to keep the system near to equilibrium. Using weak AC field we have measured the estimated value of maximum change in the contact angle which is very small ( $0.0008^\circ$  if we consider  $\theta_Y = 45^\circ$ ), the average contact angle changes with respect to the applied field frequency. For further explanations see section 4.1.1.

# Chapter 3

## Experimental Setup

We perform experiments at room temperatures as well as at higher temperatures in weak AC fields with Vertical Deposition-like Configuration (VD) (see section 2.1). VD experimental set up permits the application of external electric field to colloid and approach to the contact line, where the colloidal transition takes place. This chapter explains the experimental details to obtain colloidal patterns at different temperatures on the application of weak AC electric field.

### 3.1. Materials

#### Suspension

We use colloidal dispersion of spherical polystyrene particles of diameter  $1.3 \mu\text{m}$  (polydispersity: 0.039). These particles are suspended in ultra pure water and their surface charge is  $-7 \mu\text{C}/\text{cm}^2$ . The dispersion (7.43% (w/w)) is provided by Dr. Paulke at Fraunhofer-IAP, Germany. We dilute this dispersion with ultra pure water to lower concentrations and placed in ultra sonic for one hour to re-disperse suspension. We store the diluted suspension in the refrigerator ( $5^\circ\text{C}$ ) to reduce sedimentation. Before each experiment, we sonicate this suspension for fifteen minutes to prevent agglomeration [38].

#### Substrates

Standard glass substrates ( $1.1 \times 17 \times 18 \text{ mm}^3$ ) with one side coated with a thin conductive layer ( $\sim 150 \text{ nm}$ ) of Indium Tin Oxide (ITO) are used for all experiments. These substrates are obtained from VisionTek Systems Ltd. United Kingdom.

### 3.2. Experimental system

Teflon<sup>®</sup> cell and its function is shown in Fig.3.1. The substrates, with its conductive side in contact with the suspension, are set vertically and resemble a parallel plate capacitor (Fig.3.1a). The conductive side of ceramic spacers coated with silver foil mask tape is kept in contact with ITO coated side of the substrates for the application of electric field. Rubber O-rings are used to avoid leaking of the suspension. Weak AC electric field of square wave form is applied perpendicular to the conducting substrates (Fig.3.1b). The two substrates are placed at 1 mm distance from each

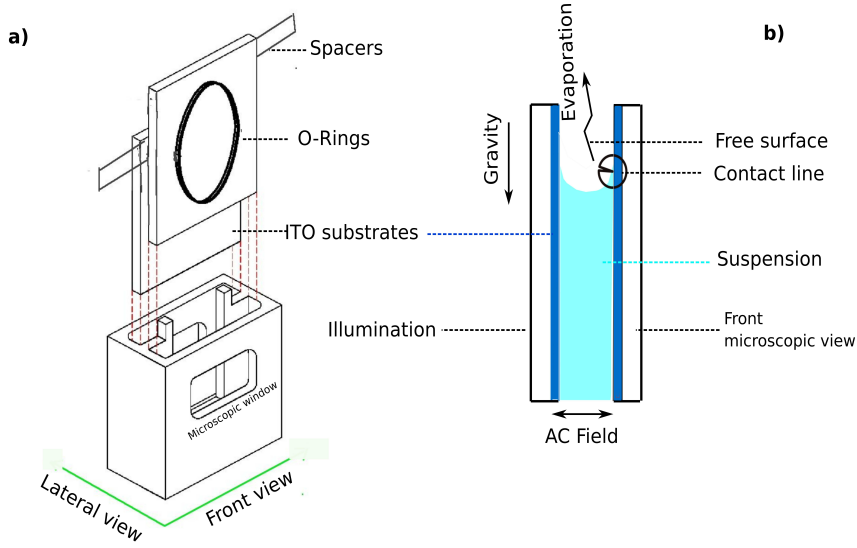


Figure 3.1: a) Sketch of the experimental cell before mounting the substrates and other components. It is illuminated from the back side and the microscope is provided from the front side through microscopic windows. b) Schematic diagram of a part of lateral view of the cell directing towards its basic function. The distance between both substrates is 1 mm. The sketch is reprinted from [1]

other. Only a small volume of the suspension is inserted which fills the cell up to the area of the observation. The reduced size permits the access of homogeneous weak AC field to the suspension and keeps the evaporation almost constant during the experiments at room temperature. Initially, the contact line is observed in convex shape with a maximum in the middle of the cell that gradually reaches to a flat profile when the mechanical equilibrium is achieved [37, 38]. The images of a relatively flat contact line are saved sequentially. Black circle in Fig.3.1b shows the contact line which divides the field of view in two regions; the upper region with maximum intensity (free surface) that decreases towards the bottom (bulk suspension), an example of it can be seen in Fig.3.2. The optical microscope arrangement (INFINITUBE) is focused on the contact line (far from the lateral boundaries of the cell on the substrate near to the microscope) instead of on the bulk suspension and is illuminated through an optical fiber illuminator. The INFINITUBE is connected with a color Complementary Metal Oxide Semiconductor (CMOS) camera (PixeLINK, PL-B776F, 3 Megapixel) for capturing frames.

### 3.3. Cleaning procedure

#### Surface wettability and cleaning of the substrates

The ITO coated substrates of hydrophobic character (confirmed with Sessile Drop Technique) as provided, its wettability varies with different cleaning procedures. We performed the experiments using different cleaning methods. The substrates become more hydrophilic when they are cleaned with acetone and piranha solution. Firstly, the substrates are kept in acetone for fifteen minutes to remove the organic materials. Secondly, they are transferred to piranha solution in

ultrasonic bath at 63 °C for forty minutes, where a basic piranha solution which is composed of H<sub>2</sub>O : NH<sub>4</sub>OH : H<sub>2</sub>O<sub>2</sub> in a proportion of 5:3:1 respectively is used. Lastly, they are rinsed with ultra pure water and dried with filtered air blow. The freshly cleaned substrates are later mounted in the experimental cell. The piranha cleaning procedure that activates the ITO surface does not lead to an equilibrium state of the surface and it evolves to reach the hydrophobic state to achieve equilibrium [35]. The application of external AC electric field through electrowetting effect (see section 4.1.1) changes the contact angle of the surface [1]. Therefore, to ease the reproducible character of the contact angle during the vertical deposition experiments, we rinse the substrates with ultra pure water and dried it with filtered air blow before mounting them in the cell. The hydrophobic character of the ITO coated substrates is convenient to obtain a relatively small variation in contact angle on the application of weak AC electric field.

### Cleaning of the experimental cell

The inert Teflon® cell, before mounting the substrates and other components, is cleaned with diluted soap solution (Micro-90®, concentrate cleaning solution, used for critical cleaning applications). Then, it is intensively rinsed with ultra pure water and dried with filtered air blow.

## 3.4. Experiments at room temperature

The experiments here are performed using the experimental set up shown in Fig.3.1 at room temperature and humidity, where colloidal dispersion evaporates slowly. The freshly cleaned and dried ITO substrates are mounted into the experiment cell. Electrical contacts from arbitrary

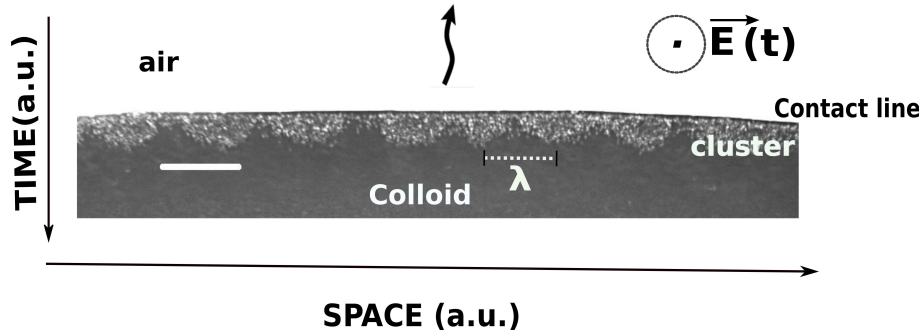


Figure 3.2: Front view of the contact line where bright spots are clusters, at 2 Vpp and 1.4 Hz, 0.9 % (w/w) concentration. The scale bar is 50  $\mu$ m. Frame is captured during the experiment performed at room temperature (wavy arrow shows low evaporation) at the time scale when clusters stabilize their size. This image is adapted from [1].

wave generator (Tektronix AFG3022B) are connected with ceramic spacers for the application of AC electric field. AC field of square wave form of low frequencies and voltages is applied perpendicular to the substrates. 100  $\mu$ l of diluted colloidal suspension is poured into the cell. INFINITUBE with an objective of 10X magnification is focused on the contact line (far from the boundaries on the substrate closer to the microscope). The central part of the cell is illuminated through a DC regulated illuminator (200 W, MOTIC MLC-150C) from the opposite side of the

cell, to observe the pattern formation. The images of a relatively flat contact line are saved sequentially with acquisition rate of about 33 frames per second at a resolution of  $2048 \times 256$  px with a CMOS camera. Fig.3.2 presents a front view sample of one of the frames saved during the experiment at room temperature with AC field, when the clusters are built up. The one-dimensional array of clusters (the field of view) can be seen near the contact line, which separates air and colloid on the nearest substrate to the microscope. The results are explained in chapter 4. We perform the experiments at different low frequencies, field strengths and initial particle concentrations by keeping one of the variables constant.

### 3.4.1. Characterization

#### The characteristic length

The mechanism of clusters evolution is characterized as a function of increasing initial particles concentration at different applied field frequencies, in terms of characteristic length between the clusters  $\bar{\lambda}$ . The results are discussed in the next chapter (see section 4.1.2). To measure this characteristic length  $\bar{\lambda}$ , frames of the front view samples are captured in-situ at a time scale, when the clusters stabilize their size, using a microscope objective of 10X magnification (see Fig.3.2). Here, the emerging groups of particles are spatially distributed and separated by a distance  $\lambda$ . The characteristic length  $\bar{\lambda}$  defines the average distance between the clusters.  $\bar{\lambda}$  is measured in pixels from captured frame. Next, it is scaled to standard units in micrometers. The error bars that show the standard mean deviation are calculated by free software package GNU Octave [57].

#### Unit conversion

We convert the values of  $\bar{\lambda}$  in pixels (px) to  $\mu\text{m}$ . The images of all cluster evolution experiments are taken with the same optical arrangement (using 10X magnification microscope) that gives the size of the images in pixels. Therefore, the unit conversion difference value (from px to  $\mu\text{m}$ ) for 10X and 2X microscopic magnifications are obtained by using diffraction grating of known number of lines and the distance between two lines in standard unit, which is multiplied with calculated values of  $\bar{\lambda}$  in pixel (using gimp) to convert into standard unit of length. The unit conversion difference value changes by changing the objectives even in the same optical arrangement.

### 3.4.2. Electrokinetic characterization

To characterize the electrokinetic effect, patterned Indium Tin Oxide (ITO) substrates are mounted in the experimental cell of Fig.3.1.

#### Substrates patterning procedure

A thin layer of S-1813<sup>TM</sup>G2 positive photoresist is spin-coated onto the provided ITO coated substrates at 4000 rpm for one minute using commercial spin-coater. Then, it is soft baked at 100 °C for one minute. The substrate with photoresist film is covered with a mask of the desired pattern. It is exposed to an ultraviolet (UV) light for three minutes. The unmask area due to the UV exposure becomes acidic. 0.5% (w/w) NaOH solution is used as a developer where the

exposed substrate is immersed in it for thirty seconds. After, it is rinsed with ultra pure water and dried with filtered air. Later on, it is etched chemically by placing in HCl (11.65 M) for five

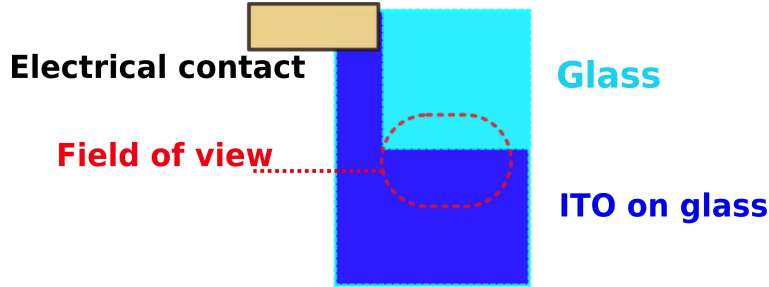


Figure 3.3: Top view of the patterned Indium Tin Oxide (ITO) substrate, which has two parts, the dark blue region is ITO on the glass and the light blue is glass. The window (red dotted box) is the field of observation.

minutes and then rinsed with ultra pure water where the unmask region becomes ITO free. The mask is removed and the etched substrate is cleaned with acetone to remove the rest unexposed photoresist. Later, it is rinsed with ultra pure water and dried with filtered air blow. Fig.3.3 indicates the patterned ITO substrate, where dark blue area is ITO and light blue part is glass.

## Experiments

The freshly patterned substrates are mounted into the cell for doing experiments at room temperature following the same experimental procedure discussed in section 3.4.

### 3.4.3. Evaporation characterization

To characterize the influence of evaporation on the clusters evolution, the upper part of the experimental cell of Fig.3.1 is closed and the experiments are performed at room temperature following the same experimental procedure explained in section 3.4. Clusters are not obtained in this experiment. Thus, evaporation is required for clusters evolution.

### 3.4.4. Particle Image Velocimetry

The PIV (Particle Image Velocimetry) technique assists to measure quantitatively the fluid velocity field at given time [58, 59]. PIV records the position over time of small tracer particles introduced into the flow to extract the local fluid velocity [60]. The PIV system operation typically consists of two steps: one is the acquisition of the images for PIV recordings and the second step consists of the numerical tools for correlating the data in terms of post-processing. Fig.3.4 presents basic scheme of the two steps, (a) displays the original image used for the PIV and (b) is the post-processed fields, where the velocity of the particles can be obtained by computing the cross correlation between both images that provides the displacement of the particles.

#### Image acquisition

The acquisition of the images for PIV analysis in our case is done by following a simple procedure. As the velocity of our system is very low (in few  $\mu\text{m/s}$ ) therefore the production of clear

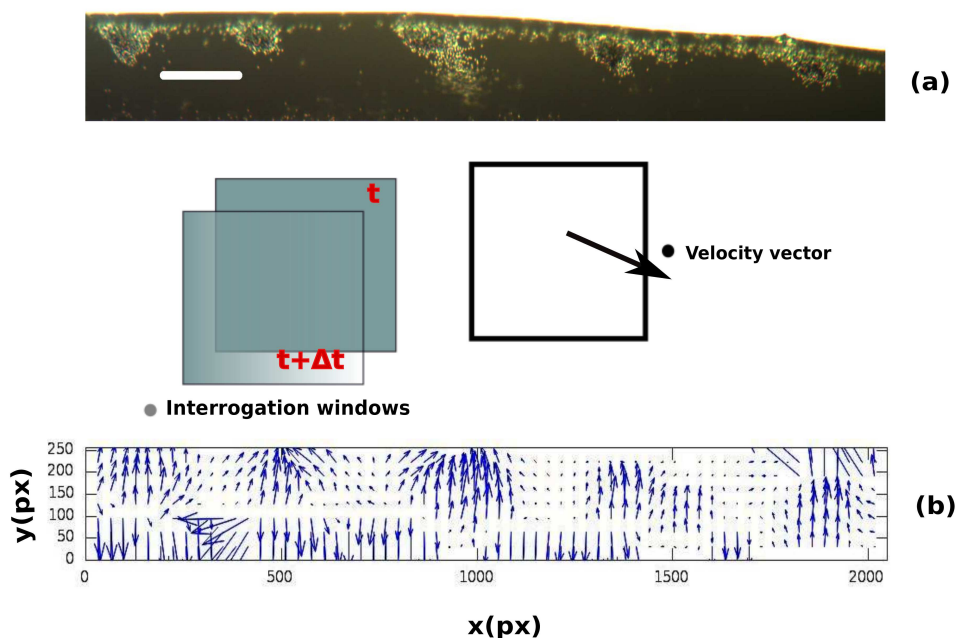


Figure 3.4: Scheme of a PIV analysis in our case. (a) The original image saved at time  $t$ , the scale bar is  $64 \mu\text{m}$ . In the middle we present a pair of interrogation areas before being correlated and their correlated velocity field vector. (b) The mean field velocity obtained via two successive images.

images of the seeded particles position are possible with normal light source. Seeded particles (polystyrene particles of diameter  $1.3 \mu\text{m}$ ) of suspension are illuminated with high intensity illuminator (200 W, MOTIC MLC-150C). Fig.3.5 indicates the schematic diagram of the PIV acquisition of images experimental setup. The frames are saved sequentially with desired acquisition rate with a small increment of time between two successive frames, at a resolution of  $2048 \times 256$  px with CMOS camera. The images that are captured in such a way, if the first frame of the flow is obtained at time  $t$ , after a small increment of time  $\Delta t$  we capture another picture at  $t + \Delta t$  (Fig.3.4) [59].

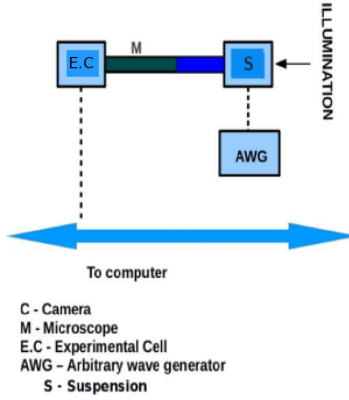


Figure 3.5: Sketch of the experimental setup for the PIV acquisition of images.

### Post-processing

The velocity field of the particles for the two successive PIV images which are captured at time  $t$  and  $t + \Delta t$  is obtained by cross-correlation methods. That analyze two single exposures [59]. We assume the interrogation windows of the first and second images shown in the middle of Fig.3.4. In Fig.3.6, the point  $p(x,y)$  in the interrogation window of first image corresponds to point  $q(x,y)$  in the interrogation window of the second image which is determined by the maximum cross correlation coefficient [61]. The velocity at point  $p(x,y)$  is calculated from the displacement of  $p(x,y)$  and  $q(x,y)$  given in Fig.3.6b. In case of using cross correlation method for post-processing, the size of interrogation window (SA) around the point  $p(x,y)$  in the first image and the size of the search window (SB) for searching the point  $q(x,y)$  in the second image, are two important parameters for the PIV analysis. The size of the interrogation window is kept bigger enough for having sufficient number of particles to get PIV results with high accuracy. After the correlation algorithm (Fast Fourier Transform (FFT)) is applied to each one of these image elements, to get a velocity vector per interrogation window (Fig.3.4). However, the output vector fields and the magnitude of the correlated velocity are very sensitive to the analysis. The field velocity vector maps are computed by using the Dantec Dynamics software FlowManager 4.50.17. For the post-processing analysis, 50% of overlapping for the interrogation windows of  $32 \times 32$  px is adjusted in our case.

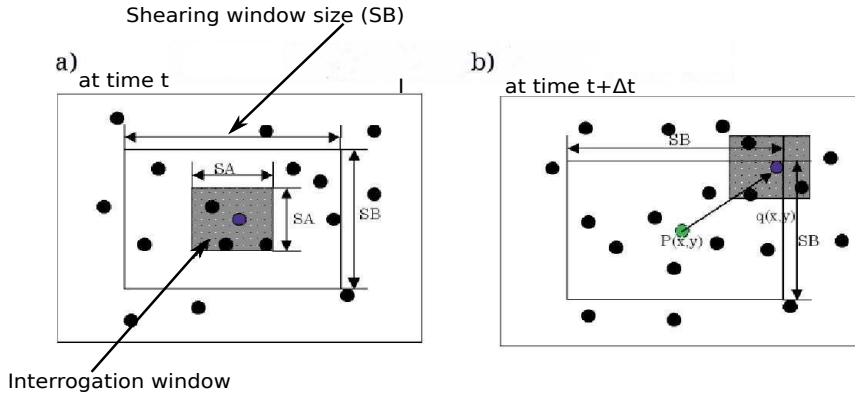


Figure 3.6: Sketch of a pair of PIV frames for the post-processing, adapted from [59].

### The effect of time interval between two successive images

The time interval  $\Delta t$  between two successive images affects the output vector fields and the magnitude of the correlated velocity [61]. If the time interval is very small, the average movement distance of the seeded particles is also small. In this case because of the limited resolution of image, the average error of the PIV result is still big although the PIV correlation result is high enough. Similarly, when the time interval between two overlapping images is very large, the average movement distance of tracer particles is larger. Therefore, the chances of the deformation of the particle position increase, which also causes a poor PIV results. Hence, the selection of the optimum time interval  $\Delta t$  between two successive images is also an important parameter during the PIV measurement to obtain final results with high accuracy.

#### 3.4.5. Short term closed flows and PIV analysis

To demonstrate short term flows which are responsible for the evolution of clusters with PIV, we set optical arrangement shown in Fig.3.5 to obtain 33 frames per second with 30.30 ms time interval between the two frames. Next, certain number of original images that were obtained during the time period of external field, are used for PIV analysis. If we use external field of frequency 1.4 Hz and time period of 0.714 seconds, hence images saved in this time period are uploaded for PIV. Similar PIV results are obtained for the frames captured in the beginning, middle and end of the same experiment. After, vector field is obtained by computing the cross correlation function configuration of the PIV system for the two successive images, that informs us about the displacement of the flow, caused by the applied external field. These results of PIV analysis are explained in detail in the next chapter.

#### 3.4.6. Long term flows and PIV analysis

To characterize long term flows in the experiments of cluster formation with PIV analysis, the contact line is tracked microscopically from the beginning of the experiment till the clusters dissociate. The images of the contact line are saved sequentially after the trigger signal is received (at each red cross in Fig.3.7(up)). We suppose to capture frames (on blue dots in Fig.3.7(down)) at those points of input signal (red cross) that display the maximum velocity of the tracking particle.

We set the trigger delay following short term flow procedure which informs us about the point on

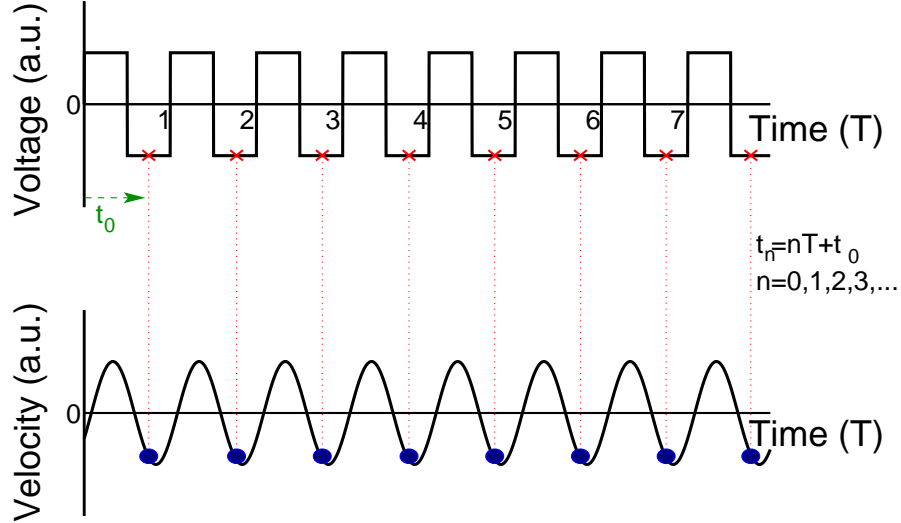


Figure 3.7: Sketch of trigger input signal (up) and the imagined output velocity of the tracking particle in long term flows (down). Where,  $t_0$  is trigger delay and  $T$  is the time period of the applied field.

the input signal where the tracking particle could have maximum velocity. Trigger delay ( $t_0$  = trigger delay in Fig.3.7) adjusts when the camera starts to capture the first image. If the delay is zero, it starts capturing immediately after the trigger is achieved. We set positive trigger delay (post-trigger delay). In case of post-trigger delay, camera begins capturing the desired first frame after the trigger delay time. In other words, the first point (on the input square signal) in the Main Time trace will have a time value equal to the delay. First, we adjust the trigger delay such that the tracking particle has maximum velocity. Next, trigger signal permits capturing sequential images at selected points (red crosses in Fig.3.7) on the input square signal after each time period of the applied signal ( $T$ ), where the flow velocity is considered maximum for the long time scale. In this case the time interval  $\Delta t$  between the two successive frames is determined by the time period of the applied field frequency. If we use external field of frequency 1.4 Hz and time period 0.714 seconds, later the time interval  $\Delta t$  between two successive images for PIV recording is 0.714 second. To control with trigger signal, the TTL (Transistor-Transistor logic) output, synchronized with channel 1 of the arbitrary wave generator (Tektronix- AFG3022B) is connected with control of the CMOS camera. Also, the first frame of the saved images is kept as a reference to measure the initial time and position of contact line from the stored sequential images. After some time, the contact line may recede to a new position. The time for this contact line position is noted. The rate of the receding of the contact line (the average velocity of the contact line) is measured from the calculated change in length and time.

### 3.5. Experiments at higher temperatures

We perform the experiments in a thermal chamber at higher temperatures and at fixed humidity to obtain colloidal dried deposits with and without applying weak AC field. Fig.3.8 displays

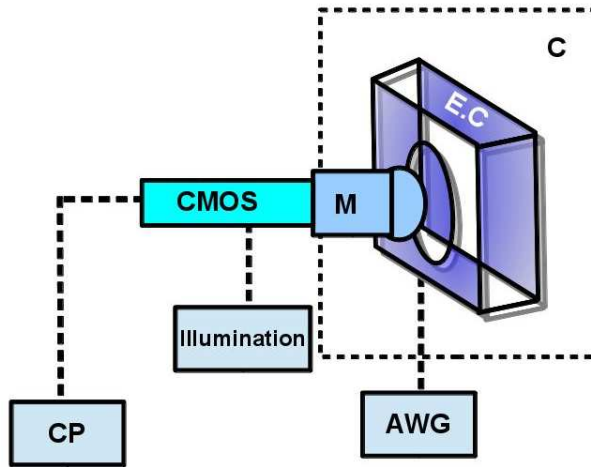


Figure 3.8: Sketch of the experiment setup to track colloidal pattern formation inside thermal humidity controlled chamber. Illumination: cold light source; E.C: experiment cell; CMOS: camera; AWG: (Arbitrary Wave Generator); M: microscope; C: thermal chamber; CP: computer.

the sketch of the experimental details done inside the thermal chamber. The chamber is set at controlled temperature and humidity accordingly. Once the chamber reaches the desired state, the freshly cleaned mounted cell shown in Fig.3.1 is placed inside it. Afterwards, 100  $\mu\text{l}$  of ultrasonicated colloidal dispersion is inserted into the cell. INFINITUBE with a microscope of 10X magnification is focused on the contact line region in the central part of the substrate closer to the microscope. High intensity illuminator (MI-150, 150 W, having a 0-100% intensity control and low noise level (25 dB)) connected with INFINITUBE is illuminated on the front substrate closer to microscope to observe colloidal deposition processes. The images of a contact line are saved sequentially at a resolution of 2048 $\times$ 1536 px with color CMOS camera. For the experiments performed without applying AC field, the temperature is kept at 63 °C and the relative humidity is maintained at 30%RH (see next chapter for results). Experiments are done at various temperatures (40-63 °C) keeping the humidity unchanged (30%RH) in the presence of weak AC electric field. For the application of AC electric field (of square wave form) the electrical contacts from the arbitrary wave generator are connected with ceramic spacers. We manifest in Fig.3.9 a front view sample obtained in the experiment of high evaporation (63 °C, 30%RH) with basic experimental details on the application of AC field of low frequency and field strength. A recently deposited (drying) vertical column of colloidal particles can be seen in the center of the figure (out of focus), where contact line separates the colloid and the air and wavy arrows show high evaporation. We perform the series of experiments at fixed AC field, changing the temperature inside the chamber using different initial particle concentrations. We observe various interesting results that assist us to maintain the temperature and humidity inside the chamber about 63 °C, 30%RH respectively. At this controlled higher temperature and humidity we get well dried colloidal columnar deposits on applying AC fields. Images of the whole dried deposits are captured with monochrome CMOS camera (Pixelink PL-A741, 1.3 Megapixel).

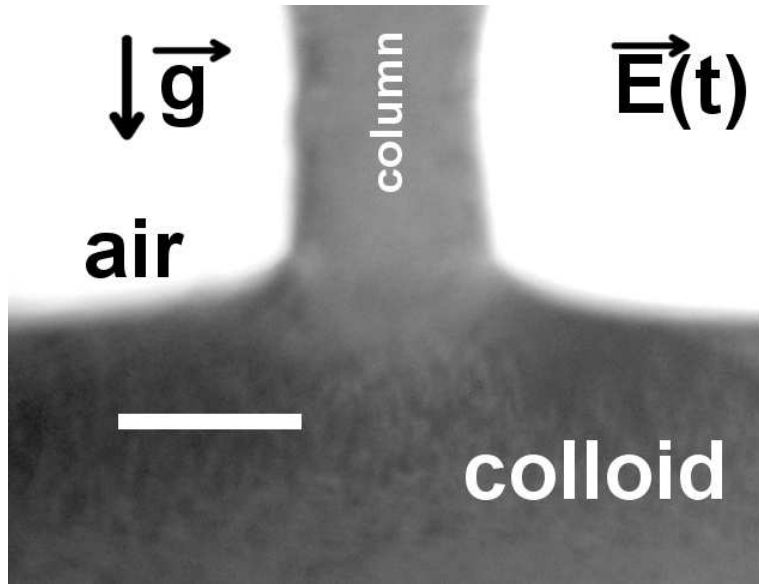


Figure 3.9: Front view sample (out of focus) of the deposition processes on the substrate closer to the microscope with high evaporation (wavy arrows). Electric field is applied perpendicular to the substrate and evaporation is perpendicular to the surface in contact with the air. Field 1 V/mm and 1.8 Hz, 0.5% (w/w) concentration. Recently building column in the center. The scale bar is 50  $\mu\text{m}$ . This image is adapted from [1]

### 3.5.1. Characterization

#### Characteristic width of Columnar deposits

Optical images of the dried deposits of colloidal particles on the ITO coated side of the substrates are captured with a microscope of low magnification (2X), connected with color CMOS camera Fig.3.10. We find that, the thickness of the dried columnar deposits increases on increasing the field strength, for different frequencies at fixed concentration 0.5% (w/w). We measure characteristic width of columnar deposits. To do so, width at different thicknesses (green line in Fig.3.10) of the individual column as well as the others columns of the same experiment are calculated. Later, the average value (characteristic width) is obtained for each experiment at different field strengths.

#### Characteristic length

The behavior of columnar deposits is characterized as a function of increasing initial particles concentration at different applied field frequencies, in terms of characteristic length between the columns  $\bar{\lambda}$ . The results are discussed in the next chapter. To measure the characteristic length  $\bar{\lambda}$ , the image of dried deposits of colloidal particles on the ITO coated side of the substrates is captured with a microscope of low magnification (2X), connected with color CMOS camera Fig.3.10. Then, the distance between columns of the same experiment is measured in GNU Image Manipulation Program, GIMP. The characteristic length  $\bar{\lambda}$  defines the average distance between the columns. The measured  $\bar{\lambda}$  in pixels is then scaled to standard units in micrometers.

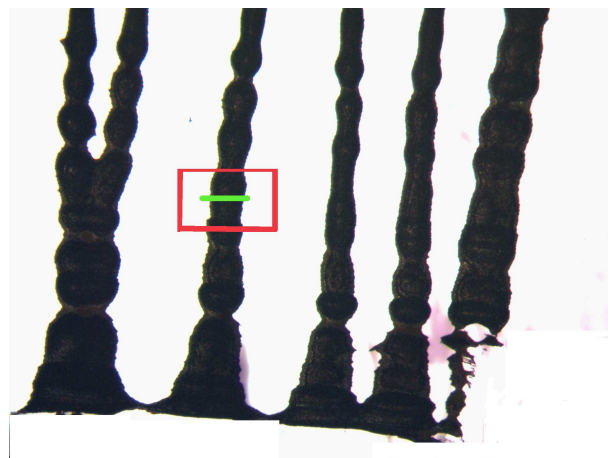


Figure 3.10: Low magnification (2X) bright field image showing front view sample of dried deposits of colloidal particles. Green line shows the thickness of the column. Field during deposition is 2.2 Hz and 1 V/mm. Concentration - 0.5% (w/w) at 63 °C. The scale bar is 230  $\mu\text{m}$  (green line).

# Chapter 4

## Results and Discussions

Here, we present the experimental results on weak AC field-induced colloidal pattern formation in vertical deposition-like configuration (experiments are performed at room temperature and inside a thermal chamber maintained at different higher temperatures). We obtain clusters at low evaporation (room temperature and humidity) and elongated columnar deposits at higher evaporation ( $63^{\circ}\text{C}$ ). We focus on the contact line region of colloid to explore the behavior of these pattern formation as a function of the applied weak AC fields (0.8 V/mm to 1.2 V/mm and 1 Hz to 3 Hz) and initial particle concentrations. The obtained results are discussed in detail for characterizing the involved mechanisms of pattern formation.

### 4.1. Low evaporation and evolution of clusters

M. Pichumani *et al.* [62] have studied colloidal clusters formation by weak AC field. We investigate here the involved mechanisms by characterizing the weak AC field induced-flows of the system by PIV (Particle Image Velocimetry) analysis, showing that colloidal particles follow the external field. We investigate the effect of the increasing initial particle concentration (0.5 % (w/w) to 1.1 % (w/w)) and the applied field on the formation of clusters.

Summarizing the experimental conditions at room temperature, as soon as the dispersion ( $100\ \mu\text{l}$ ) is inserted into the cell, electric field is applied and images are saved sequentially. Fig. 4.1 shows front view samples of different stages that result during the low evaporation experiments at various time intervals. Particles start to move towards the contact line through electrowetting, electrokinetic and capillary forces, where they accumulate (Fig. 4.1A). Then, come closer to each other, they group in the form of clusters and continue to grow till they stabilize their size (Fig. 4.1B). The one-dimensional array of clusters can be seen near the contact line, which separates air and colloid on the nearest substrate to the microscope (Fig. 4.1B and C). These clusters start to dissociate (Fig. 4.1D) after some time [62].

#### Short term closed flows and PIV analysis

To demonstrate the response of the system to the applied field, we study the flow-dynamics involved in the aggregation of particles at the contact line with PIV. In Fig. 4.2, we show the flows near the contact line in the presence of clusters, at 1 V/mm and 1.4 Hz using 0.9 % (w/w) concentration. Subplot (a) shows a bright field image (field of view is 0.67 mm) at a point of

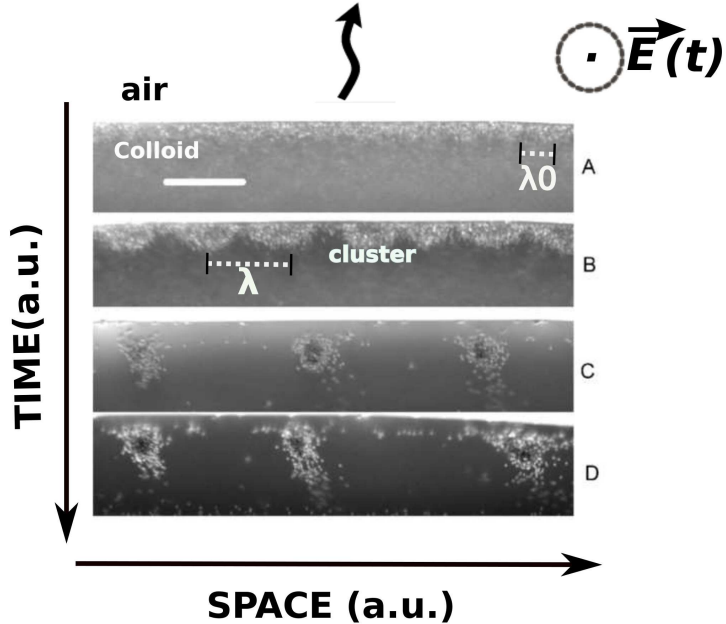


Figure 4.1: Frames A–D are front view samples of the contact line, captured at various time intervals showing different stages during the low evaporation experiment, at 2 Vpp and 1.4 Hz, 0.9 % (w/w) concentration. The bright spots are clusters. The scale bar is 150  $\mu\text{m}$ .

the square wave cycle of the applied field, which we set as time-origin of the cycle, (b) is the PIV (cross correlation average filtered) analysis of (a) at time  $t = 0$ , (c) is at  $t = \frac{T}{2}$ , (d) or (e) is the state at  $t = \frac{T}{4}$  in between (b) and (c). Subplots (b-d) indicate that these flows follow the applied field frequency. Meanwhile, during the change in the flow direction at the stagnation curve (dashed wavy line of Fig. 4.2c), the velocity field is relatively small (Fig. 4.2d or Fig. 4.2e, where (e) is the normalized form of (d)).

#### 4.1.1. Discussion

##### Short term flows

The short term closed flow dynamics characterized by PIV analysis (Fig. 4.2) can be further explained by the microscopic lateral view sketch near the contact line (Fig. 4.3). By applying electric field to the system, the variation in the contact angle generates short range closed flows (perpendicular to the substrate in the meniscus, Fig. 4.3, curved double arrows), that give rise to instabilities in the certain range of the control parameters, like frequency (1 Hz to 3 Hz), field strength (0.8 V/mm to 1.2 V/mm) and initial particle concentration (0.5 % (w/w) to 1.1 % (w/w)). It has been reported in the literature [63, 64], that the electrohydrodynamic instabilities observed in these experiments are due to electrokinetic and electrowetting [17–19, 65] mechanisms.

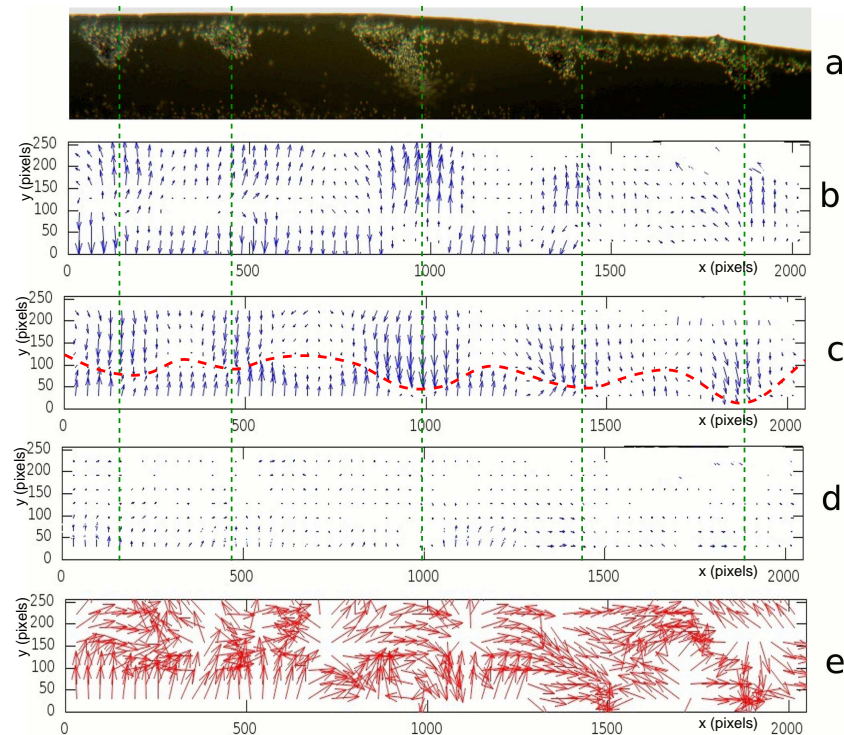


Figure 4.2: Front view of the flow at the end of the experiment, showing different stages in half cycle of the applied field (1 V/mm), following field frequency (1.4 Hz). Dashed wavy line in (c) is a guide to the eye for the stagnation line on the substrate. Vertical dashed lines are guides to the eye which correlate maximum absolute value of vertical velocity (b and c) with the minima of the stagnation line (c) and with the position of the clusters (a). Concentration is 0.9 % (w/w). Subplots (a-e) are explained in the text. Field of view is 0.67 mm = 2048 pixels. This image is reprinted from [1].

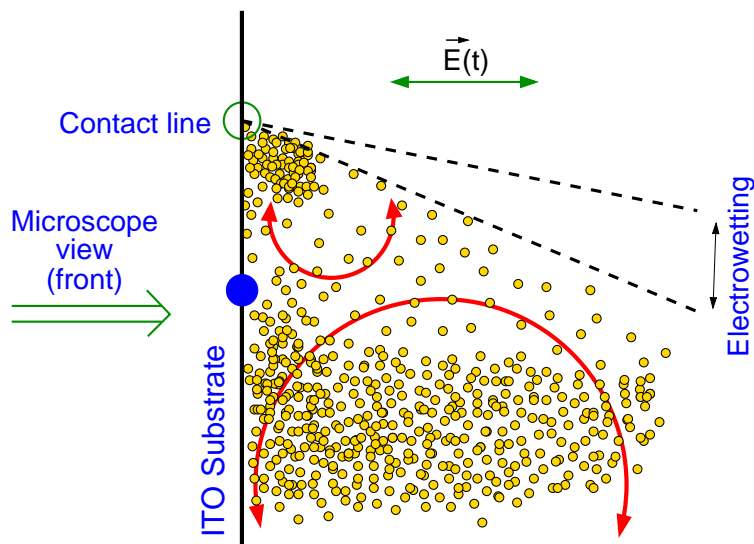


Figure 4.3: Lateral view sketch of short ranged perpendicular flows following the applied field frequency. States b and c of Fig. 4.2 correspond to the cases where top curved (red) double arrow points clockwise and counterclockwise, respectively. Top and bottom curved arrows show local flows induced directly by the electric field and oscillate out-of-phase (clockwise versus counter-clockwise). The remaining state d of Fig. 4.2 corresponds to the time when curved arrows change their direction. The up and down variation in the contact angle (electrowetting effect) is shown by the straight double arrow. The open (green) circle represents a point of the contact line. The filled (blue) circle is a point of the stagnation line shown in Fig. 4.2c. This image is reprinted from [1].

### Electrophoretic effect

The estimated values in order of magnitude of electrophoretic velocity can be obtained by introducing the equation given in [38]

$$\vec{u} = \frac{q\vec{E}}{6r\pi\eta} \quad (4.1)$$

where  $\vec{u}$  is the velocity of the particle,  $q$  is the total effective surface charge of the particle,  $\vec{E}$  is the applied field and  $r$  is the radius of the particle and  $\eta$  is the viscosity. Typical values of these parameters for our system are

$$Q \approx 4.4 \times 10^{-13} \text{ C} \quad (4.2)$$

$$E \approx 1 \text{ V/mm} = 10^3 \text{ V/m}$$

$$r \approx 0.7 \times 10^{-6} \text{ m}$$

$$\eta \approx 1 \text{ cP} = 10^{-3} \text{ N s/m}^2$$

$$(4.3)$$

equation 4.2 presents the surface charge of the sphere ( $Q = -7 \times 10^{-2} \text{ C/m}^2 \times S \text{ m}^2$ , where  $S$  is the area of the sphere of radius  $R$  which is  $4\pi R^2$ ) and the effective charge of the particle is the sum of the surface charge  $Q$  and that in the Stern layer. To consider the effect of Stern double layer that screens a part of the surface charge, we suppose Smoluchowski approximation related to electrophoretic mobility  $\mu$  in terms of Zeta potential ( $\zeta$ ) and is valid for  $\kappa_r \gg 1$  and  $\kappa_r^{-1}$  is the Debye length [49].

$$\begin{aligned} \mu &\equiv \frac{u}{E} = \frac{q}{6r\pi\eta} \\ \zeta &= \frac{q}{4\pi\epsilon_0\epsilon_m r(1 + \kappa r)} \\ \zeta &= \frac{\eta\mu}{\epsilon_0\epsilon_m} \end{aligned} \quad (4.4)$$

$$u = \frac{E\epsilon_0\epsilon_m\zeta}{\eta} \approx 10^{-5} \text{ m/s} \approx 10 \text{ } \mu\text{m/s} \quad (4.5)$$

$$(4.6)$$

where, equation 4.4 is obtained from Smoluchowski approximation [49].

The direction of electrophoretic velocity of the particles is the same as that of the applied fields. The estimated value of electrophoretic velocity given in equation 4.5 is  $10 \text{ } \mu\text{m/s}$ . Here, external field is suppose to be constant which can induce a redistribution of the charges in the suspension (particles and possible electrolytes in solution) until a new equilibrium is achieved. Electrophoretic velocity of particles changes the direction if AC field is applied. The particle oscillates about its mean position with smaller velocity. In our case, if we use AC field of square wave form of  $1 \text{ V/mm}$  strength and  $1.4 \text{ Hz}$  (time period  $0.7 \text{ s}$ ) frequency, the particles are not able to travel more than  $3.5 \text{ } \mu\text{m}$  at the velocity given in equation 4.5. Therefore, we suppose that the electrophoretic effect plays a relevant role only for transporting those particles which are closer to the meniscus and affected by capillary forces.

### Electrowetting effect

The homogeneous variation of the contact angle due to electrowetting effect on applying AC field, becomes unstable and breaks the translational symmetry at the meniscus and generates short range closed flows. We obtain the estimated values for electrowetting effect following the same procedure for our experimental conditions explained in [38]. The variation in contact angle by electrowetting effect is obtained from the equilibrium condition of a parallel plate capacitor [65] (see section 2.4) i.e.

$$\cos \theta(V) = \cos \theta_Y + \frac{\epsilon}{2d\gamma_{LV}} V^2 \quad (4.7)$$

where,  $\theta$  and  $\theta_Y$  are the equilibrium contact angles with and without field, respectively,  $d$  is the width of the insulating layer,  $\gamma_{LV}$  is the surface tension between suspension and air and supposed to have the values in between surface tension of polystyrene and water [38, 72]  $10^{-3} \text{ N/m}$  at  $25^\circ \text{C}$  obtained from [66],  $\epsilon = \epsilon_0 \epsilon_r$  is the electric permittivity of the dielectric layers and  $V$  is the voltage difference between electrodes. Here, the two electrodes are the ITO coated glass substrates having resistivity of  $12 \Omega/\text{sq}$  which enclose the diluted colloid. The system near the electrodes works like a parallel-plate electrolysis cell where on applying a voltage above  $\approx 0.9 \text{ V/mm}$ , due to electrochemical processes, the water molecule hydrolyzed and electrodes become coated with a very thin insulating layers of  $\text{H}_2$  and  $\text{O}_2$  [67]. The electrodes reactions are stopped once these barriers are formed [67]. The reaction  $2\text{H}_2\text{O(l)} = 2\text{H}_2\text{(g)} + \text{O}_2\text{(g)}$  will continue till the needed voltage is provided. In our experimental conditions, the  $\text{H}_2$  and  $\text{O}_2$  bubbles could not escape from the electrodes because the ITO behaves as hydrophobic surface and also the applied voltage does not exceed the threshold value [67]. To study the electrowetting effect using equation 4.7, we consider the highly heterogeneous real system as an idealized one. In this approximation, the dielectric layer  $\epsilon$  is supposed to have values of the permittivity of  $\text{H}_2$  or  $\text{O}_2$  at  $20^\circ \text{C}$  are  $\approx 1$  obtained from [68], and that in between the polystyrene and water permittivities are  $[2.5, 100] \times \epsilon_0$  (in order of magnitude) obtained from [38]. The change in the equilibrium contact angle due to the applied electric field is given as

$$\cos \theta - \cos \theta_Y = \frac{\epsilon_0 \epsilon_r}{2d\gamma_{LV}} V^2 \sim \frac{[10, 10^3] \times 10^{-12} \frac{\text{N}}{\text{V}^2} \times 1\text{V}^2}{[50, 100] 10^{-6}\text{N}} \sim [10^{-6}, 10^{-5}] \quad (4.8)$$

Without applied field, the suspension has a contact angle in an interval of  $[30^\circ, 50^\circ]$  [38]. With applied field, although the estimated maximum change in the contact angle is very small (i.e.  $0.0008^\circ$ , if we consider  $\theta_y = 45^\circ$ ), the average contact angle changes following applied field frequency. This small and rapid variation in contact angle, synchronizes local flows that initiate the supply of particles in the meniscus, initiating the formation of clusters. The region surrounds the small groups of particles (dotted squared region in Fig. 4.4a), which limits the curved double arrows in Fig. 4.3 is named as **basin of attraction**. Electrophoresis coupled with capillary forces supply more particles to the meniscus [69]. Surface forces trap particles in the meniscus building up the capillary action to attract more particles [70], which increases the size of the basin of attraction. These particles start to accumulate near the contact line in the form of groups.

### Long term flows

The affected basins of attraction of these groups interact and rearrange according to the availability of particles. This leads to clusters of stable size. These clusters oscillate and follow the applied fields. Because of the oscillation of bigger clusters and low evaporation, with time the contact line recedes very slowly. This results in a sudden decrease in the distance between the particle concentrated regions near the contact line and the PPZ (Particle Pool Zone, see [35]). Initially, these two regions are separated by a long distance (see Fig. 4.4a), that gradually decreases (Fig. 4.4b,c) until the clusters start to dissociate due to interaction with PPZ and the enhancement of convection-like long scale flows related to evaporation. To consider the relevant role of existence

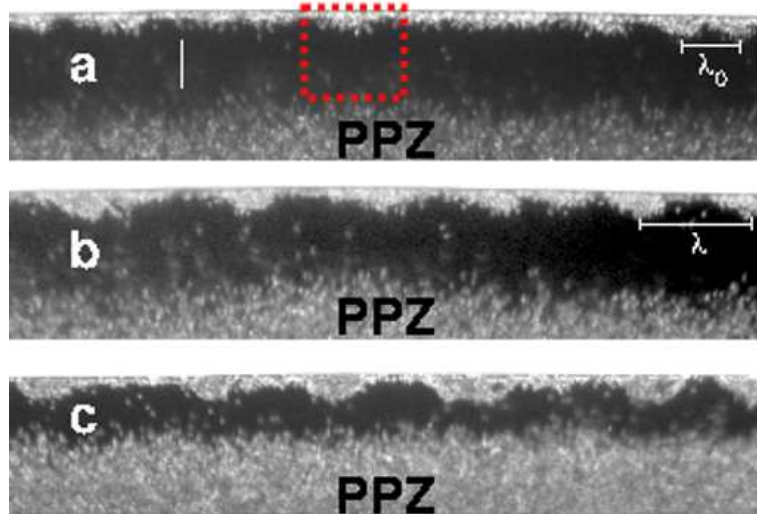


Figure 4.4: Frames a–c are front view samples of the contact line, captured at various time intervals showing different stages during the low evaporation experiment. Concentration is 0.5% (w/w) and the applied field is 1 V/mm and 1.4 Hz. A realization of  $\lambda$  and  $\lambda_0$  are shown. PPZ refers to the Particle Pool Zone (see [35]). The scale bar is 25  $\mu\text{m}$ . Subplots (a–c) are explained in the text. The red squared region in image (a) presents basin of attraction. The picture is reprinted from [1].

of evaporation, the experimental method is simplified by covering the experimental cell, keeping all the other experimental conditions unchanged, in this case, we are not able to get clusters. We explore further that the existence of free surface is mandatory for cluster evolution. Thus, we characterize the importance of electrokinetic effect for clusters evolution experimentally by using patterned substrates (section 3.4.2). We don't observe any cluster formation which directs to the fact that electrokinetic effect is not contributing directly to the formation of clusters, but it is fundamentally a free surface electric effect (e.g. electrowetting).

#### 4.1.2. Behavior of clusters

We explore the behavior of clusters as a function of the applied fields and initial particle concentrations of suspension. We observe that an increase in concentration and field strength affect the size of clusters in the same way, because either there are more colloidal particles available

in the affected basin of attraction or curved double arrows depicted in Fig. 4.3, cover larger area for fetching more particles (Fig. 4.5, Fig. 4.6) respectively. The smaller groups of particles are spatially distributed and separated initially by a distance  $\lambda_0$  shown in Fig. 4.4a. The affected basins of attraction of these groups interact with each other during long term flows in the direction of interaction. When, two small groups are closer enough to each other to be able to distribute the incoming particles from the bulk, they are not stable and merge together (Fig. 4.4b) to form a cluster. After, the clusters maintain their stable size, an array of clusters along the contact line have been observed. The average distance between these clusters when they stabilize is called **characteristic length**  $\bar{\lambda}$ . Fig. 4.4b presents an individual  $\lambda$  as well.

### The effect of applied field

The influence of applied field on the behavior of clusters in terms of characteristic length ( $\bar{\lambda}$ ) at fixed concentration of 0.5% (w/w) is shown in Fig. 4.5. Here, we observe a relative maximum in  $\bar{\lambda}$  at frequency 2.6 Hz for amplitude 1 V/mm. The time required for a volume element to complete a cycle in phase during the regular closed flows shown by curved double arrows in Fig. 4.3 is called recurrence time. The length of the fluid element path increases with an increase

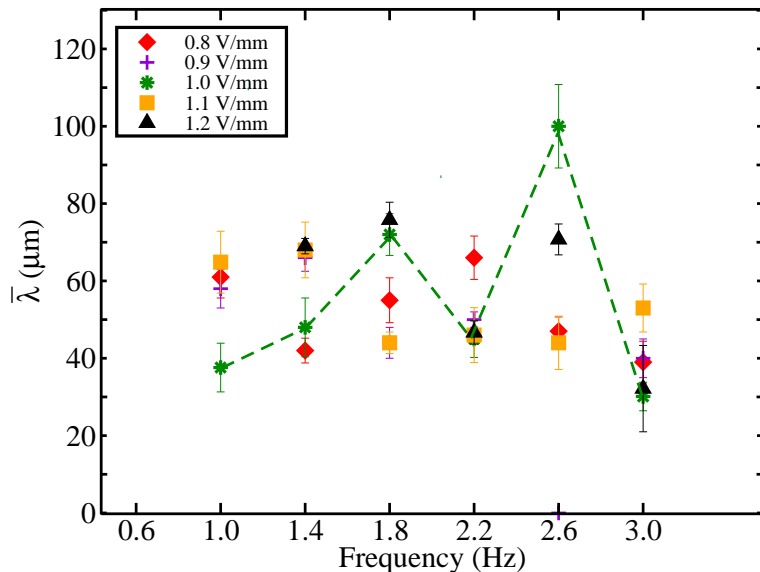


Figure 4.5: Characteristic length ( $\bar{\lambda}$ ) as a function of increasing applied frequencies for various amplitudes using 0.5 % (w/w) concentration. For a single amplitude 1 V/mm, relative maximum appears at frequency 2.6 Hz (green dashed lines are guides to the eye).

in field strength and, for having flows in phase, the frequency has to be increased. Higher applied field strength increases the length of these curved double arrows and consequently each cluster has more particles available in the affected basin of attraction. The increased capillarity also increases the size of basin of attraction to fetch more particles for cluster formation. Therefore, the characteristic length increases with an increase in the electric field strength.

### Effect of concentration

We report the effect of increasing initial particle concentration on the mechanism of clusters formation. Fig. 4.6 shows its influence on the characteristic length ( $\bar{\lambda}$ ) of clusters for different frequencies at fixed field strength of 1 V/mm. It increases monotonically with an increase in initial particle concentration. At frequency 1.4 Hz (see Fig. 4.6), for lower concentrations (up to 0.7 % (w/w)), the change in the characteristic length is small. However, we observe a bigger change in the characteristic length for higher concentrations, even when the applied field is unchanged.

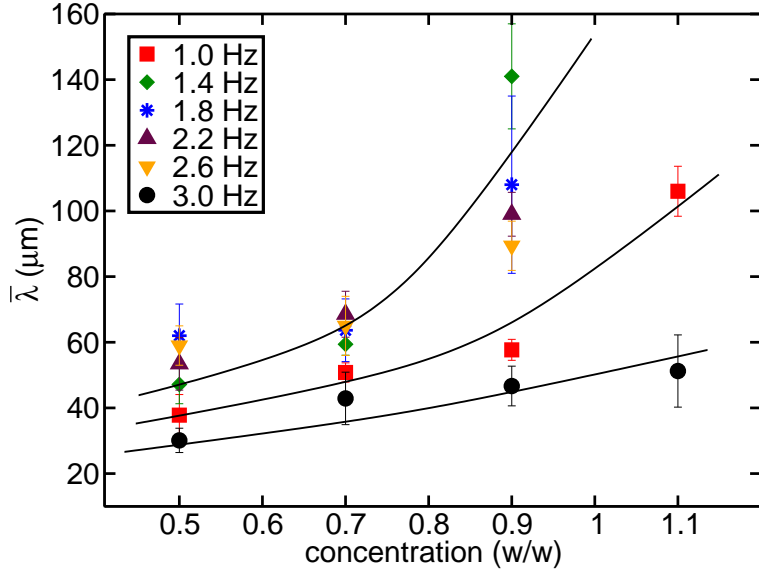


Figure 4.6: Characteristic length ( $\bar{\lambda}$ ) as a function of the increasing initial particle concentration for different frequencies at fixed field strength 1 V/mm. For each frequency,  $\bar{\lambda}$  changes monotonically with an increase in the concentration. Solid lines are guides to the eye. This plot is reprinted from [1].

## 4.2. High evaporation and colloidal deposits

Here, we explore experimental results on deposition of colloid in vertical deposition at higher temperatures with and without weak AC fields. We obtain well dried columnar deposits of colloid through rapid evaporation (during the experiments when thermal chamber is maintained at 63 °C). We focused to demonstrate the mechanism of deposition as a function of applied fields (0.8 V/mm to 1.2 V/mm and 1 Hz to 3 Hz) and initial particle concentration. To recall the experimental condition (see section 3.5 for details), Fig. 4.7 shows different stages resulting in situ, after the dispersion (100  $\mu$ l) is poured into the experimental cell and the electric field is the applied. Particles move towards the contact line due to high evaporation of the solvent (water) and concentrate there. Surface forces trap them into the meniscus. Then, these particles come closer to each other, building up the capillary action to begin dried deposits in the contact line (Fig. 4.7a). External fields continue to provide more particles approaching the contact line to support columnar deposits (Fig. 4.7b). When two recently built columns are closer to each

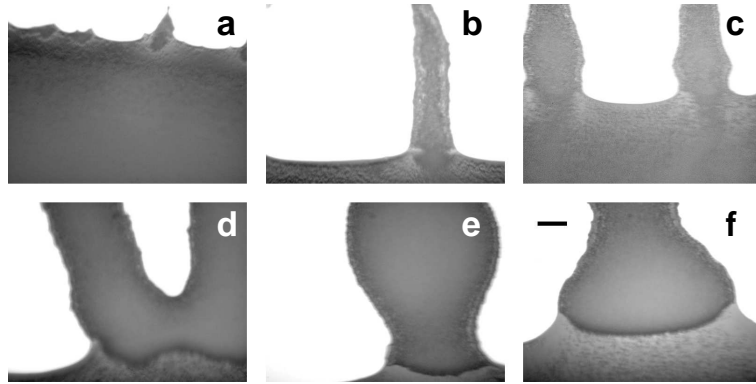


Figure 4.7: Front view of the contact line where frames a-f are captured at different increasing time intervals, show different characteristics of the deposition process, at 1 V/mm, 1.8 Hz, concentration - 1.1 % (w/w) at 63 °C. Scale bar is 50  $\mu$ m. Subplots a-f are explained in the text. This image is reprinted from [1].

other, they share the incoming particles from the bulk suspension (Fig. 4.7c), they are not stable and after some time merge together (Fig. 4.7d). After, these columns maintain their size, they oscillate in correlation with long range flows, that are independent of the short period of the applied electric field (Fig. 4.7e,f).

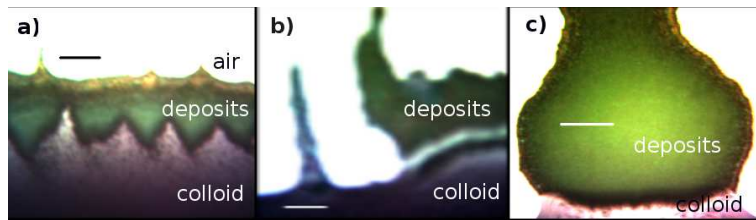


Figure 4.8: Snapshots of the process of deposition in situ at different temperatures and concentrations inside thermal chamber at 1.8 Hz and 1 V/mm, where the upper region in each image is the deposited part and the bottom region is the bulk suspension (colloid), the scale bar is 100  $\mu$ m. a) The building up of wet heterogeneous porous structure through out the experiment at 40 °C and concentration of 0.5 % (w/w). b) A wet structure incorporating a larger volume of fluid at 50 °C and concentration of 0.5 % (w/w). c) Well dried colloidal deposits due to rapid evaporation of the solvent at higher temperature (63 °C) and concentration of 1.1 % (w/w).

We observe different kinds of morphologies in situ at different higher temperatures and concentrations on applying AC fields shown in Fig. 4.8, where the images are arranged with an increase in temperature inside thermal chamber from left to right (40–63 °C). At lower evaporation (40 °C), we observe the building up of heterogeneous porous structure (Fig. 4.8a) in the form of thick triangular cluster array in the contact line. When the temperature is kept inside the thermal chamber at 50 °C, due to high evaporation a wet thick structure with a larger volume of fluid incorporated into it is observed (Fig. 4.8b). At higher temperature 63 °C we obtain well dried colloidal deposits due to rapid evaporation of solvent (Fig. 4.8c). Although, in situ these images provide limited information about the depositing structure because of their low resolution, we are

able to identify that the flux of particles that arrives to the contact line, determines the deposited structure. This flux is related to the evaporation-induced flow and on the local concentration of

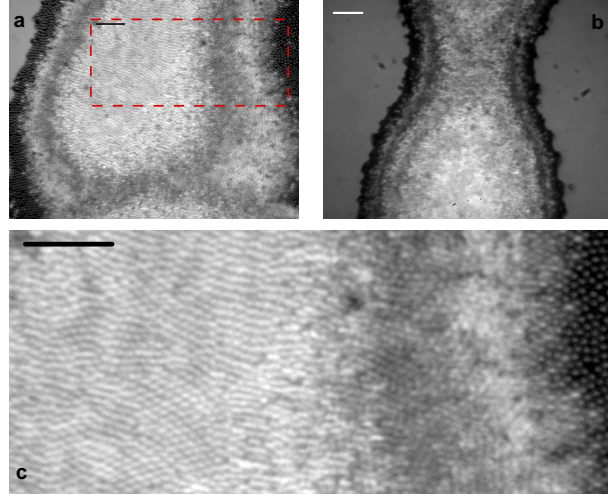


Figure 4.9: High resolution optical microographies of the upper layer of colloidal dried columnar deposits of multilayer in the middle far away from the boundaries. Experimental conditions are: 63 °C, concentration of 1.1% (w/w), 1.8 Hz, 1 V/mm. (a) and (b) are the optical micrograpries of the same column at different places and (c) is the magnified image of the red doted squared area in (a). Scale bar is 7.8  $\mu\text{m}$

particles near the contact line. Therefore, due to evaporation and the built deposited layer in the free surface, the particles from the bulk suspension will drag with different intensities towards the contact line. Thus, different deposited structures at various temperatures and concentrations depend on evaporation rates. We observe that the dried deposits on the ITO coated side of the substrate obtained during higher evaporation (63 °C) experiments with high resolution objectives (Fig. 4.9), closed packed well dried structures are obtained in the upper layer of vertical columns.

#### 4.2.1. Discussion

Fig. 4.10 shows the sketch of different depositing processes that have been observed during the high evaporation experiments, performed at higher temperatures. The contact line recedes because of evaporation of the solvent which results in a convective flows, that bring particles towards the meniscus from the bulk suspension (Fig. 4.10a). Hence, concentration of the colloidal particles inside the cell is not constant throughout the experiment because of the evaporation of the solvent from the suspension and also the concentration in PPZ (Particle Pool Zone) and in the bulk suspension are not the same [71]. Surface forces trap particles in the contact line and bring them closer to each other to build up capillary action. The capillarity initiate the deposition of compact layer of colloidal particles in the contact line (Fig. 4.10b). During the deposition due to capillary effect, the evaporation of the solvent becomes regular which induces hydrodynamical flows through porous structure to stimulate further growth of the dried deposits. Next, rapid variation of the contact angle (having the estimated value given in equation 4.8) by electrowetting effect on applying AC field, generates short range closed flows (curved double arrows of Fig. 4.3)

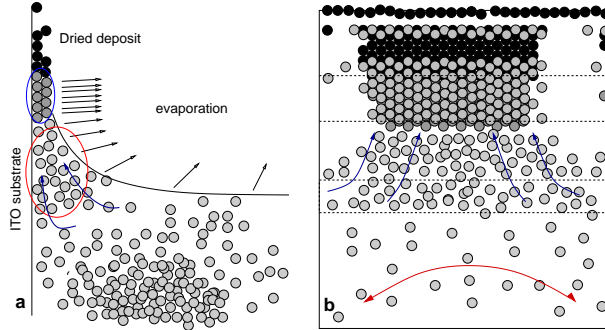


Figure 4.10: Schematic representation of the deposition process of a column. Lateral view (a) and front view (b), where capillary flows (up-going curved arrows), evaporation (straight arrows), and large scale convection flows (double curved arrow) can be seen. For details see the text. This sketch is reprinted from [1].

which continue the supply of particles supporting columnar deposition. Nevertheless, the capillary flows (Fig. 4.10) overcome them and continue the growth of the columns as the contact line recedes. Finally, we obtain the columnar deposits made of multi-layer structures.

The typical parameters that influence our system obtained from [38] are

$$\gamma \approx 1 \times 10^{-1} \text{ N/m} \quad (4.9)$$

$$\eta \approx \eta_{\text{water}} = 1 \text{ cP} = 10^{-3} \text{ Kg/(m s)}$$

$$\rho \approx \rho_{\text{water}} = 1 \text{ g/cm}^3 = 10^3 \text{ Kg/m}^3$$

$$L \approx 10^{-6} \text{ m}$$

$$v \approx 10^{-6} \text{ m/s}$$

$$Re = \frac{\rho v L}{\eta} \approx 10^{-6}$$

$$Ca = \frac{\eta v}{\gamma} \approx 10^{-8}$$

$$(4.10)$$

where  $\gamma$  is the surface tension of diluted suspension in water and supposed to have estimated value in order of magnitude given in equation 4.9 similar to water surface tension [38].  $\eta$  is the viscosity,  $\rho$  is the density of this suspension which is considered to have value in order of magnitude of density of water,  $L$  is the diameter of the colloidal particles and  $v$  is the characteristic velocity. From the small value of Reynolds number ( $Re$ ), we can infer that the colloidal particles act like inertial ones therefore approximately follow the fluid flow [71]. Consequently, the flows in porous structure is dominated due to capillary forces ( $Ca$  is small capillary number) [72].

Furthermore, to identify the relevant role of the external field on formation of columnar ordered colloidal deposits, we perform the experiment with and without applied field. Fig. 4.11 shows the dried deposits of the same experiment both without (above the green line) and with (below the green line) field. This indicates with field, we obtain elongated columnar deposits with regular order and that without field we obtain less ordered dried deposits. The regular order shown in Fig. 4.12 which appears between columnar deposits is related to the availability of colloidal particles and due to the homogeneous character of the colloid at the beginning of the experiment

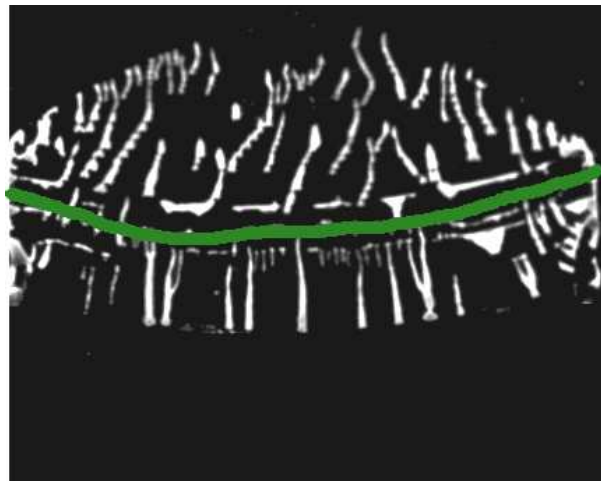


Figure 4.11: Photograph of the dried deposits of colloidal particles (field of view is 12.9 mm) with crossed polarizers where deposits above the green line are obtained without field and below it are with the applied field. Concentration of 0.7 % (w/w). Field - 1 Hz and 1 V/mm. This image is adapted from [1].

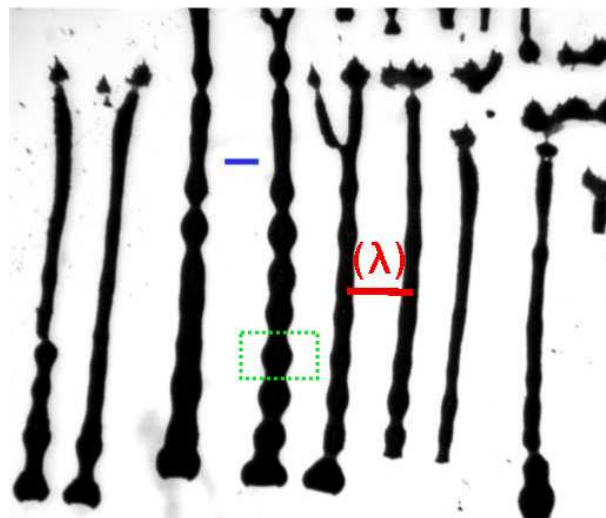


Figure 4.12: Low magnification (2X) bright field image of dried deposits of colloidal particles on ITO coated side of the substrate. The scale bar (blue) is 100  $\mu$ m. Concentration of 0.5 % (w/w). Field during deposition - 1.8 Hz and 0.8 V/mm. The red line presents the distance between consecutive columns ( $\lambda$ ) and the green squared enclosed width of the column. This image is modified from [1].

and to the fact that the PPZ is also homogeneous during the experiment.

#### 4.2.2. Mechanisms

We focus to explore the effects of the two parameters on the behavior of columnar deposits in vertical deposition experiments: the applied weak AC fields and initial particle concentrations of the suspension. These effects are investigated in terms of characteristic length  $\bar{\lambda}$  (the average distance between the columns shown in Fig. 4.12 by red line presents an individual  $\lambda$ ) and characteristic width (average thickness of the columns shown in Fig. 4.12 by square).

##### Effect of the field strength

We investigate the influence of the field strengths on the behavior of the dried deposits. Fig. 4.13 shows the characteristic width of columns measured macroscopically (see section 3.5.1 for details), for the different applied voltages (0.8–1.1 V/mm) at fixed initial concentration 0.5 % (w/w) and for different frequencies. At 1 Hz frequency see Fig. 4.13, the characteristic width is an increasing function of the applied field strength. This increase in the characteristic width of the columns due to external field can be understood from the fact of increase in the size of basin of attraction. Curved double arrows of Fig. 4.3 that present the AC field-induced closed flows, cover larger area for fetching more particles to form columns of thicker width.

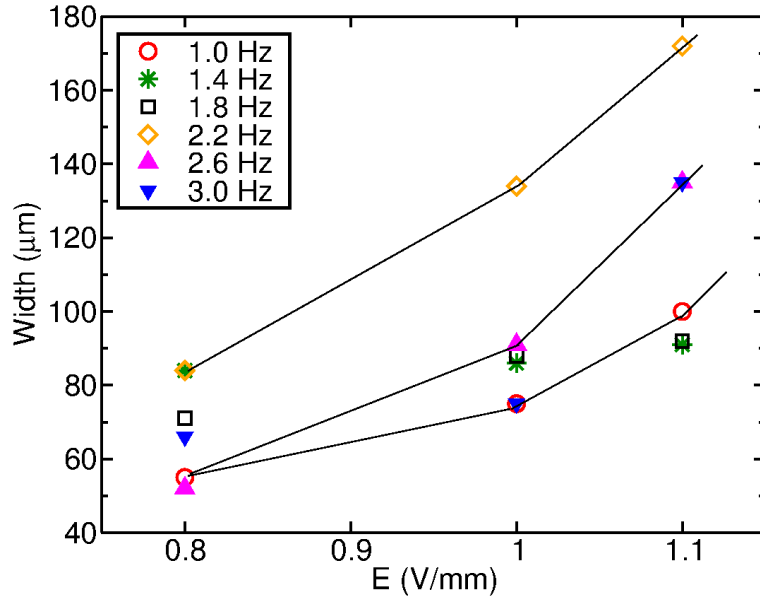


Figure 4.13: Average width of the columns as a function of the field strength for different frequencies at fixed concentration of 0.5 % (w/w). For each frequency, width is increasing with an increase in the field strength (black lines are guide to the eye). This plot is adapted from [1].

##### Effect of concentration

We study the effect of increasing initial particle concentrations on the behavior of columns formation. Fig. 4.14 shows its influence on the characteristic length ( $\bar{\lambda}$ ) between columns for

different frequencies at fixed field strength of 1 V/mm. At frequency 1 Hz see Fig. 4.14, the characteristic length has larger values for higher concentrations (1.1 % (w/w)) of the suspension.

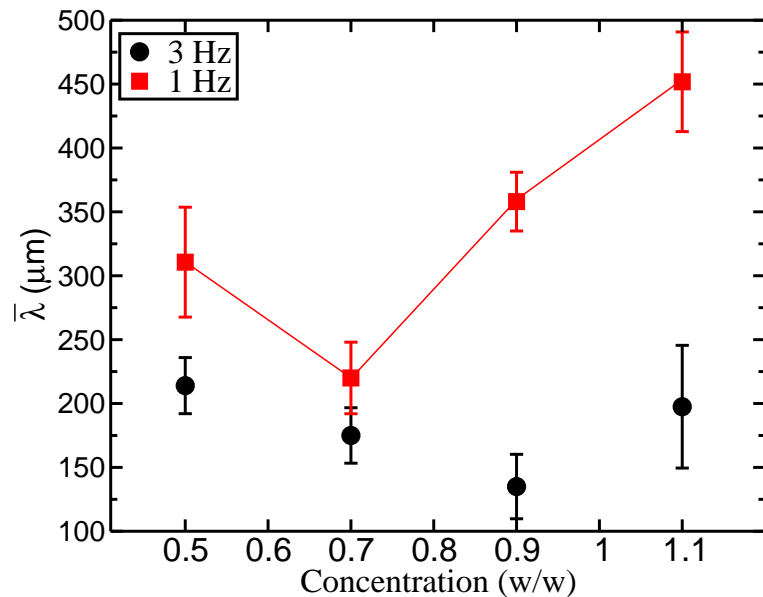


Figure 4.14: Characteristic length ( $\bar{\lambda}$ ) between columns as a function of the increasing initial particle concentration for different frequencies at fixed field strength 1 V/mm.



## Part II

# Spin-coating of colloidal systems



# Chapter 5

## Introduction

### 5.1. Spin-coating basics and theory

spin-coating is a well known technique that has been used to make uniform thin films to flat substrates for decades. Many research groups have investigated this phenomenon both theoretically and experimentally [2, 38, 73–77, 77–87]. Walker *et al.* [73] were the first who used spin-coating process for studying the physical characteristics of paints and emulsions. spin-coating is widely used for making polymer thin films of uniform thickness over large areas (e.g. photoresists or protective coatings) [82, 88–90]. To do so, a polymer solution is prepared using a volatile solvent, that evaporates rapidly during spinning, leaving behind a uniform polymer film [88]. Spin-coating process is very fast, reproducible, simple and needs less material [91]. Further, explanations about spin-coating of Newtonian fluids can be obtained in the references [74, 75, 81, 92, 93]. In spin-coating, the thickness and the uniformity of the films are important and strongly dependent on the key parameters that include: the spin time and speed, the viscosity of fluids, the density and the evaporation rate of the fluids and the substrate surface properties [38, 71, 91].

#### Spin-coating theory

The dependence of spin-coated film thickness on the key parameters and the information on the flow and fluid properties for the rotating disk or spin-coating systems, have been reported in various theoretical continuum models [74, 75, 77, 85, 94]. Emslie *et al.* [74] model describes the thinning of a Newtonian fluid layer on the spinning disk without considering the evaporation of solvent. The model assumes the set of simplifications that based on viscous forces due to fluid properties and the centrifugal forces of the spinning. It also considers the approximations of lubrication theory which provides the balance between viscous and centrifugal forces per unit volume for a Newtonian fluid in cylindrical polar coordinates ( $r, \theta, z$ ) is [74]

$$-\eta \left( \frac{\partial^2 u_r}{\partial z^2} \right) = \rho \omega^2 r \quad (5.1)$$

where  $\eta$  is absolute viscosity,  $\rho$  is fluid density,  $u_r$  is the radial velocity,  $\omega$  is the speed of rotation and the axis  $z$  is perpendicular to the rotating plane (see Fig 5.1). Integrating eq. 5.1 with respect

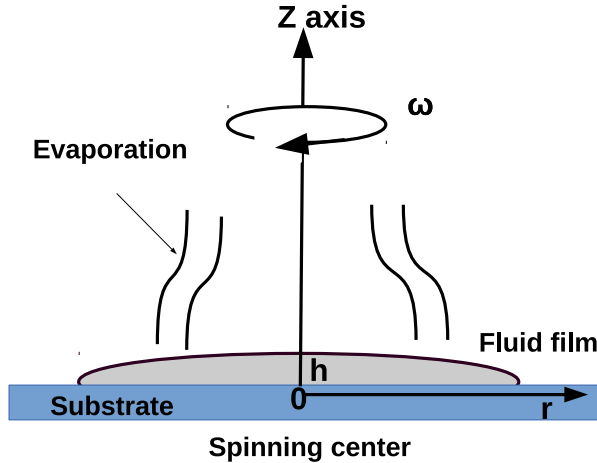


Figure 5.1: Schematic representation of spin-coating process, where  $\omega$  is the speed of rotation,  $h$  is the film thickness and  $r$  is the radial distance from the center of rotation. The image is adapted from [85].

to  $z$  and assuming proper boundary condition with zero shears at the free surface ( $\partial u / \partial z = 0$ ) at  $z = h$ , and that  $h$  does not depend on radial position, eq. 5.1 leads to

$$\frac{dh}{dt} = -2Kh^3 \quad (5.2)$$

where  $K = \frac{\rho\omega^2}{3\eta}$ .

Integrating eq. 5.2 using suitable limits such that at  $t = 0$ ,  $h = h_0$ , where  $h_0$  is the initial thickness of fluid film, we obtain

$$h(t) = \frac{h_0}{(1 + 4h_0^2 K t)^{1/2}} \quad (5.3)$$

Eq. 5.3 presents a simplest model of spin-coating, that avoids the effect of shear stress (under no slip condition).

### Inclusion of evaporation

The final spin-coated film thickness also strongly depends on the evaporation. Meyerhofer [75] has added a constant evaporation term to the thinning rate in eq. 5.2. He assumes in his model that the thinning rate of rotating disk systems includes two different stages: early stages are flow dominated and later stages are evaporation dominated. Eq. 5.2 with constant evaporation term becomes

$$\frac{dh}{dt} = -2Kh^3 - E \quad (5.4)$$

where  $E$  is the evaporation rate.

Introducing the evaporation rate term, the rate of change in the solvent height ( $L$ ) is (see ref. [75])

$$\frac{dL}{dt} = -1(1 - C_s) \frac{2\omega^2 h^3}{3\nu} \quad (5.5)$$

where  $C_s$  is the concentration of the solute ( $= S/(S + L)$ ) and  $\nu$  is the kinematic viscosity of solvent ( $= \frac{\eta}{\rho}$ )

Later on, Cregan *et al.* [85] proposed that the evaporation rate and viscous flow rate are simultaneous. According to Cregan's model for continuum fluids, the final spin-coated film thickness ( $h(t)$ ) is

$$h(t) = \frac{S_0}{L_0} \left( \frac{E}{\alpha} \right)^{\frac{1}{3}} \quad (5.6)$$

where  $S_0$  and  $L_0$  are the initial solute and the solvent thickness if they were considered separated and  $\alpha = \frac{2\omega^2}{3\nu}$  ( $\omega$  is the spinning rate,  $\nu$  is the kinematic viscosity of solvent and  $E$  the evaporation rate of solvent as before) [85]. Lately, our group has proposed experimental work based spin-coating model for colloidal systems taking into account the evaporation of the solvent and is derived by modifying the existing Cregan's model [71, 95]. This model helps to study final spin-coated colloidal deposit thickness. Further explanations about spin-coating model for colloidal systems can be found in chapter 7. In addition, more discussions for models for non-Newtonian fluids are available in references [78, 96].

## 5.2. Spin-coating of colloids

More recently, spin-coating has been introduced in colloids science to fabricate colloidal crystals with regularly ordered particles [2, 86, 91, 97, 98].

**Using less volatile medium** for colloidal dispersion, Jiang *et al.* [97] were the first producing 3-d colloidal crystals by spin-coating. They controlled the thickness of spin-coated film by tuning experimental parameters (e.g. speed and time of spinning). Jiang used suspension of colloidal particles (in nanometer size range) dispersed in polymer solution (less volatile medium). They achieved colloidal films of six bright colored arms after several minutes of spinning as shown in Fig. 5.2-A. They obtained structures that were composed of hexagonal layers [97]. Interestingly, in these structures the particles were not in touch with each other (Fig. 5.2-B), but the layers were arranged in such a way that the particles of one layer were in contact with the particles of adjacent layers.

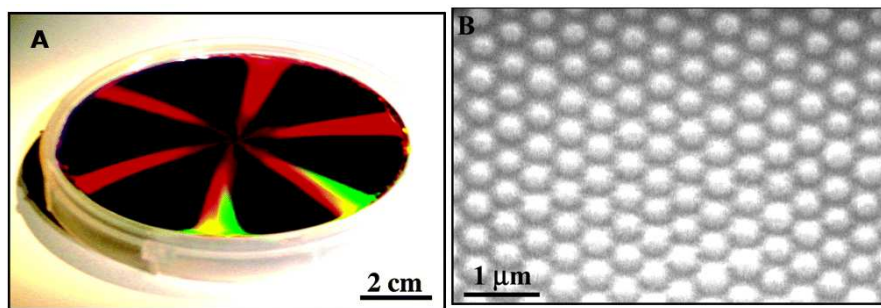


Figure 5.2: Spin-coated colloidal deposits of 325 nm diameter colloidal spheres suspended in a non-volatile solvent on a 4-inch silicon wafer. Spin speed is 600 rpm and spin time is 120 seconds. A) Image of a 3-d film illuminated with white light. B) Magnified scanning electron microscopic (SEM) image of a spin-coated colloidal crystal-polymer. This figure is adapted from [97].

**Using volatile medium** for colloidal suspension, some research groups performed spin-coating experiments to make well ordered colloidal crystals as well as to understand the dynamics of the structure formation [2, 38, 77, 86]. They obtained similar results but in short time (smaller than a second) and their experiments showed 4- or 6-fold symmetry (bright colored arms) depending on the type of solvent and the spinning velocity they used. A summary of spin-coated colloidal crystals obtained in their experiments are shown in Fig. 5.3 and Fig. 5.4. Mihi *et al.* [86] used silica particles in nanometer sized range dispersed in volatile solvent (ethylene glycol and ethanol) (see Fig. 5.3-left). They controlled the thickness and orientation of spin-coated colloidal films by spinning rate as well the time for the evaporation of the solvent (Fig. 5.3-right). Arcos *et*

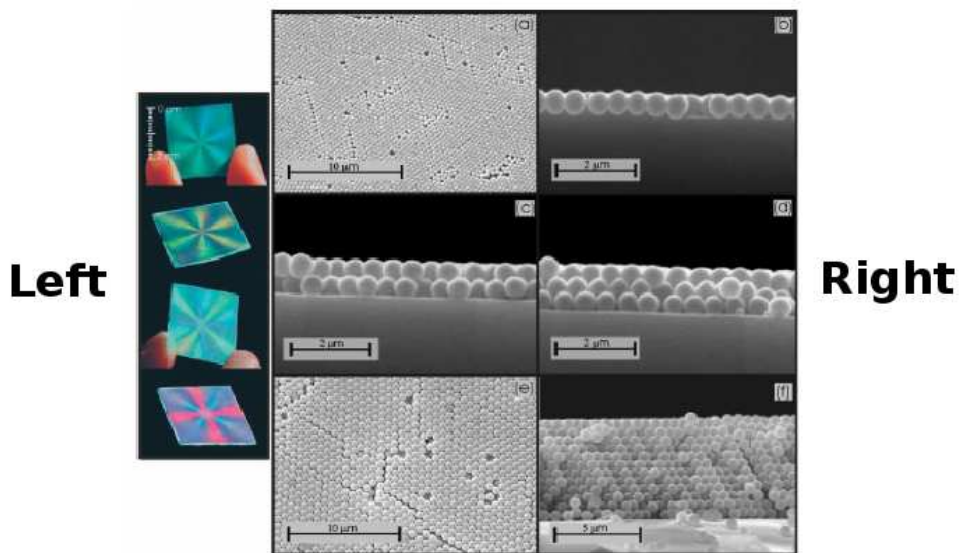


Figure 5.3: Spin-coated colloidal deposits of polymeric particles suspended on mixtures of different solvents. Left: images of the optical diffraction patterns observed in the spin-coated crystals, under solar illumination showing two distinct symmetries. Right: SEM images (a–f) of the same spin-coated samples at different rotation rates. This figure is modified from [86].

*al.* [2] used colloidal dispersion of higher concentrations of 40%w/w of silica particles (diameter 458 nm) dispersed in volatile solvent (ethanol / acetone) to perform spin-coating experiments. A sample of their experimental results are shown in Fig. 5.4-top. The SEM images near the center of samples in Fig. 5.4-bottom indicate that the obtained structures are not like well ordered crystals but an **Orientationally correlated polycrystal (OCP)**. They observed the structures mostly oriented in the radial direction about the center of rotation. This long range orientational order is due to axisymmetric experimental setup.

Lithography combined with spin-coating has also been used [99–101] to make well ordered colloidal crystals. Firstly, a template is prepared on a substrate by lithography. Secondly, colloidal suspension of volatile medium is spin coated slowly to fill the trenches. Lastly, the spinning speed is increased to remove extra particles. The particles could adopt the desired crystal structure if the dimensions of trenches are scaled carefully. Colloidal crystals with a specific structure and orientation are achieved after removing the template.

Lately, Giuliani *et al.* [102] provided insights for the spin-coating of colloidal systems that

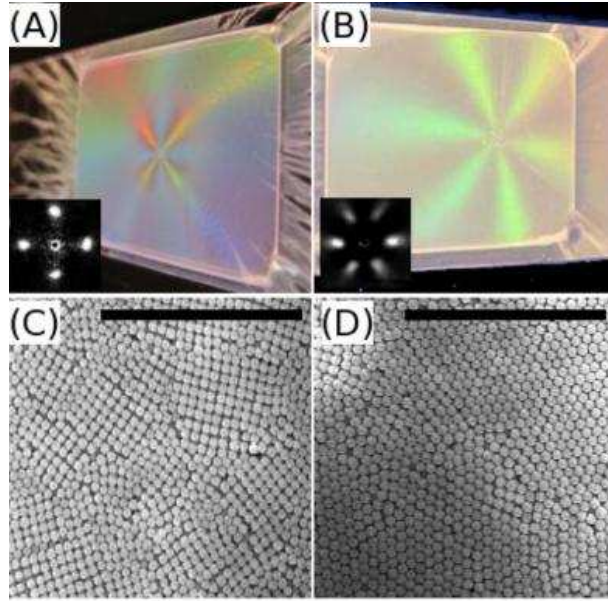


Figure 5.4: Top: (A) and (B) are the white-light reflections of spin-coated colloidal films of silica spheres dispersed in (A) acetone and (B) ethanol solvents, onto cover-slides at 3000 rpm, displaying 4-fold and 6-fold symmetries. Their laser diffraction patterns are shown in the left corners. Bottom: (C) and (D) are the SEM images near the center of the same samples. The scale bars are 10  $\mu\text{m}$ . Figure is reprinted from [2].

combine the flow and the properties of fluids. They used the suspension of sub-micron silica particles suspended in volatile medium (Methyl Ethyl Ketone, MEK) and studied the dynamics of colloidal crystal structure formation by spin-coating, using high-speed imaging and associated it with speed of rotation. Their results illustrated the transient dynamics of long-range orientational order and presented the symmetry transitions and the thinning dynamics of colloidal suspension during spin-coating. In these kinds of systems, the measured thickness of dried spin-coated film in regular intervals from the spinning center may prove the non planarization phenomenon [38].

As discussed before, spin-coating is a simple, fast and reproducible technique to fabricate colloidal crystals [2, 76, 86, 97, 103, 104]. Nevertheless, using higher concentration of 40% w/w suspensions, colloidal films with 4-fold, 6-fold or mixed symmetries are obtained (see Figs. 5.2, 5.3 and 5.4). The emergence of symmetric radial colored arms in spin-coated colloidal crystal are orientationally correlated because of the axial symmetry imposed by spinning axes [2]. To avoid the OCP character, to make colloidal-films with translational order structures and to control the orientation, electric fields were applied during spin-coating [105]. It has been studied that, in an external electric field hydrodynamic flows are influenced through dielectrophoretic confinement of the suspension that results colloidal crystals in predefined direction [105]. Pichumani *et al.* [71, 105] controlled the orientation of colloidal crystal by applying non-uniform alternating electric fields during the spin-coating. Colloidal dispersion of silica particles (diameter 458 nm) dispersed in Methyl Propyl Ketone (MPK) of  $\sim$ 40% w/w concentration was used for their experiments. They investigated that the external field might break the axial symmetry. The application of these external fields can decrease the reproducibility of spin-coating method and can lead the

system towards complexity.

Here, we use photolithography followed by spin-coating method to prepare polycrystals mostly consisting of monolayers. First, a pattern of photo-resist hexagonal pillars is made on a cover slide by lithography. Then, colloidal dispersion of silica particles (diameter 458 nm) dispersed in a volatile medium (ethanol) of 40% w/w concentration are spin coated at constant spinning velocity to make polycrystals. With this simple surface treatment, we are able to break the axial symmetry from the spin-coated film. Spin-coating experiments which have been explored previously, were performed using colloidal dispersion of non magnetic particles of higher concentrations of  $\approx 40\%$  w/w, that caused the characterization of structure formation challenging. On the contrary, Pichumani *et al.* [106] used dilute suspensions of superparamagnetic particles for spin-coating experiments with and without magnetic fields. They obtained sparse structures that consist of quasi 2-d clusters of particles. On applying external magnetic fields during spin-coating, they observed an increase in the viscosity of colloids. Also, the clustering dynamics of superparamagnetic suspensions in magnetic field may be influenced as a consequence of magnetic dipole interactions.

### 5.3. Colloids under shear stress

Hard sphere systems show a phase diagram in equilibrium, that consist of four states depending on the increasing volume fraction of the suspension. The suspension is supposed to be in a liquid state at low concentration. It initiates to crystallize locally with an increase in concentration along with fluid regions. At concentration of  $\phi = 0.545$  the system crystallizes mostly in a rhcp lattice, whereas, the crystal goes to a glass state for the concentration within the range of  $\phi = 0.58 - 0.63$ . At higher concentration the crystal state is restored. Furthermore, explanations about the phase diagram are given in [107]. This phase diagram can be modified by applying shearing that adds further three dynamical states depending on the strength of the shearing [108, 109]. At low shear rates, adjacent layers are displaced from each other in a zig-zag movement. With an increase in shear rate, the layers initiate to move linearly, and finally, they get disordered at shear-induced melting point.

Emslie *et al.* [74] avoided the effect of shearing force arised from the co-rotating air flow to the final film thickness  $h(t)$  in terms of initial film thickness  $h_0$  given in eq. 5.3. Because, air has finite viscosity which causes a shearing stress at the interface during spinning. Research has been done to include the effect of shearing stress in the mathematical modeling of spin-coating [87]. Integrating the left side of eq. 5.1, using suitable boundary conditions, the shear stress  $\tau_{rz}$  imposed by external air flow can be derived as

$$\tau_{rz} = \rho\omega^2 r(h - z) \quad (5.7)$$

Eq. 5.7 shows that shear stress is proportional to the square of spinning speed ( $\omega^2$ ). It is concluded that air shearing force increases the rate of thinning [87]. The magneto-rheological effect is mostly associated to the field-induced magnetization of the suspended magnetic particles. The suspensions have a low viscosity without magnetic fields. The particles become magnetized on applying magnetic fields and attract each other through magnetic dipole interactions along the field lines and form clusters that causes a large yield stress. This behavior is also known as a large shear rate-dependent apparent viscosity and increased viscoelasticity induced by the applied magnetic field [110].

Lately, Shereda *et al.* [98] studied experimentally, the spin-coating of colloidal suspension of PMMA spheres (poly(methyl-methacrylate)) dispersed in dioctyl phthalate (a non-volatile solvent of viscosity,  $\eta = 718$  cP [38]), of higher concentration  $\sim 35\%$ . They investigated the effect of the shear stress on the crystalline quality using this viscous suspensions in terms of Peclet number (measured from equation eq. 5.7)

$$Pe \propto \tau_{rz}a^3/K_bT \quad (5.8)$$

$$Pe = \frac{6\pi\rho\omega^2r(h-z)a^3}{K_bT} \quad (5.9)$$

where,  $k_b$  is the Boltzmann constant and  $T$  is the absolute temperature and the factor  $6\pi$  in eq. 5.9 is included to define  $Pe$  at the infinite dilution limit [9]. Using this analysis they observed the transition in the viscous suspension, from non-crystalline to crystalline order that correlated well for a  $Pe \sim 1$  [98].

Here, we perform spin-coating experiments to study magnetorheology of mixed colloidal suspensions. The magneto-viscosity of hybrid diluted colloids of carbonyl iron+silica particles in cyclohexanone is derived from the surface coverage of the spin-coated deposit [95]. These spin-coating results are compared with the results obtained from classical magnetorheometry [110] (see chapter 7 for further details).



# Chapter 6

## Experimental Setup

This chapter explains the experimental techniques and methods for spin-coating of colloids. The provided spin-coater is modified to perform experiments in external magnetic fields, using mixed colloidal particles (carbonyl iron and silica) suspension. The commercial spin coater is also used for performing experiments, to build up colloidal polycrystals of monolayer, from suspension of nonmagnetic silica particles on photo-patterned substrates.

### 6.1. Magnetorheology experiments

#### 6.1.1. Materials

##### Suspension

Carbonyl iron particles of micrometer size (iron particles prepared by thermal decomposition of iron pentacarbonyl are called carbonyl iron particles) are dispersed in water or cyclohexanone, to prepare diluted suspension. Also, the suspension of mixed particles (silica and carbonyl iron) at 4% (w/w) concentration is made in (water for trial experiments) cyclohexanone for all real experiments. We prepare the suspension by mixing equal mass of the two kind of particles. The

Particles	Silica	Carbonyl iron
Molecular formula	$\text{SiO}_2$	Fe (highly pure (97.5%) iron
Size [ $\mu\text{m}$ ]	0.75	2 and 3
Density [g/cm <sup>3</sup> ]	1.8	7.87
Solubility in water	insoluble at normal conditions	insoluble
Solubility parameter $\sigma_t$ [MPa <sup>1/2</sup> ]	35.3 e.g. in [111]	117 e.g. in [112]
Melting point [°C]	1600	1536

Table 6.1: Physical properties of silica and carbonyl iron.

physical properties of the particles are almost similar and are given in the table 6.1 except the density. The physical characteristics of the solvents are similar and they are explained in the table 6.2. To prepare homogeneously dispersed suspension, we follow the procedure explained in [38]. Silica particles of 0.75  $\mu\text{m}$  diameter obtained in dried form (Angstromsphere<sup>TM</sup>, commercially available from Fiber Optic Center. inc.) are weighed after drying overnight at 150 °C inside

Solvent	Water	Cyclohexanone
Molecular formula	H <sub>2</sub> O	(CH <sub>2</sub> ) <sub>5</sub> CO
Density [g/mL] at 25 °C	0.9987	0.9478
Solubility parameter $\sigma_t$ [MPa <sup>1/2</sup> ] at 25 °C	47.8	19.6
Viscosity [cP] at 20 °C	1	2
Surface tension [mN/m] at 25 °C	72.8	32.92

Table 6.2: Physical properties of water and cyclohexanone where the solubility parameters are obtained from [112].

the oven to reduce the absorbed humidity. After thermalization at room temperature when the silica particles are taken out of the oven, they are mixed with the desired weighed carbonyl iron particles. Then the decided volume of the solvent is added to prepare the suspension of mixed (silica and carbonyl iron) particles and is kept for ultrasonication overnight. The well dispersed suspension is later used for performing experiments. The dispersion of carbonyl iron in water becomes rusted after some time due to oxidation therefore cyclohexanone is used as a solvent for our actual experiments. Also, cyclohexanone is a good substitute compared to water, because of its similar properties except higher viscosity (which is good for reducing sedimentation). Moreover, silica particles are mixed to keep carbonyl iron particles in the suspension to reduce the rate of sedimentation because of their higher density [113].

### Characterization of the size of particles

The size of silica and carbonyl iron particles as provided, can be characterized by using DLS (Dynamic Light Scattering) technique. We prepare very diluted and well dispersed suspension of silica or carbonyl iron particles in cyclohexanone or water. The obtained results characterizing the size of carbonyl particles are shown in Fig.6.1 and those for silica particles in Fig. 6.2. The small difference in the average size of the particles obtained from the DLS results (when they are wet or suspended in solvent may swell) from the provided size (in dry form) might be as a result of the relative solvency behavior of a specific solvent known as Hildebrand solubility parameter [114]. The standard solubility parameter values are obtained from [111, 112] and are given in the tables 6.1 and 6.2 for particles and solvents respectively that we use in our experiments.

### Substrates

We use microscopic glass substrates of size 38×25×1 mm<sup>3</sup> for all the experiments. The substrates are placed in acetone for fifteen minutes to remove the organic materials and then transferred to a basic cold piranha solution that is composed of H<sub>2</sub>O : NH<sub>4</sub>OH : H<sub>2</sub>O<sub>2</sub> in ratio of 5:3:1 respectively for one day, after they are kept in ultrasonic bath at 63 °C in hot piranha solution for forty minutes. The substrates are after rinsed with ultra-pure water and dried with filtered air blow. Freshly cleaned and dried substrates are used for each experiment.

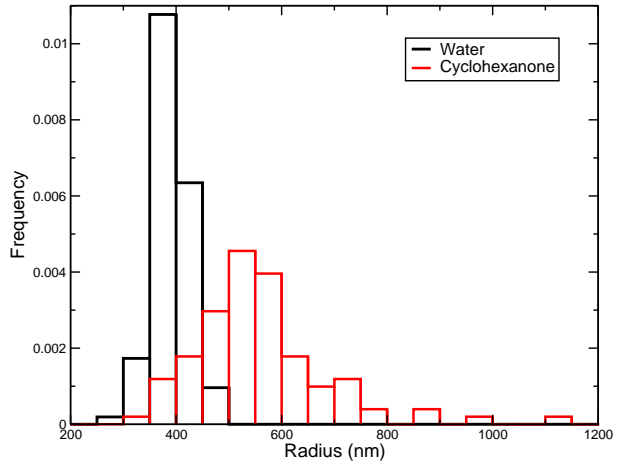


Figure 6.1: Normalized histograms, characterizing the size of carbonyl iron particles dispersed in water (black line) or cyclohexanone (red line).

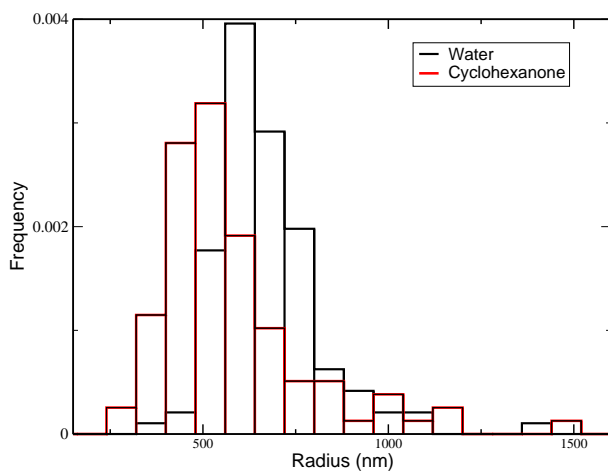


Figure 6.2: Normalized histograms, characterizing the size of the silica particles, suspended in water (black line) or cyclohexanone (red line).

### 6.1.2. Experimental system

The experimental setup to perform the experiments using a commercial spin-coater (Laurell technologies, WS-650SZ-6NPP/LITE/OND) in external magnetic field is shown in Figure 6.3. Magnetic field is applied by a pair of Helmholtz coils (Fig. 6.3A and B). The Helmholtz coils are arranged in such a manner that the substrate rotates with desired speed in the region of uniform axial magnetic field (Fig. 6.3C). The magnetic fields are applied by changing the current in the

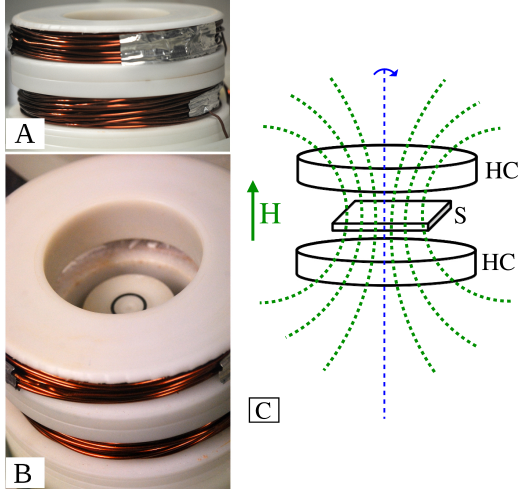


Figure 6.3: Experimental setup; (A) a pair of Helmholtz coil, (B) a spin-coater and (C) the sketch of experimental setup and the magnetic field lines where HC: Helmholtz coil; S: Substrate and the curved arrow shows the direction of the spinning. This image is reprinted from [95].

Helmholtz coils with an external power supply. Current intensity and magnetic field strength is obtained by using Gaussimeter that works on the basis of Hall effect. We switch on the DC power supply and adjust the current, later we measure the magnetic field induced by this current in the Helmholtz coils placing the sensor in the middle of the substrate inside the spin coater before spinning. We obtain several values of magnetic field on changing current given in Fig. 6.4.

### 6.1.3. Experiment

The spin-coater is programmed at a desired rotation rate  $\omega$  and the experiments are performed with and without applying magnetic field at room temperature. The freshly prepared suspension after fifteen minutes of sonication is used for each experiment. The desired magnetic field is applied and  $100 \mu\text{l}$  of suspension is pipetted onto the spinning substrate. The field is turned off after the suspension is dried. The experiments are repeated for the range of magnetic fields and rotation rates (2000 to 7000 rpm).

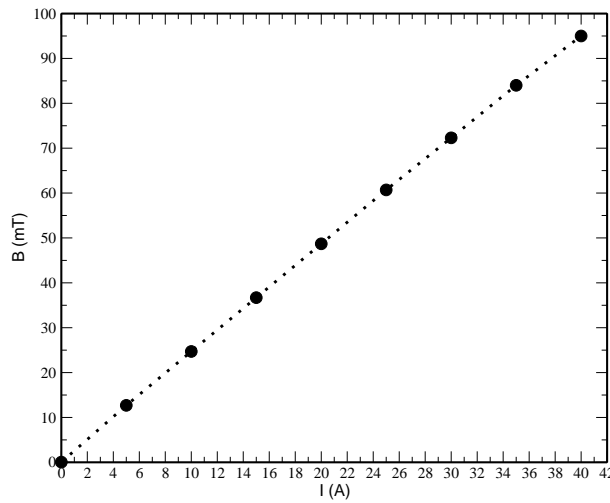


Figure 6.4: Current induced magnetic field curve, where by adjusting current on the DC power supply leads to a range of magnetic fields.<sup>1</sup>

#### 6.1.4. Measurements

The images of dried spin-coated deposits on the substrates are captured at 2 mm intervals from the center of spinning with objective of 10X magnification. Next, they are enhanced and thresholded using GIMP. An example of the original image (A) and its respective modified form (B) is displayed in the Fig. 6.5. In this way, the images of the dried deposits of all experiments

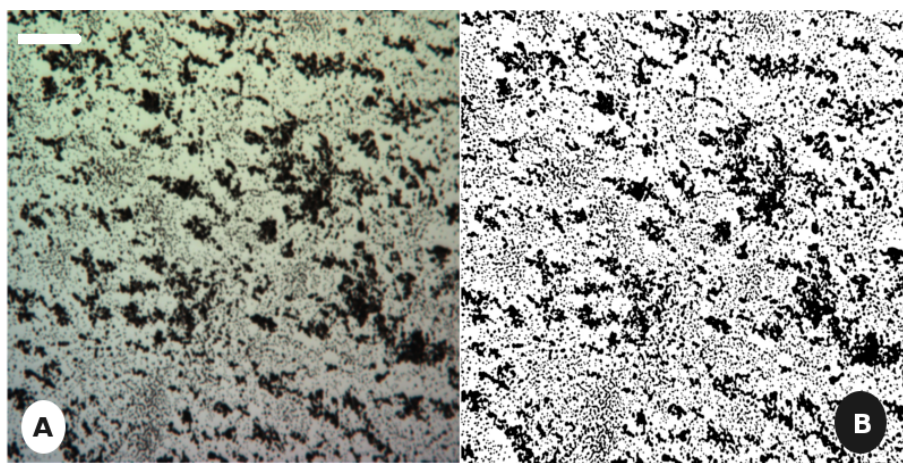


Figure 6.5: Images of spin-coated deposits on the top of the substrate at 8 mm from the spinning center. Scale bar is  $100 \mu\text{m}$ . (A) is original image and (B) is the modified enhanced and threshold form of the respective image. Conditions are the following, magnetic field  $B = 36.7 \text{ mT}$ , Spinning rate is 5000 rpm.

have been modified first before analyzing through home made routines in Octave, where the area occupied by the particles relative to total area of the region is measured. This surface

<sup>1</sup>Magnetic field: in vacuum,  $B$  (magnetic field in Tesla T) and  $H$  (magnetic field strength in A/m) are proportional to each other i.e.  $H = B/\mu_0$ , where  $\mu_0$  is the vacuum permeability. It has a value of  $4\pi \cdot 10^{-7} \text{ N/A}^2$  in the SI system of units.

coverage is called occupation factor  $\varepsilon^2$ . We measure the occupation factor for every image from all the experiments for each set  $(\omega, H, r)$ , where  $r$  is the distance to the center of spinning. It is equivalent to the dimensionless thickness of a multilayer deposit and the spatially averaged values are further used for obtaining the magnetic field dependent relative viscosity of the used mixed particles suspension.

### Identifying the distribution of carbonyl iron particles from the dried deposits

Two different techniques are used to distinguish the distribution of carbonyl iron particles from the dried deposits that include: photo-spectrophotometer (for the experiments of  $2 \mu\text{m}$  carbonyl iron particles) and thermal camera (for the experiments of  $3 \mu\text{m}$  carbonyl iron particles).

To differentiate the carbonyl iron particles deposit, we place the substrates with dried deposits (mixed particles) into the oven kept at  $250^\circ\text{C}$  for overnight. The carbonyl iron particles become oxidized and change the colour (from black to blue). Then, the spectrophotometer (CM-2500d, SpectraMagic.NX) is used to obtain colour reflection spectrum of the central part (8 mm) substrate with maximum deposits.

Also, the typical micrographs of the dried deposits of the mixed particles are captured with thermal camera (Xenics: Gobi-384-Premium 50Hz-PAL Scientific). Fig. 6.6 shows a micrograph captured with thermal camera from an experiment performed at  $60.7 \text{ mT}$ ,  $2000 \text{ rpm}$ . Everything is at same temperature where carbonyl iron deposit is bright. We characterize the amount of deposit by measuring “occupation factor” or surface coverage  $\varepsilon^2$  for each micrograph.

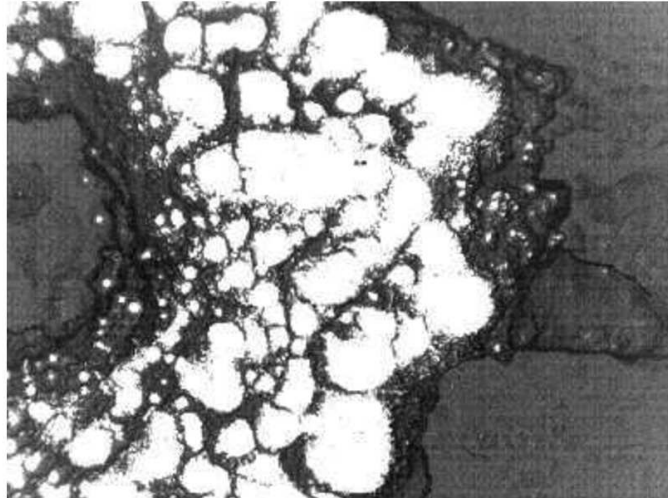


Figure 6.6: Micrography of spin-coated substrate captured with thermal camera (everything at same temperature so, we can distinguish different emissivities / reflectivities, where iron is bright. Spinning rate is  $2000 \text{ rpm}$  and the magnetic field is  $0.060 \text{ T}$ . The field of view is  $8.4 \text{ mm}$ .

## 6.2. Spin-coating of colloids on photo-patterned substrate

In this section, we set up experiments of spin-coating for characterizing out-of-equilibrium approaches to fabricate polycrystals of monolayer of micro-sized silica colloidal particles, by de-

veloping a patterning technique to create hydrophobic and hydrophilic substrates. The main objective is to demonstrate the effect of the surface treatment on the obtained colloidal structures. The experiments have been performed in collaboration with soft matter physics group of Memorial University of Newfoundland, Canada under the supervision of Dr. A. Yethiraj.

### 6.2.1. Surface treatment and hydrophilic substrates

We design masks of different geometries (circles or hexagonal pillars) of different size using Inkscape. Patterns of hexagonal pillars of 1.1 mm diagonal with various spacings in between them (0.3, 0.55, 0.82 and 1.09 mm) are designed to fabricate photo-patterned substrates for our experiments. To do so, SU-8 2010 (UV-sensitive photoresist, obtained from MicroChem Corp, USA) is spin-coated on the microscope cover slip (of size  $22 \times 30 \text{ mm}^2$ ) at 3000 rpm for 30 seconds to achieve the thickness of  $10 \mu\text{m}$ . After, it is soft-baked at  $95^\circ\text{C}$  for 3 minutes and exposed to UV-light through MPS (Micro Patterning Surfaces) technique with previously designed pattern for 3–4 minutes. Later on, cover slip is hard baked at  $95^\circ\text{C}$  for 3 minutes for postexposure bake. Later, it is developed for 2 minutes with ethyl-lactate and 5% NaOH solution. This photolithography step enhanced the hydrophilic character of the surface of the substrate. The cover-slip is glued after patterning over the commercially available microscope glass slides for further use in our experiments.

### 6.2.2. Suspension

Silica particles of diameter  $0.5 \mu\text{m}$  obtained in dried form from AngstomspHERE<sup>TM</sup> (commercially available in Fiber Optic Center inc.) are dried overnight at  $150^\circ\text{C}$  inside the oven to reduce the absorbed moisture. After, they are taken out of the oven and kept for some time to reach at room temperature then the desired volume of the volatile solvent (ethanol 95%) is added to the weighted particles to prepare a suspension of 20% (v/v) concentration. Later, it is ultrasonicated for several hours (approximately four hours) to obtain homogeneously dispersed suspensions.

### 6.2.3. Experiments

All experiments are carried out in air environment at room temperature with a standard spin-coater (Laurell technologies, WS-650SZ-6NPP/LITE/OND), keeping inside a fume hood for protection from the vapors of the solvents. The photo-patterned substrate is spun at 3000 rpm.  $60 \mu\text{l}$  suspension is pipetted, when the substrate reaches a constant angular velocity. After the spun when the dispersion is completely dried, the spinning is stopped.

### 6.2.4. Characterization of spin-coated deposit

The spin-coated deposit on the SU-8 pillar of patterned substrate is characterized by Atomic Force Microscopy (AFM, Asylum Research MFP-3D<sup>TM</sup>). Prior to scan with AFM, the colloidal film is spin-coated with a thin layer ( $\approx 100 \text{ nm}$ ) of polymer (PMMA) to prevent the surface being scratched by the AFM tip. AFM is operated in contact mode. The tip is lowered till it touches the top surface of the colloidal film (Fig. 6.7). After, the parameters of the AFM are adjusted, the system measures the deflection of the tip as it scans and captures the topography of the structure. We scanned and captured regions of  $20 \times 20 \mu\text{m}^2$ , at  $2.24 \text{ mm}$  intervals in such a manner that



Figure 6.7: Optical image of the AFM tip (red square) at the moment of scanning the top structure of the colloidal thin film sample.

each scanned region makes an angle of  $\beta = \arctan(1/2) = 26.6^\circ$  with radial direction away from the center of rotation (see Fig. 6.8). A zero order flattening is applied to compensate internal systematic error of the system. A sample scan by AFM is shown in Fig. 6.9. The microscopic

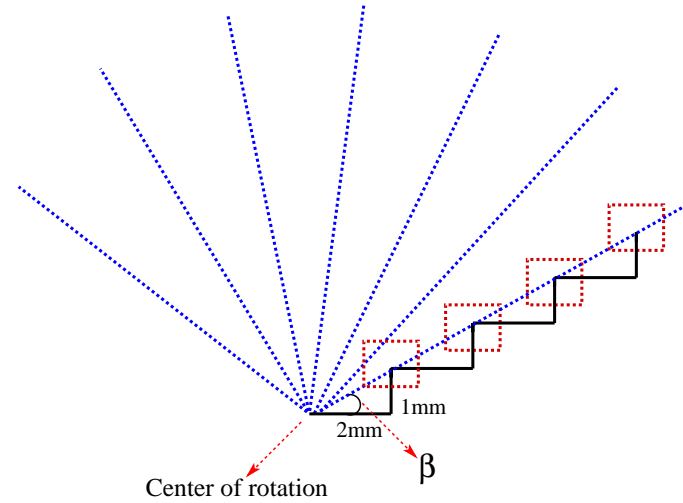


Figure 6.8: Scanning regions (red dotted squares) by AFM, at 2.24 mm intervals (such that the 1st distance (2,1)=2.24 mm), where every scanned region makes an angle of  $\beta = \arctan(1/2)$  with radial direction (rightmost blue dotted lines) away from the center of rotation.

structure of the top surface of these deposits observed via AFM presents colloidal polycrystals (Fig. 6.9). Preliminary results on image processing of AFM images that have been characterized in terms of symmetry, orientation, domain size and the ratio of hexagonal to square packing of particles in polycrystals of monolayers are explained in [3, 115]. The dried films are also imaged

by optical microscope using objectives of various magnifications (4X, 10X, 20X, 40X), as shown in Fig. 6.10.

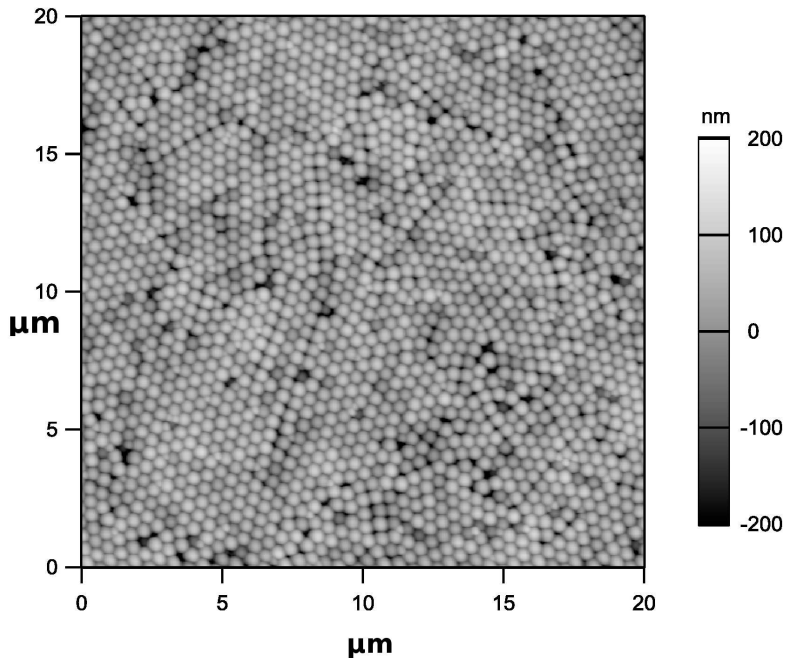


Figure 6.9: Sample of AFM scanned image of the top surface of colloidal deposits on SU-8 pillar of the patterned substrate, showing mostly hexagonal packing.

### 6.2.5. Surface treatment and hydrophobic substrates

We design masks with circles of size  $\approx 1.1$  mm arranged in hexagonal shape, using Inkscape. Microscope cover slip (of size  $22 \times 30$  mm $^2$ ) are cleaned using a common glass cleaning procedure: keep in NaOH (0.5%) solution for 24 hours, sonicate in water for 10 minutes, transfer to sulfuric acid for 15 minutes, sonicate in water for 10 minutes and rinse with ethanol (95%), then dry with filtered air before the photo-coating step. A thin layer of S-1813<sup>TM</sup>G2 positive photoresist is spin-coated onto the freshly cleaned cover slip at 4000 rpm for one minute using commercial spin coater. Next, it is soft baked at 100 °C for one minute and exposed to UV-light through MPS (Micro Patterning Surfaces) technique with previously designed pattern for 3–4 minutes. The unmasked area due to the UV exposure becomes acidic. 0.5% (w/w) NaOH solution is used as a developer where the exposed substrate is immersed in it for thirty seconds. After, it is rinsed with ultra pure water and dried with filtered air.

#### Silanization

Silanization of the photo-patterned cover-slip is performed by dip coating that produce roughly silane monolayer coverage on the glass surface, where aminosilanization converts the glass surface

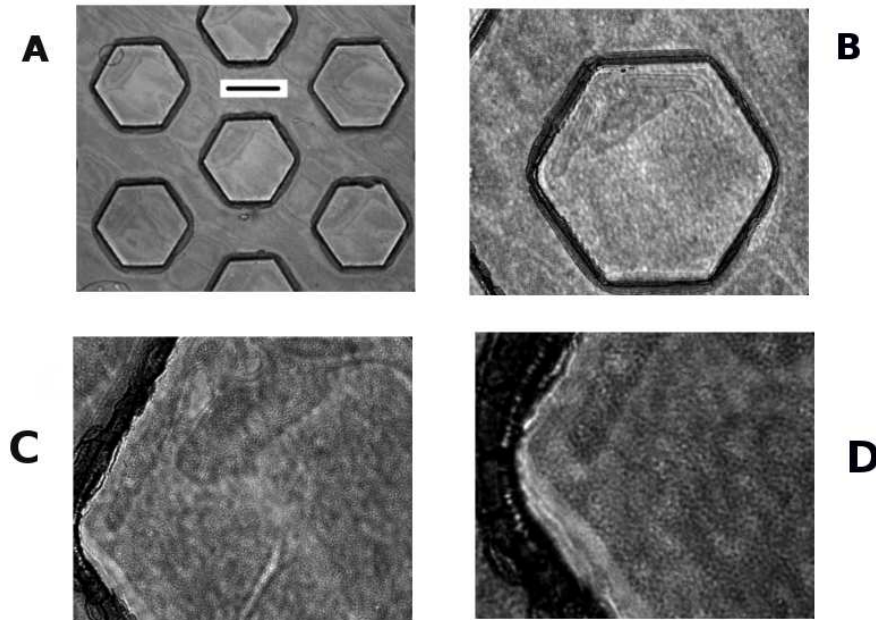


Figure 6.10: A–D are images of the top surface of colloidal thin film by optical microscope from the experiment where the spacing between hexagonal pillars is 0.82 mm using objectives of various magnification 4X, 10X, 20X and 40X respectively. Scale bar in image A is 0.62 mm

from negative to positive potentials [116]. The cover slip is immersed in aqueous solution of silane (composed of 5% of octadecyltrichlorosilane (OTS) and 95% of hexane) for 15 minutes. After it is shacked in ethanol (95%) for 5 minutes, rinsed with ultra pure water and dried with filtered air. Finally, the layer of S-1813<sup>TM</sup>G2 on the part of the cover slip is removed by rinsing it intensively with acetone. Later, it is rinsed with water and dried well. The silanization step enhanced the hydrophobic character of the surface of the substrate. After we glue the patterned-silanized cover slip over the microscopic glass to use for spin-coating experiments. The experiments are performed following the same procedure explained in section 6.2.3.

## Chapter 7

# Results and Discussions

Firstly, in this chapter we presents the experimental results on magnetorheology of mixed colloids measured by spin-coating. A magnetic field is applied during the spin-coating of the colloidal suspension involving evaporation of the solvent. We show the results obtained at different experimental conditions: for the range of the rotation rates of the substrate (2000 to 7000 rpm) and changing magnetic field (0.05 to 72.7 mT). The magnetic field-dependent relative viscosity of hybrid diluted colloids of carbonyl iron+silica in cyclohexanone using spin-coating is derived from the surface coverage of the spin-coated deposit. The resulted occupation factor from dried colloidal film is introduced in the modified Cregan model to extract magnetoviscosity. The results under different experimental conditions and the effect of different component on the magnetorheological characteristics of the spin-coated colloid deposit will be discussed in detailed in the following section. Secondly, here we show experimental results on fabricating the colloidal polycrystals of monolayer by spin-coating (using nonmagnetic colloids), without the appearance of colors arms by axial symmetry, using photo-patterned substrates.

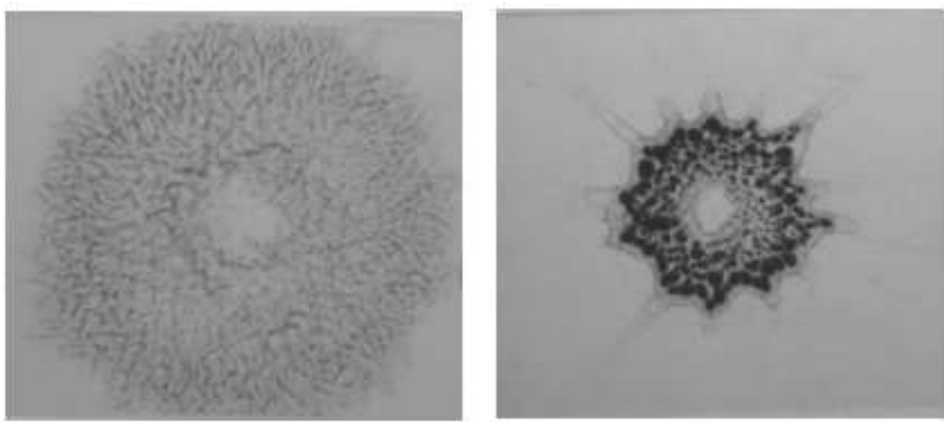


Figure 7.1: Images of different spin-coated colloidal deposits (carbonyl iron +  $\text{SiO}_2$ ) on the whole substrate, captured with a black and white camera at very low magnification and transmission. Spinning rate for both images is 2000 rpm. The magnetic field for the image on left side is 0.037 T and for the right side is 0.061 T. The field of view for both images is 12 mm.

## 7.1. Magnetorheology of hybrid colloids by spin-coating

### Spin-coating of hybrid colloids in magnetic fields

Hybrid colloids are prepared by dispersing magnetizable carbonyl iron particles in a non-magnetizable liquid cyclohexanone. We use carbonyl iron particles due to their large saturation magnetization [110]. In addition, silica particles of similar size (in order of magnitude) are added to this suspension (section 6.1.1) to reduce the settling of particles [117]. Magnetic field-induced magnetization of the suspended carbonyl iron particles is referred as the magnetorheological effect. On applying a magnetic field, the magnetoviscosity of the suspension increases and magnetic particles attract each other through their magnetic dipoles [118]. As a consequence, clusters or elongated chains of particles are formed depending on the field strength and spinning rate. At our spin-coating experimental conditions in magnetic fields (see chapter 6), we obtain colloidal dried deposits consisting of larger clusters of particles. Fig. 7.1 shows the whole spin coated dried deposit on the substrate at very low magnification and transmission using a black and white camera. These deposits are obtained at the same spinning rate 2000 rpm but at different magnetic fields (increasing from left to right). The experiments are performed with and without magnetic field. Small groups of particles are observed without magnetic fields (see Fig. 7.2-A, C, E) while deposit of larger size clusters are obtained under magnetic fields (see Fig. 7.2-B, D, F). The average area of deposit depends on the spinning velocity  $\omega$ , the magnetic field strength  $H$  and  $r$  which is the radial distance from the center of spinning. This area decreases for an increase in the rotation rate or if we move away from the spinning center on the dried substrate or in the case, if the applied magnetic field is reduced (see Fig. 7.2).

### The occupation factor

The deposited amount of colloidal particles by spin-coating is characterized by introducing surface coverage or the occupation factor ( $\varepsilon^2$ ), which is defined as the deposited area occupied by the clusters relative to the total area of the observation. To measure the occupation factor  $\varepsilon^2$  images of each spin-coated substrate are captured at 2 mm increasing regular intervals from the center of rotation ( $r$ ) with 10X microscopic objective, then they are analyzed through homemade routines in Octave [57] (see section 6.1.4 for details). In this case, if we assume axial symmetry the occupation factor values for each sample (spin-coated substrate) are measured along  $r$  (in 1-d) i.e.  $\varepsilon^2(r)$ . We also calculate its average values over  $\vec{r}$  i.e.  $\langle \varepsilon^2(\vec{r}) \rangle$  (in 2-d). The relationship between  $\langle \varepsilon^2(\vec{r}) \rangle$  and  $\varepsilon^2(r)$  (see sketch in Fig. 7.3) is given as

$$\langle \varepsilon^2(\vec{r}) \rangle_{area} = \frac{\langle r \cdot \varepsilon^2(r, 0) \rangle_r}{\langle r \rangle_r} \quad (7.1)$$

Fig. 7.4 presents the occupation factor as a function of increasing radial distance from the spinning center  $r$  (in 1-d) at 3000 rpm spinning at various magnetic fields. This plot shows that  $\varepsilon^2(r)$  as a measure of the colloidal films thickness is not homogeneous along  $r$  from the center of rotation as previously has been observed [102]. We measured its average value for each sample over  $\vec{r}$  / area at fixed  $\theta$  using eq. 7.1 which is used for further analysis. In Fig. 7.5 we observe an increase in the average occupation factor on increasing applied magnetic field that may be caused

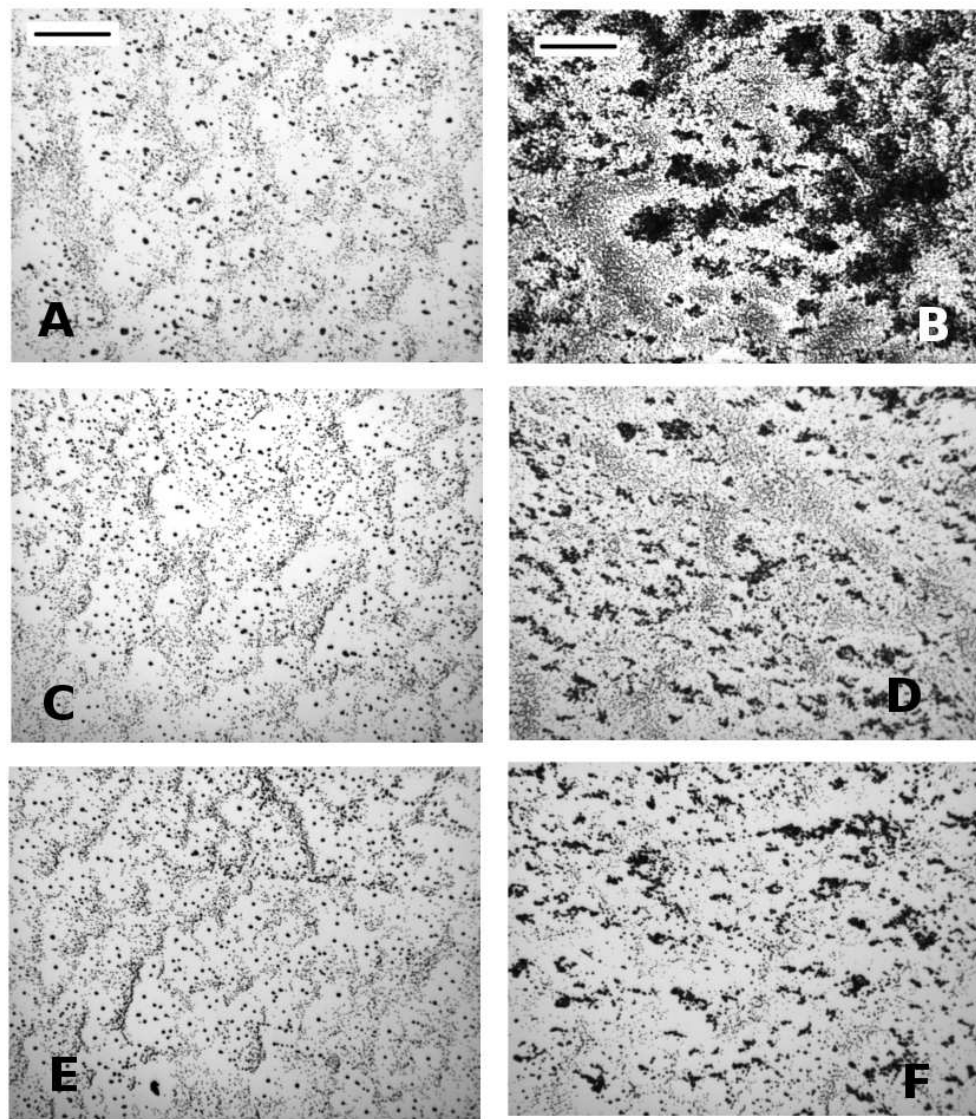


Figure 7.2: Images of the different spin-coated dried deposits ( $\text{SiO}_2$  and carbonyl iron particles suspension) at 6 mm from the center of rotation by 10X microscopic objective. For A, C and E, the magnetic field  $B = 0.05 \text{ mT}$  and for B, D and F, the applied magnetic field is  $H = 0.036 \text{ T}$ . The rotation rate is 3000 rpm for A and B; 5000 rpm for C and D; 7000 rpm for E and F. When the magnetic field is applied, the carbonyl iron particles accumulate to form clusters (B, D and F). The diameter of the carbonyl iron particle is  $2 \mu\text{m}$  (scale bar is  $100 \mu\text{m}$ ).

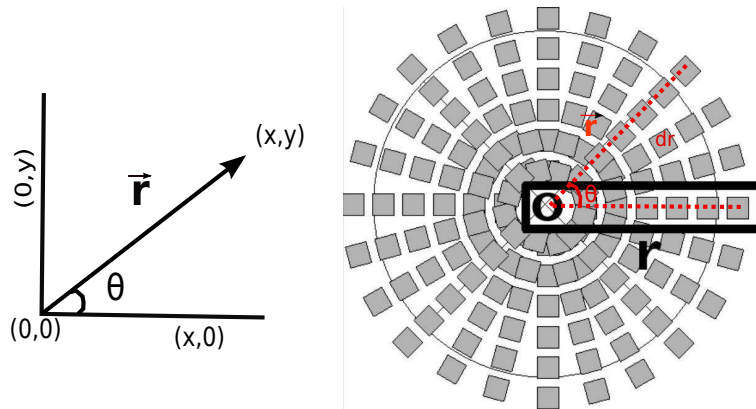


Figure 7.3: Schematic representation for measuring  $\varepsilon^2(r)$  (in 1-d along  $r$ ) and obtaining  $\langle \varepsilon^2(\vec{r}) \rangle$  (in 2-d). Left: shows the axis system and notation used with the center of spinning at (0,0). Right: shows the sketch with images of spin-coated substrates captured at  $r=d_r=2$  mm increasing regular intervals from the center of rotation ( $r=0$ ), which is integrated to obtain a 2-d distribution ( $\vec{r}$  (over area)).

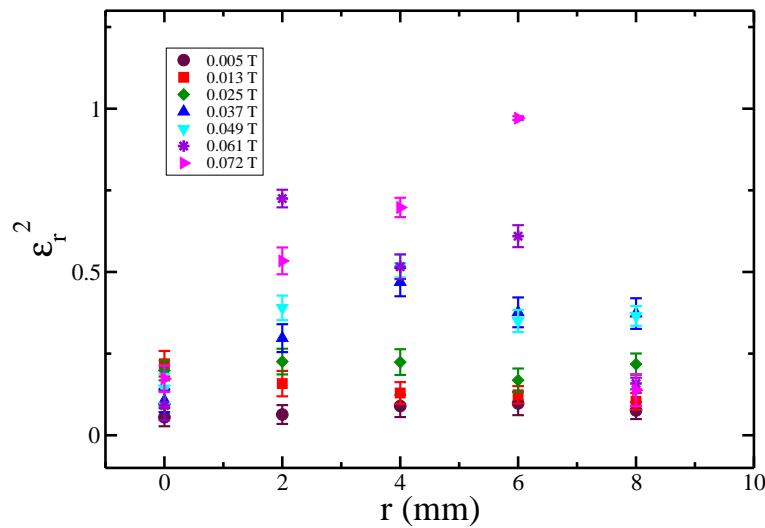


Figure 7.4: The occupation factor as a function of increasing distances along  $r$  (1-d) from the center of rotation. The spinning rate is 3000 rpm.

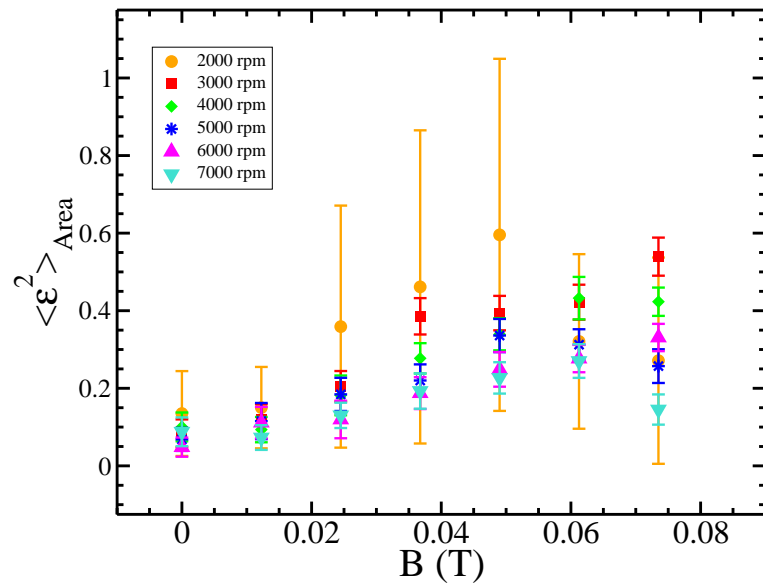


Figure 7.5: The average occupation factor and its standard deviation as a function of increasing applied magnetic field for colloidal deposit of carbonyl iron+silica dispersion. The average occupation factor is calculated for the whole sample over area ( $\vec{r}$ ). Larger error bars could be due to the large non-Newtonian character of the hybrid colloids at higher magnetic field.

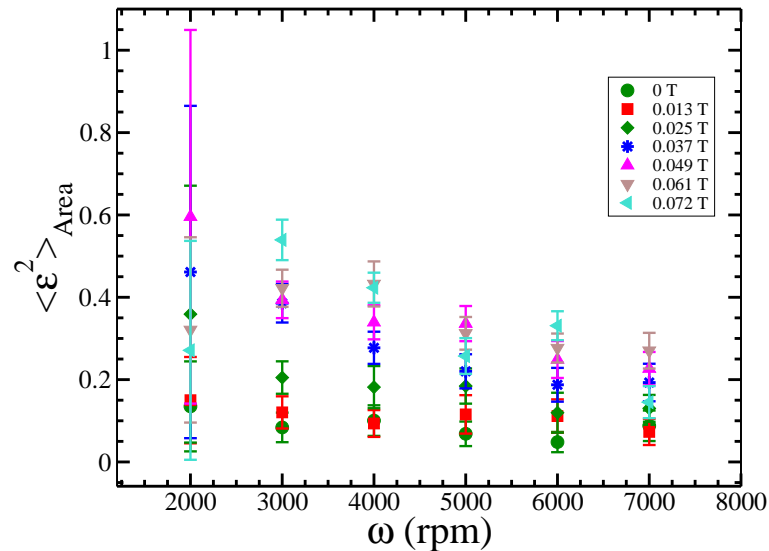


Figure 7.6: The average occupation factor (in 2-d) as a function increasing spinning velocity at various applied magnetic fields.

by an increase in the effective viscosity [119] shown in Fig. 7.1. Meanwhile, Fig. 7.6 shows that the occupation factor is decreasing on increasing the rotation rate at different applied magnetic fields.

### 7.1.1. Simple model for magnetorheology of colloids by spin-coating

Fluid dynamics on the spinning disk has been investigated since long from the perspective of thinning Newtonian fluid layers (e.g. Emslie *et al.*, Meyerhofer *et al.*, Cregan *et al.*) [74, 75, 77, 85].

#### Colloidal film thickness

The standard idea of these continuum models could be extended to understand colloidal dispersion dynamics from spin-coated deposits. A simple model for colloidal spin-coating has been introduced by modifying the existing Cregan model [95] (eq. 7.2).

$$h_{\infty}^{(s)} = \frac{C}{1-C} \left( \frac{3}{2} \nu E \right)^{\frac{1}{3}} \omega^{-\frac{2}{3}} = A \omega^{-\beta} \quad (7.2)$$

where  $h_{\infty}^{(s)}$  is the final deposited film thickness,  $C$  is the initial concentration in v/v,  $\omega$  is the rotation rate and  $\nu$  is the kinematic viscosity of solvent,  $E$  is evaporation rate of solvent.  $A$  is a constant over the experiment and  $\beta = \frac{2}{3}$ . Cregan *et al.* [85] model proposed a constant evaporation rate  $E$  which does not depend on the rotation rate  $\omega$ . Nevertheless, in other models [38, 75], it is defined as  $E \propto \omega^{\frac{1}{2}}$  or  $E \propto \omega$  respectively. Giuliani *et al.* [102] model proposed that the evaporation rate depends on the rotation rate, the parameters of the suspension and experiment in a particulate system (e.g. colloidal system). By inverting eq. 7.2 we can obtain  $E(\omega)$  at different conditions

$$E(\omega) = \left[ \frac{1-C}{C} h_{\infty}^{(s)} \right]^3 \frac{2\omega^2}{3\nu} \quad (7.3)$$

For spin-coating of our colloidal system, we consider a set of assumptions including that the solvent is volatile enough and  $h_{\infty}^{(s)}$  is the compact equivalent height (CEH) depending on the geometry of deposited structure [95]. For 2-d hexagonal submonolayer deposited structure (diluted suspension) is obtained as

$$h_{\infty}^{(s)} = \frac{2\pi}{3\sqrt{3}} R \cdot \varepsilon^2 \quad (7.4)$$

where  $R$  is the radius of the colloidal particles. The coefficient to  $\varepsilon^2$  comes from geometric considerations. In principle, we have access to all parameters if the  $\nu$  of the solvent and the radius of the particles are known, and the occupation factor is measured. Thus from eq. 7.3, it is possible to obtain the evaporation rate as a function of the spinning rate.

Pichumanli *et al.* [95] have generalized eq. 7.2 by including an evaporation rate that may depend on  $\omega$ , but not on the magnetic field. Hence, if we compare two experiments performed in the same conditions, except for the applied magnetic field (both experiments lead to submonolayers), by computing the ratio of their corresponding compact equivalent heights (CEH) we obtain

$$\frac{h_{\infty}^{(s)}(H, \omega)}{h_{\infty}^{(s)}(H=0, \omega)} = \frac{\varepsilon^2(H, \omega)}{\varepsilon^2(H=0, \omega)} \quad (7.5)$$

Substituting the left hand side of eq. 7.5 by eq. 7.2, the corresponding generalized Cregan equation, the kinematic viscosity  $\nu$  is the only parameter which remains dependent on the field. This gives

$$\frac{\nu(H, \omega)}{\nu(H = 0, \omega)} = \left[ \frac{\varepsilon^2(H, \omega)}{\varepsilon^2(H = 0, \omega)} \right]^3 \quad (7.6)$$

### 7.1.2. Model for the magnetorheology of mixture or hybrid colloids

In this work we have colloidal suspensions which contain more than one kind of particles, in this case it is possible to generalize the Cregan's equation by taking into account that both kind of particles have a size within the same order of magnitude and we consider that the equivalent spin-coated deposit behaves equally to that of a non-particulate system (i.e. eq. 7.3). In this case Eq. 7.4 can be rewritten as

$$h_\infty^{(s)} = \frac{\pi}{3\sqrt{3}} \sum_i (2R_i) \cdot \varepsilon_i^2 \quad (7.7)$$

where the subindex  $i$  is the type of particle.  $h_\infty^{(s)}$  is based on the geometry of the deposited structure and in eq. 7.7 it is assumed as the compact equivalent height (CEH) for 2-d hexagonal submonolayer deposits.

While eq. 7.5 for the mixture in this case corresponds to

$$\frac{h_\infty^{(s)}(H, \omega)}{h_\infty^{(s)}(H = 0, \omega)} = \frac{\text{CEH}(H, \omega)}{\text{CEH}(H = 0, \omega)} = \frac{\sum_i (2R_i) \cdot \varepsilon_i^2(H, \omega)}{\sum_i (2R_i) \cdot \varepsilon_i^2(H = 0, \omega)} \quad (7.8)$$

Using the compact equivalent height of the Cregan's model of the continuous system, we obtain the field dependent kinematic viscosity  $\nu$  for the mixture that leads to

$$\frac{\nu(H, \omega)}{\nu(H = 0, \omega)} = \left[ \frac{\text{CEH}(H, \omega)}{\text{CEH}(H = 0, \omega)} \right]^3 \quad (7.9)$$

#### The occupation factor for the mixture

As the occupation factor is approximately a conserved magnitude for the same order of magnitude sized particles, therefore for the mixture we have that

$$\varepsilon_{\text{total}}^2 \approx \sum_i \varepsilon_i^2 \quad (7.10)$$

We obtain the total occupation factor  $\varepsilon_{\text{total}}^2$  from Fig. 7.2 (which is a sample, captured using 10X objectives and  $\varepsilon_{\text{total}}^2$  is the total deposited area (composed of carbonyl iron + SiO<sub>2</sub>) divided by the total substrate area). Fig. 7.7 is a sample, captured with a thermal camera, allows us to obtain the occupation factor for carbonyl iron particles  $\varepsilon_{\text{Fe}}^2$ , this is due to the fact, that we can distinguish the two kind of particles deposit on the basis of their emissivity values. For instance, iron is bright due to its smaller emissivity but much higher reflectivity. The occupation factor of silica can be easily obtained as  $\varepsilon_{\text{total}}^2 \approx \varepsilon_{\text{Fe}}^2 + \varepsilon_{\text{SiO}_2}^2$

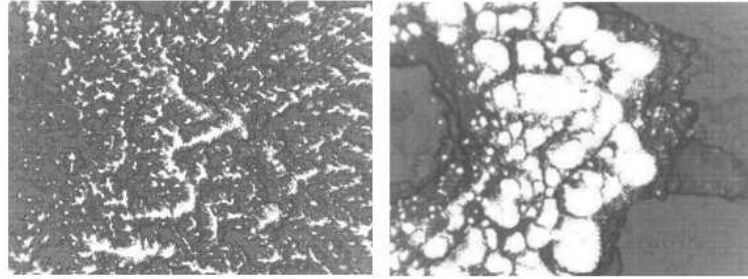


Figure 7.7: Micrographs of the spin-coated deposits (carbonyl iron +  $\text{SiO}_2$ ) at the same temperature, captured with thermal camera, we can distinguish the two kind of particles deposit where iron is bright. The spinning rate for both images is 2000 rpm. The magnetic field for the image on left side is 0.037 T and for the right side is 0.061 T. The field of view for both images is 8.4 mm.

### The compact equivalent height (CEH)

Introducing these raw measured values of the occupation factors in eqs. 7.7 and 7.10, we can obtain the compact equivalent height of the colloidal deposits at different magnetic fields and also without field as shown in Fig. 7.8. The CEH thickness in this case, without magnetic field (black circles in Fig. 7.8) in comparison with the spatial averaged final film thickness of  $\text{SiO}_2\text{-NM}$  which was measured by Atomic Force Microscopy (blue circles in Fig. 7.8, where  $\text{SiO}_2\text{-NM}$ ; silica nonmagnetic particles of diameter 458 nm were dispersed in MEK and information is extracted from Fig.4a of the reference experiment reported in [102]. It is outstanding that although the particles and the solvents of both experiments have different values for their physical and chemical properties, data follow the same power law. Therefore, it appears that Cregan's generalized model holds for zero-field (dotted lines in Fig. 7.8 correspond to the model proposed by Cregan *et al.* [85]). This thickness ( $h_{scaled}$ ) from the reference experiment corresponds to a multilayer because they used a concentrated suspension. Fig. 7.8 shows a common curve fitting for both experiments such that the film thickness decreases as the spinning rate increases.

CEH for the magnetic colloids increases on increasing the applied magnetic field, it is represented with squares (at  $H = 29.2 \text{ kA/m}$ ) and diamonds (at  $H = 48.7.2 \text{ kA/m}$ ) in Fig. 7.8. These results represent an increase of the average occupation factor on applying a magnetic field as shown in Fig. 7.5. Here, we have also observed, the decreasing tendency of the CEH depends on the rotation speed due to decrease in the average occupation factor values for increasing  $\omega$  as it can be observed in Fig. 7.6.

### The magnetoviscosity

Using eqs. 7.9 and 7.10, that the relative change in viscosity due to the applied magnetic field is measured. The values for  $\varepsilon_{total}^2$  are obtained from the experimental data. For a given magnetic field (48.7 kA/m), we plot in Fig. 7.9 the relative change in viscosity for all  $\omega$ . There, we can observe a very high effective magnetoviscosity for low shear rates (frequencies of rotation). In those cases, there is a phase separation, producing a faster evaporation and a much more compact deposition (e.g. Fig. 7.7right). Next, by averaging over  $\omega$  for Fig. 7.9 (and equivalent for other fields), we obtain Fig. 7.10. The average relative viscosity increases with increasing magnetic

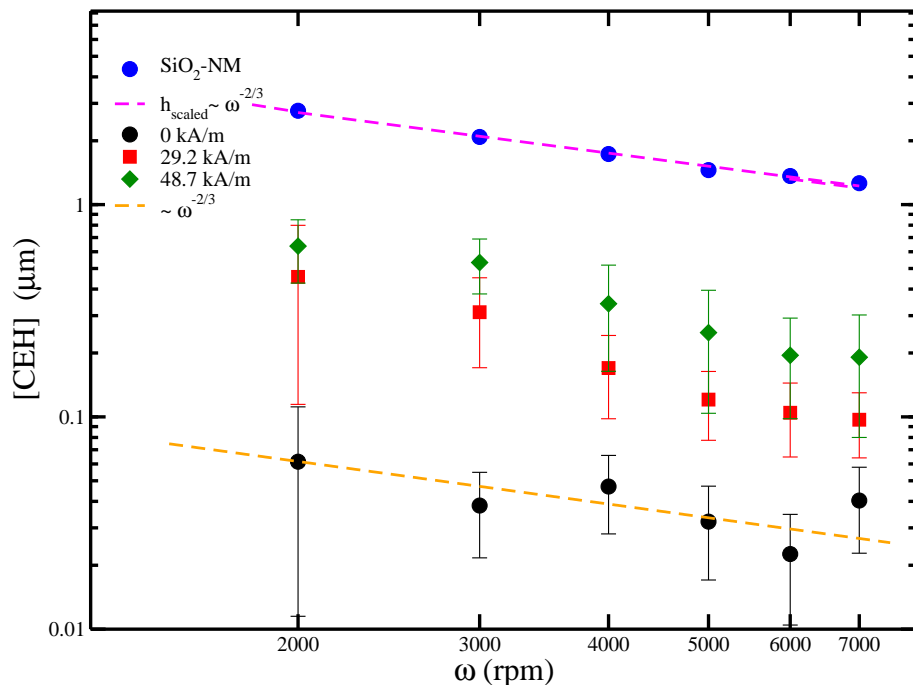


Figure 7.8: Compact equivalent height (CEH) and its comparison with the film thickness for different colloids without and with applied magnetic field. For the mixture of SiO<sub>2</sub> and carbonyl iron: black circles at H= 0 kA/m; square at H= 29.2 kA/m; diamonds at H= 48.7.2 kA/m. Blue circles: represents the SiO<sub>2</sub>-NM, whose data have been extracted from Fig. 4a of the reference experiment reported in [102] by doing a spatial average over area. Dashed lines indicate the Cregan's model.

fields. This increase in the average relative viscosity due to magnetic field could be explained by considering the magnetic dipole interactions between the magnetic particles (carbonyl iron in this case). This transition from sparse (without field) to submonolayer deposits (with magnetic field) can be observed in Fig. 7.2. Large error bars in Fig. 7.10 could be due to the large non-Newtonian character of the colloids under higher magnetic field [98, 120, 121].

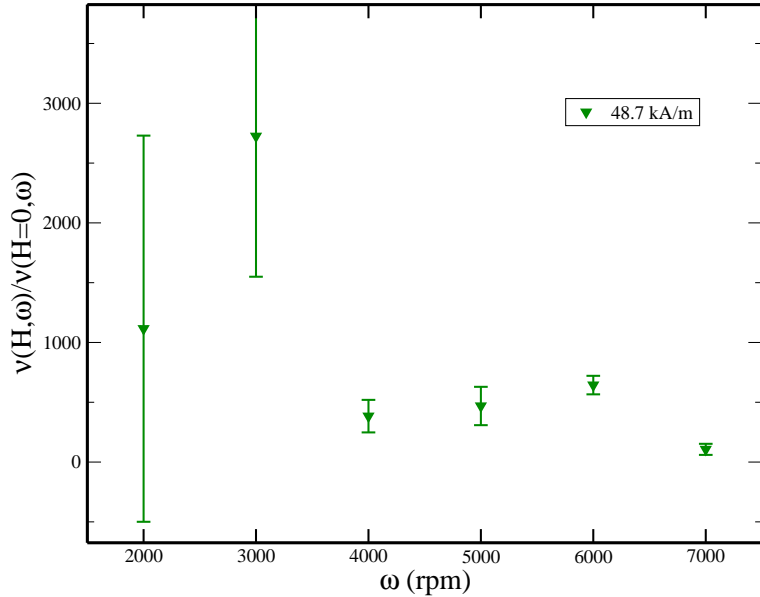


Figure 7.9: The effective magnetoviscosity at magnetic field of 48.7 kA/m as a function of the spinning velocity  $\omega$ .

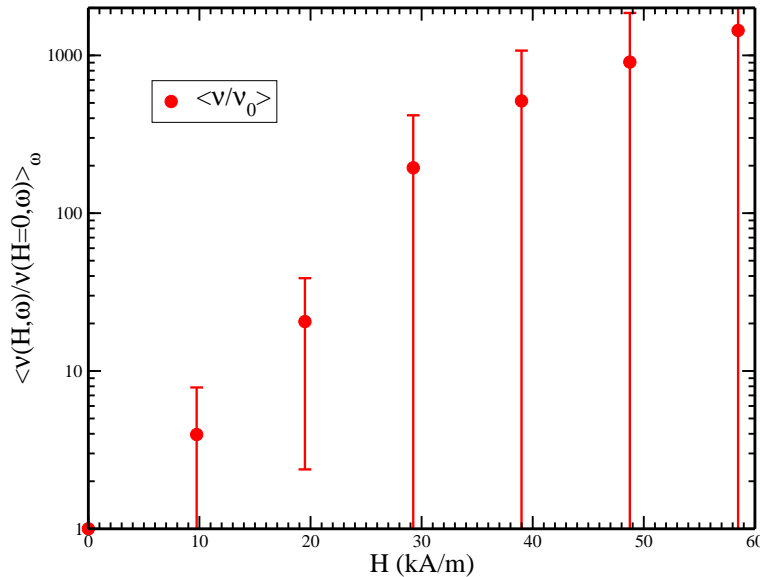


Figure 7.10: The relative change of the average normalized viscosity as a function of the applied magnetic field. This data is obtained by calculating the average over all  $\omega$ . The error bars correspond to 95% of confidence interval.

We compare our experimental results of magnetoviscosity from the surface coverage of spin-coated deposit with the results obtained from classical magnetorheometry [110] using a suspension of same mixture of particles ( $\text{SiO}_2$  and carbonyl iron) in collaboration with Dr. Juan de Vicente. The manuscript based on those results is submitted to Smart Mater. Struct. and will be published soon. Further work is in progress to investigate the effect of other factors on the magnetorheological characteristics of the spin-coated colloidal deposit such as the increasing concentration of suspensions.

## 7.2. Spin-coating of colloids on a photo-patterned substrate

Spin-coating is a simple, fast, cheap and reproducible method to fabricate colloidal crystals [2, 76, 86, 97, 103]. This technique produces fourfold, sixfold or mixed symmetries due to the axial symmetry imposed by the spinning axis for suspensions at higher concentrations of 40% w/w which is presented in the Fig. 7.11 (reprinted from [2]). In [2], they observed the emergence of symmetric radial colored arms in spin-coated colloidal crystals when the sample was illuminated with diffuse white light causing orientationally correlated polycrystals (OCP) referred to as polycrystallinity.

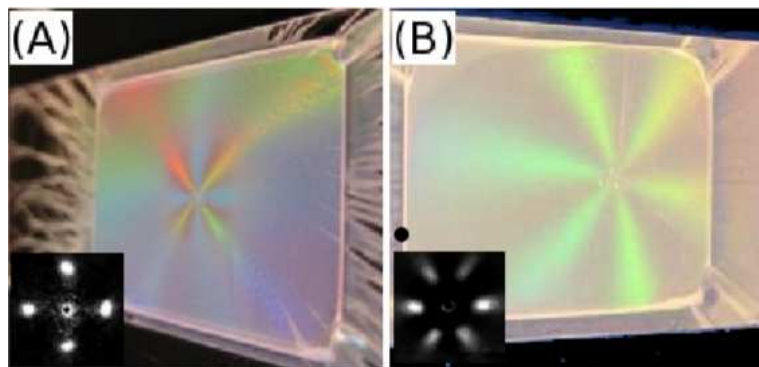


Figure 7.11: White-light reflections of colloidal spin-coated film at 3000 rpm from (A) acetone and (B) ethanol solvents on cover-slides display fourfold and sixfold symmetry. Laser diffraction patterns show that the 4-fold and 6-fold symmetries correspond to fcc structures [95] (image reprinted from [2]).

Producing close packed monolayer defect-free colloidal crystals has special interest to fabricate cheap photonic band gap materials [122–124]. Nowadays, the OCP character of colloidal-films by spin-coating is still a great challenge. Electric fields have been applied to break the axial symmetry and to produce translational ordered structures in [105, 125]. However, the application of these external fields leads the system towards more complex patterns and reducing the reproducibility of spin-coating.

In this work, we introduce a simple technique to produce colloidal polycrystals of monolayer by spin-coating without axial symmetry using photo-patterned substrates. In section 6.2, the experimental conditions to make colloidal thin films on photo-patterned substrates by spin-coating is explained in detail. As a brief remark, firstly the patterned substrate is spun at the required spinning velocity then the suspension is pipetted. Secondly, the spinning is stopped after the

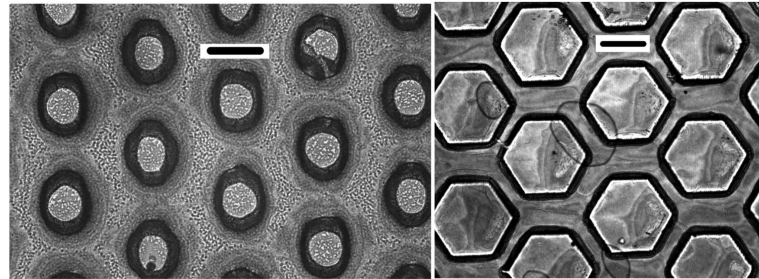


Figure 7.12: Microscopic images of colloidal spin-coated deposit at 3000 rpm on photo-patterned substrates with SU-8 on circle (left) and hexagonal (right) pillars. Deposits of silica particles of  $0.5 \mu\text{m}$  suspended in ethanol (solvent) on the patterned cover-slides do not show 4-fold and 6-fold symmetries on white-light reflections. Scale bar for both images is 0.6 mm.

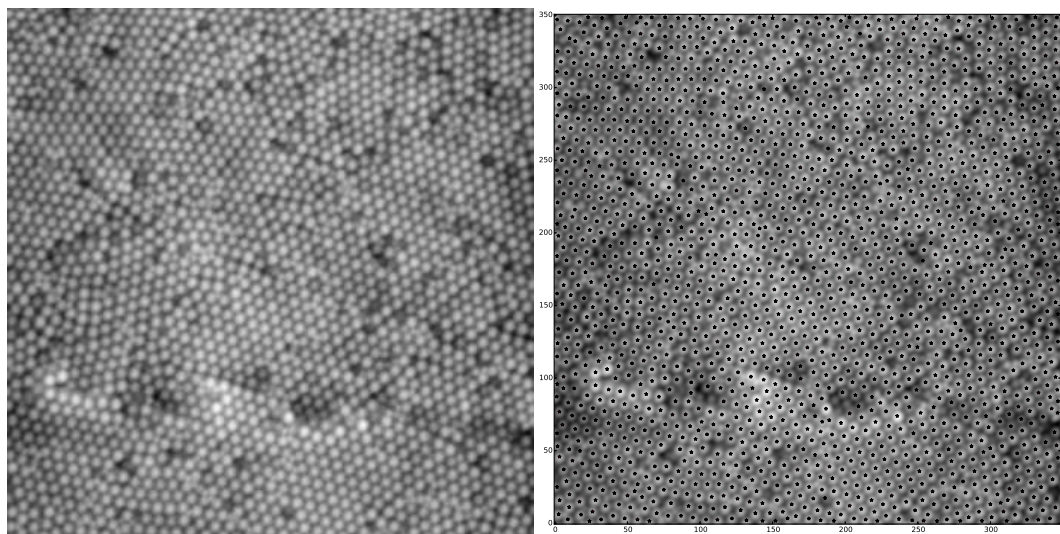


Figure 7.13: Real AFM image (field of view is  $20 \mu\text{m} \times 20 \mu\text{m}$ ) of a colloidal monolayer on the SU-8 pillar (left) and its particle detection analysis (right), where the center of particles have been marked.

dispersion is completely dried as it is shown in Fig. 7.12. Our experiments are in good agreement with hexagonal geometry for expected results and promote the formation of monolayer structures. Thus, hexagonal patterning geometry is kept for all experiments. In the following, we will examine the spin-coated films to identify the degree of structural order. The structures (AFM images) have been analyzed in depth with standard bond orientational order parameters [3] and with Minkowski structure metrics [4]. We also discuss the influence of the scaling spacing of the patterning on the structural order of colloidal films.

### 7.2.1. Structural analysis of spin-coated films

To quantify the degree of structural order of spin-coated films, images of colloidal deposit on SU-8 hexagonal pillar are captured with Atomic Force Microscopy (of large area  $20 \mu\text{m} \times 20 \mu\text{m}$ ) along the radial direction (see section 6.2.4 for details). First, in each AFM image the positional coordinates of the particles are obtained by using the home-made routines which are based on scikit-image processing [126]. These routines are used to detect the center of particles in AFM images (a sample shown in Fig. 7.13-left), the red stars indicated in Fig. 7.13-right. Then, they are analyzed with bond order parameters and with Minkowski structure metrics. Finally, we present a comparison of structural order in colloidal films based on two kinds of analyses.

#### 1) Local orientational bond order parameters

With the positional coordinates of the particles, we calculate the local orientational bond order parameter  $\psi_r(a)$  for a given weight  $r$  ( $r = 4$  or  $6$ ) which is assigned to particle  $a$ . Each  $\mathbf{n}_{ab}$  is the set of unit vectors pointing from particle  $a$  to the particle  $b$  where  $b \in NN(a)$  ( $NN(a)$  is the nearest neighbours of particle  $a$ ) and each  $\mathbf{n}_{ab}$  vector is characterized by bond orientation  $\theta_{ab}$  to a fixed reference axis.

Local orientational bond order parameters  $\psi_r(a)$  are defined as

$$\psi_r(a) = \frac{1}{NN(a)} \sum_{b \in NN(a)} e^{ir\theta_{ab}} \quad (7.11)$$

In eq. 7.11 the phase of  $\psi_r(a)$  determines the absolute orientation of  $NN(a)$  in  $r$ -fold orientation space. Its magnitude  $|\psi_r(a)|$  measures the deviation of perfect orientational structural order (hexagonal or square) having values between 0 and 1, where 1 marks perfect  $r$ -fold symmetry [3, 4]. The purpose of the bond orientation order quantification is to derive a scalar metrics from the information of the set of bond vectors. This method allow us to identify the degree of structural order, the microscopic distribution and orientation of particles of spin-coated colloidal films. We choose the values within the interval  $|\psi_r| = 0.5\text{--}0.6$  as the minimum threshold values for  $r$ -fold symmetry which are considered reasonable in our calculations towards better results. It is measured for each particle in AFM image for both 4-fold and 6-fold symmetries. For each AFM image, we measure the average values  $\langle \psi_r \rangle$  and  $\langle |\psi_r| \rangle$  in order to analyze the overall degree of order of configuration.

The phase of  $\psi_r$  is studied from histograms of the phase of two order parameters ( $\psi_6$  and  $\psi_4$ ) for each AFM image. A sample is shown in the Fig. 7.15-left, where each particle is assumed with  $\psi_6$  orientation for which  $|\psi_6| \geq 0.5$  and  $|\psi_4| \leq 0.6$  (green color) and with  $\psi_4$  phase for which  $|\psi_4| \geq 0.6$  and  $|\psi_6| \leq 0.5$  (red). Fig. 7.15-left (top-bottom) also indicates that in colloidal monolayer films

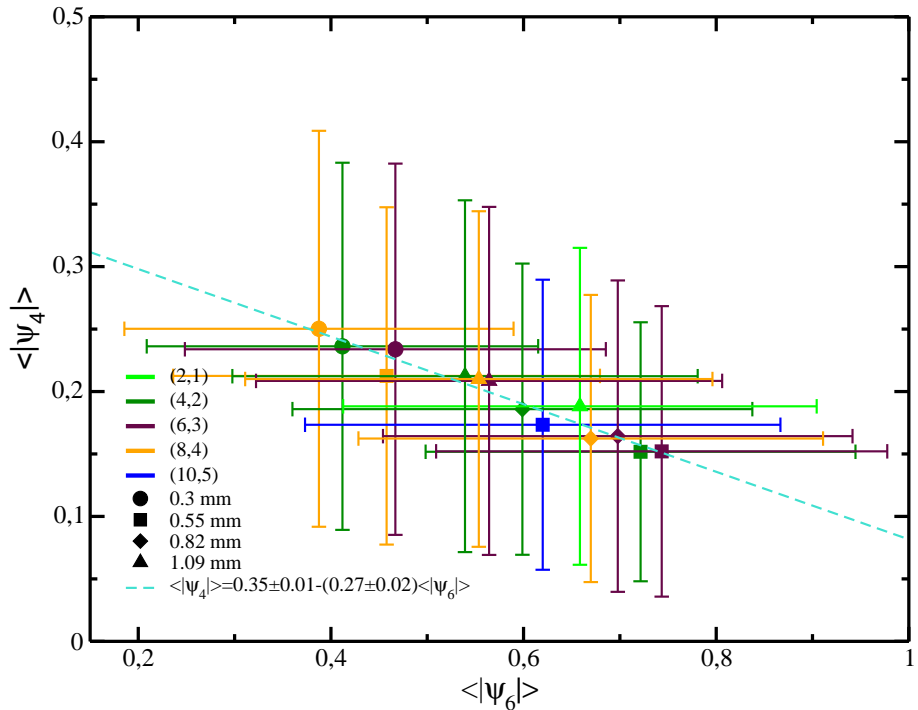


Figure 7.14: Average local bond order parameter for  $\langle |\psi_4| \rangle$  and  $\langle |\psi_6| \rangle$  of each AFM image of spin-coated deposit, taken along the radial direction at different increasing distances from the center of spinning evidenced by lines in legend (e.g. (2,1)=2.24 mm, see Fig. 6.8 for details), and as a function of increasing spacing between hexagonal pillars (see symbols in legend). For the scaling spacing of 0.55–0.82 mm we have greater values for  $\langle |\psi_6| \rangle$  and smaller for  $\langle |\psi_4| \rangle$ . The turquoise dashed line shows the regression analysis result.

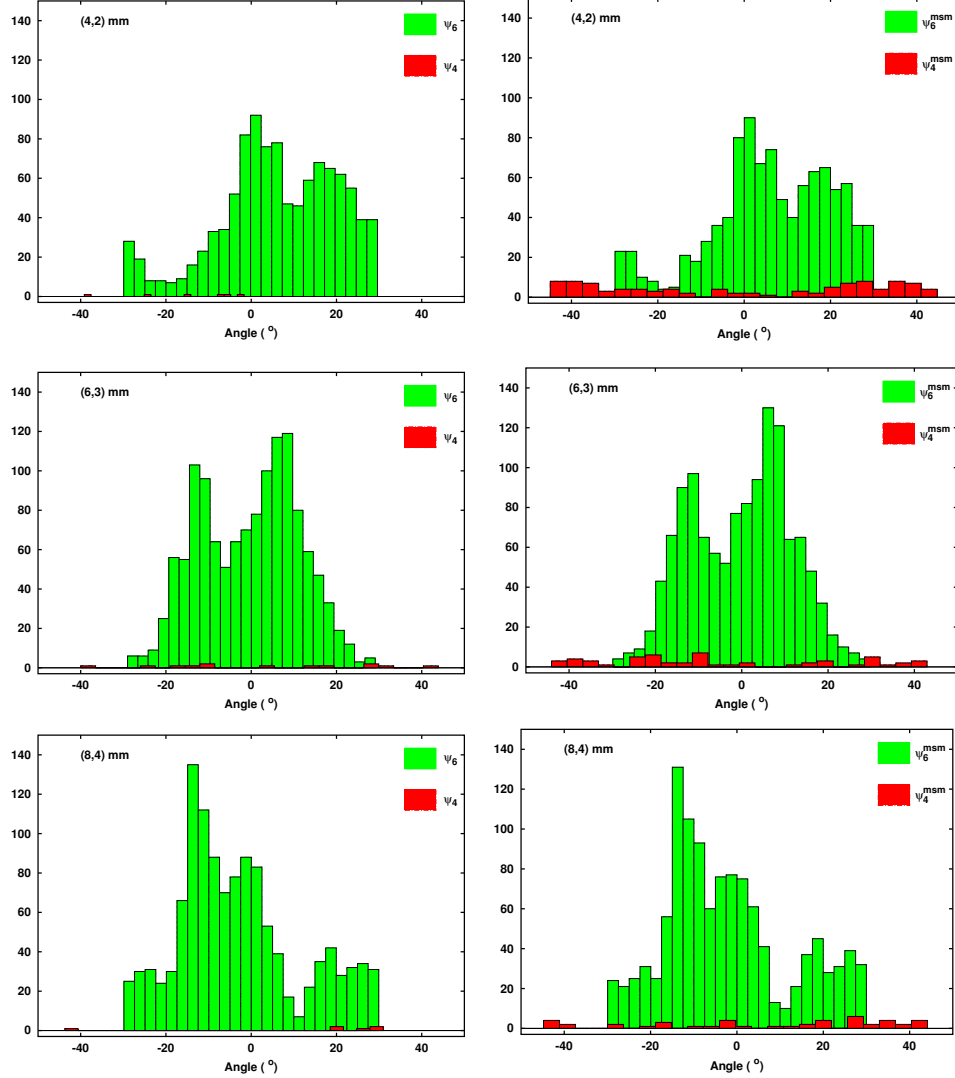


Figure 7.15: The histograms of phases  $\psi_6^{\text{msm}}$  and  $\psi_4^{\text{msm}}$  (right), and  $\psi_6$  and  $\psi_4$  (left) for each AFM image. Where green corresponds to 6-fold and red to 4-fold symmetries. Top-bottom images indicate histograms at increasing distances along the radial direction for the same experiment (whole substrate with the scaling spacing of 0.82 mm between hexagonal pillars).

produced by spin-coating on the SU–8 pillar of photo-patterned substrate, domains are not oriented along the radial direction from center of rotation in comparison with to polycrystals (OCP). Furthermore, Fig. 7.14 presents  $\langle|\psi_4|\rangle$  and  $\langle|\psi_6|\rangle$  values for different experiments from the AFM images. These results will be described in detail in the next sections.

## 2) The Minkowski structure metrics

Some fundamental difficulties were detected in the bond-orientational order parameters analysis that significantly affect their simplification to investigate the degree of order of disordered systems [4]. The bond-orientational order method assumes the geometrical arrangement of a set of nearest neighbors  $NN(a)$  around particle  $a$ ; where  $NN(a)$  has greater influence on  $\psi_r(a)$  values specifically in the case of square structure. Also, the discrete nature of  $NN(a)$  is not a continuous function of the particle coordinates which is responsible for the lack of robustness of the  $\psi_r$  as structure metrics. Consequently, Minkowski structure metrics (msm)  $\psi_r^{msm}$  is introduced to overcome these issues. The Minkowski structure metrics (msm) are achieved by modifying the conventional bond order parameters according to the reference [127]. Nevertheless, in msm the contribution of each nearest neighbor to the structure metric is defined by an associated relative length factor  $l(s)/L$ , where  $l(s)$  is the length between two neighboring vertices of the Voronoi cell of particle  $a$  that corresponds to a given bond  $s$ , and  $L = \sum_{s' \in \delta(a)} l(s')$  is the total perimeter length of the Voronoi cell of particle  $a$  as it can be seen in Fig. 7.16.  $\delta(a)$  is the set of bonds which link particle  $a$  with its nearest neighbors  $NN(a)$ . This simple modification could lead to robust, continuous and parameter-independent structure metrics  $\psi_r^{msm}(a)$  which avoids the flaws of the bond order parameters  $\psi_r$ . The Minkowski structure metrics  $\psi_r^{msm}(a)$  in 2-d is defined as

$$\psi_r^{msm}(a) = \sum_{s \in \delta(a)} \frac{l(s)}{\sum_{s' \in \delta(a)} l(s')} e^{ir\theta_{ab(s)}} \quad (7.12)$$

where  $\theta_{ab(s)}$  is the angle of the normal vector  $n_s$  of facet  $s$  (see Fig. 7.16) with fixed reference axis. From AFM images,  $\psi_r^{msm}$  and  $|\psi_r^{msm}|$  are measured for both 4-fold and 6-fold for each particle independently. For each AFM image, we then measure average values  $\langle\psi_r^{msm}\rangle$  and  $\langle|\psi_r^{msm}|\rangle$  to identify the overall degree of order of the structure. The phase of  $\psi_r^{msm}$  is presented with histograms of  $\psi_6^{msm}$  and  $\psi_4^{msm}$  for each AFM image. Fig. 7.15-right is a sample where green corresponds to  $\psi_6^{msm}$  phase and red to  $\psi_4^{msm}$  symmetry. Here, we select  $|\psi_6^{msm}| \geq 0.5$  and  $|\psi_4^{msm}| \geq 0.6$  as the minimum threshold values for  $r$ -fold symmetry. In this figure the images from top-bottom (right) indicate histograms at increasing distances along the radial direction for the same experiment (whole substrate), showing that domains are not in phase along the radial direction like in OCP. Furthermore, in Fig. 7.17 we show a plot presenting  $\langle|\psi_6^{msm}|\rangle$  and  $\langle|\psi_4^{msm}|\rangle$  values for various experiments at increasing distance from the spinning center. This plot is discussed in detail in the following sections.

## Summary

In this study two methods are used to characterize order and disorder in colloidal monolayer structure obtained by spin-coating that include bond order parameters and Minkowski structure

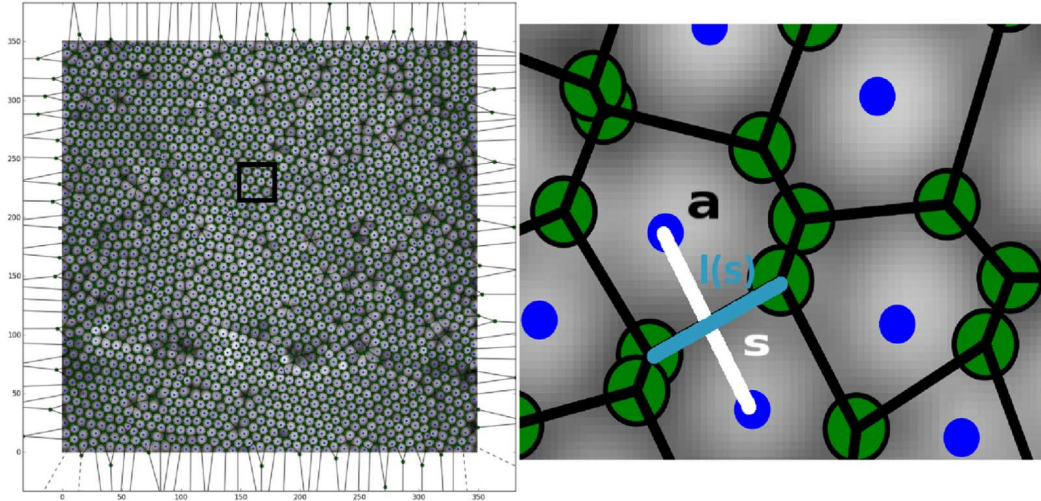


Figure 7.16: Voronoi diagram of AFM image obtained in the experiment using patterning substrate with the scaling spacing of 0.55 mm. Right: magnified portion of it (the small squared region). Here we show Voronoi cell for each particle  $a$ . Where,  $l(s)$  is the length between two neighboring vertices (green circles) of the Voronoi cell of particle  $a$  that corresponds to a given bond  $s$ . The field of view is 20  $\mu\text{m}$ .

metrics. These analysis methods present a unified strategy for comparing degree of structural order. Fig. 7.15, Fig. 7.14 and Fig. 7.17 show a comparison of structural order in colloidal monolayer based on these two kinds of analyses for various experiments. In Fig. 7.15-right we can observe more red columns that corresponds to the phase of 4-fold symmetry ( $\psi_4^{\text{msm}}$ ) than in Fig. 7.15-left ( $\psi_4$ ). Similarly, in Fig. 7.17 the absolute value of the correlation coefficient coming from the regression analysis (turquoise dashed line) for  $\langle|\psi_r^{\text{msm}}|\rangle$  is 0.991 which is higher than in Fig. 7.14 for  $\langle|\psi_r|\rangle$  i.e. 0.963. Our experimental results show that the bond orientational order parameters  $\psi_r$  given in eq. 7.11, which are the nearest neighbor bonds and are strongly influenced by the choice of neighborhood. Therefore, a well-known and robust structure metrics (msm) is proposed based on the geometry of the Voronoi cell definition according to eq. 7.12, removing the weaknesses found in bond network neighborhoods.

### 7.2.2. Effect of the scaling spacing geometry of patterning

We study the influence of the scaling spacing (the distance between the hexagonal pillars in Fig. 7.18) or the substrate surface properties on the behavior of spin-coated colloidal films by keeping the other experimental conditions unchanged. Next, we discuss two relevant aspects linked to the scaling spacing.

#### On the degree of order of structure

Series of experiments are performed on changing the scaling spacing (0.3, 0.55, 0.82, 1.09 mm: distances between hexagonal pillars), to obtain a better degree of order of structure. After,  $\langle\psi_r\rangle$  and  $\langle\psi_r^{\text{msm}}\rangle$  are measured for 4-fold and 6-fold regions separately. That are plotted as a function

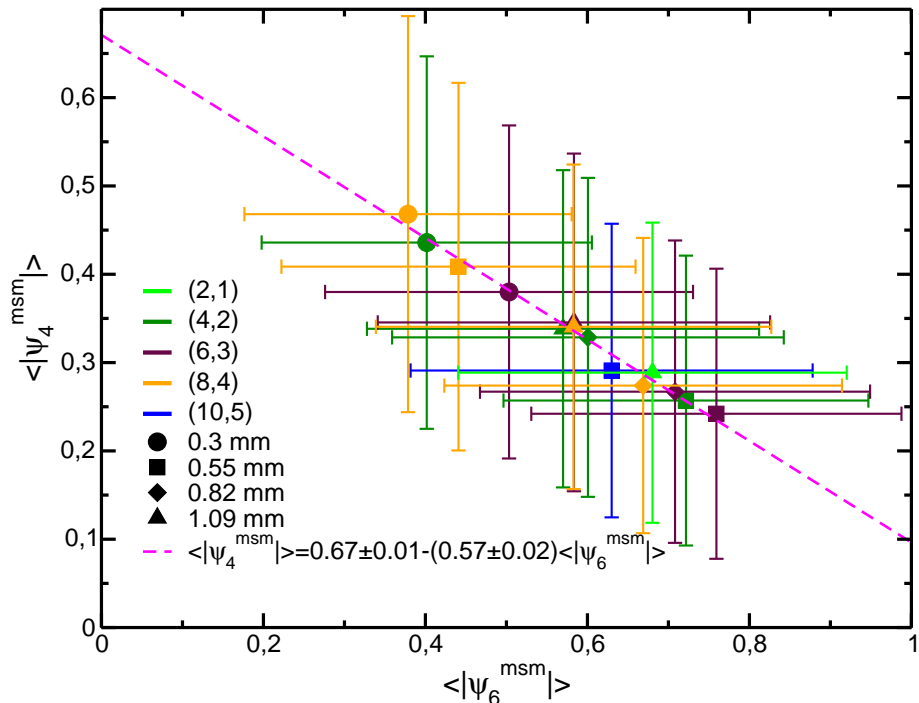


Figure 7.17: Average Minkowski structure metrics for  $\langle|\psi_6^{\text{msm}}|\rangle$  and  $\langle|\psi_4^{\text{msm}}|\rangle$  of each AFM image of spin-coated deposit, taken along the radial direction at different increasing distances from the center of spinning shown by lines in legend (e.g. (2,1)=2.24 mm, see Fig. 6.8 for details), and as a function of increasing spacing between hexagonal pillars (see symbols in legend). For the scaling spacing of 0.55–0.82 mm we have greater values for  $\langle|\psi_6^{\text{msm}}|\rangle$  and smaller for  $\langle|\psi_4^{\text{msm}}|\rangle$ . The turquoise dashed line shows the regression analysis result.

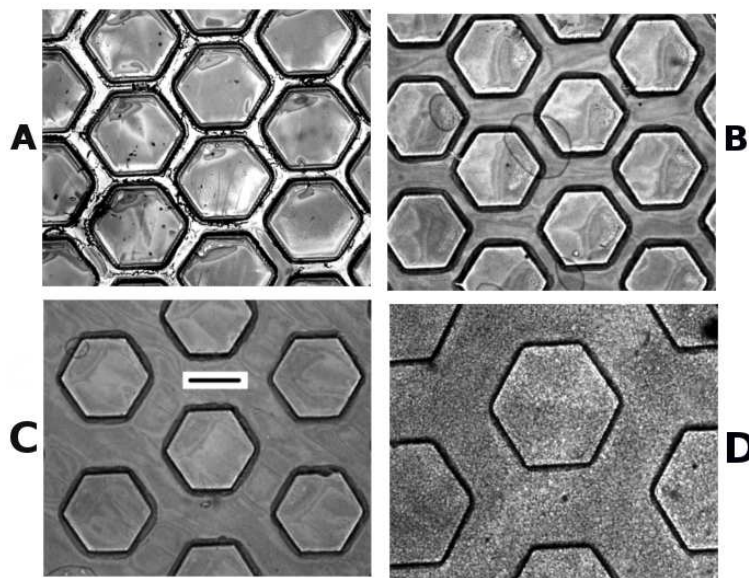


Figure 7.18: A–D are optical microscopic images of colloidal films, spin-coated at 3000 rpm on a photo-patterned substrate with SU–8 on hexagonal pillars of the same diagonal length (1.1 mm) and various scaling spacing (distances between hexagonal pillars), A=0.3 mm; B=0.55 mm; C=0.83 mm; D=1.09 mm. Deposit of silica particles of  $0.5 \mu\text{m}$  suspended in ethanol (solvent) on the patterned cover-slides. Scale bar for image (C) is 0.62 mm

of the scaling spacing and the distance from the center of spinning displayed in Fig. 7.14 and Fig. 7.17. These plots indicate that we have hexagonal and closed packed monolayer colloidal structure for the scaling spacing 0.55–0.82 mm which is in a good agreement with our experimental conditions.

### On the perimeter width

Also, we obtain optical microscopic magnified images of the spin-coated colloidal films on the patterned substrates (see Fig. 7.18). We observe an increase in the width of the perimeter (the deposited colloidal layer around each hexagonal pillar) for increasing the scaling spacing between the hexagonal pillar up to 0.55 mm and then starting to decrease for the larger spacing as shown in Fig. 7.19. This plot reveals that the perimeter width is a general function of the scaling spacing. Possibly, at higher spacing values the surface behaves as non-patterned substrate for drying suspension. Hence, the perimeter width also has strong dependence on the scaling spacing. The dependence of the perimeter thickness on the scaling spacing may be related to hydrodynamics or surface tension. Additional research is required to figure out this phenomenon in depth.

Further work is in progress to analyze in depth these structures with persistent homology using first Betti number of complex in collaboration with Prof. S. Ardanza-Trevijano. Also, more work has to be carried out to investigate the effect of other useful parameters such as: increasing the initial concentration of suspensions or the size of particle that can shed light on the knowledge concerning this phenomena.

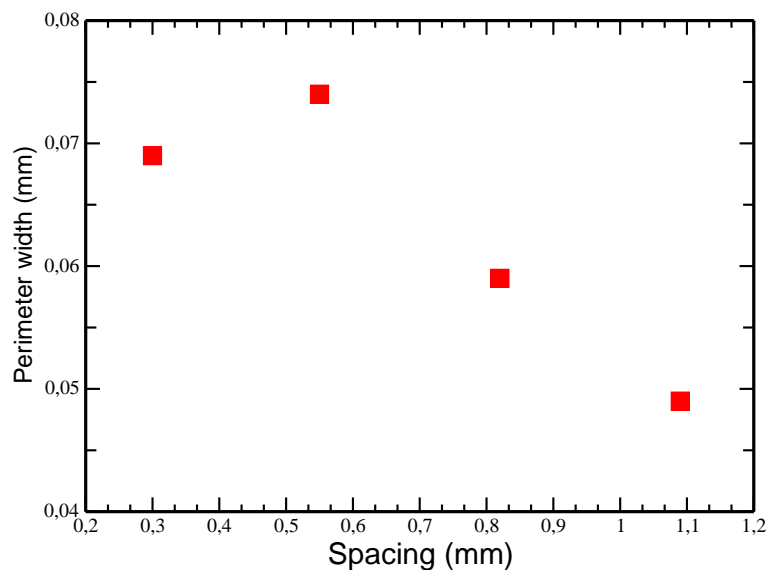


Figure 7.19: Perimeter width (the deposited colloidal layer around each hexagonal pillar) as a function of increasing scaling spacing between the hexagonal pillars.

# Conclusions and Outlook

## Conclusions

Experimental results on weak AC field-induced pattern formation in diluted colloids have been studied both at room temperature and at higher temperature using vertical deposition like configuration. Weak AC fields lead to the evolution of clusters at the interface at low evaporation and elongated columnar deposits are obtained at higher evaporation. The conclusions attained in this part at our experimental conditions are the following:

- A contact line on an electrode is required to obtain clusters. Thus the mechanism involved for clusters formation is electrowetting.
- Evaporation is needed to have clusters formation.
- PIV analysis prove that contact angle variation by electrowetting generates short ranged closed flows (in the affected basin of attraction) near the meniscus giving rise to instabilities and break the continuous translational symmetry to supply particles there for accumulation.
- The mean distance between clusters  $\bar{\lambda}$  increases monotonically with an increase in initial particle concentration.
- Clusters are not correlated with columns formation, i.e. clusters are not seeds for columns.
- At higher evaporation long range convective flows affect the colloidal deposition.
- External AC field keeps the connection of short ranged closed flows (in the affected basin of attraction) which provide more particles to obtain elongated columnar deposit.
- The width of the columns is associated with applied field strength.

The magnetic field-dependent viscosity of diluted ferromagnetic colloids is measured by spin-coating in magnetic field. We also make colloidal films using concentrated suspension of nonmagnetic colloidal particles by spin-coating technique on photo-patterned substrates.

- Magneto-rheological behavior of ferromagnetic-colloids can be studied by spin-coating.
- Hybrid colloids rheology can be characterized by spin-coating.
- Spin-coating of concentrated colloids on photo-patterned substrates breaks up the axial symmetry (eliminates the emergence of color arms).
- Polycrystals of monolayer on SU-8 coated pillars are obtained.

- Scaling spacing between pillars is a critical parameter to control the process of structure formation.
- Standard bond order parameter analysis is not enough for characterizing properly the structure. Minkowski structure metrics are giving more appropriate results.

## Outlook

It is clear that vertical deposition configuration in AC fields is a promising technique to obtain interesting colloidal patterns at various temperatures. It is required to continue the research to reach a complete understanding of the system. Thus, it would be interesting to perform further experiments to study quantitatively the effect of surface properties on the behaviour of clusters and columns formation.

In spin-coating experiments involving evaporation, we were able to develop a generalized model to extract the absolute thickness of dried deposit of hybrid colloid. It is also possible to obtain the behavior of evaporation as a function of  $\omega$  (spinning speed) in terms of occupation factor and shortly this work will be completed. Also, it would be interesting to investigate the effect of increasing initial particle concentration on the magneto-rheological behaviour of superparamagnetic colloids in magnetic fields and to study magnetorheology of magnetic colloids at very low  $\omega$  (50–500 rpm). For quantitative verification of our magnetorheological results of hybrid colloids obtained by spin-coating, it is necessary to appropriately compare these results with those obtained by classical rheometry. This work is performed in collaboration with Prof. Juan de Vicente and the manuscript based on those result is already submitted to **Smart Mater. Struct.** for publication. Some fundamental shortcomings were detected in the bond-orientational order parameters analysis that significantly affect their simplification to investigate the degree of order of disordered systems [4]. It is needed to introduce new methods to analyze these structures in dept with more accuracy. Therefore, research is being done in our group to quantify these structures with persistent homology using first Betti number of complex with Prof. S Ardanza-Trevijano and Prof. A. Yethiraj.

# Bibliography

- [1] R. Aslam, M. Pichumani, W. González-Viñas. *Weak ac field-induced patterns in vertical deposition of colloids at various evaporation rates.* Eur. Phys. J. Special Topics **224** (2), (2015), pp. 435–445.
- [2] C. Arcos, K. Kumar, W. González-Viñas, R. Sirera, K. M. Poduska, A. Yethiraj. *Orientationally correlated colloidal polycrystals without long-range positional order.* Phys. Rev. E **77**, (2008), p. 050402(R).
- [3] P. Bagheri, A. M. Almudallal, A. Yethiraj, K. M. Poduska. *Quantitative metrics for assessing positional and orientational order in colloidal crystals.* Langmuir **31** (30), (2015), pp. 8251–8259.
- [4] W. Mickel, S. C. Kapfer, G. E. Schröder-Turk, K. Mecke. *Shortcomings of the bond orientational order parameters for the analysis of disordered particulate matter.* Phys. Rev. E. **138** (4), (2013), p. 044501.
- [5] R. Williams, R. Crandall. *The structure of crystallized suspensions of polystyrene spheres.* Phys. Lett. A **48** (3), (1974), pp. 225–226.
- [6] E. Yablonovitch. *Inhibited spontaneous emission in solid-state physics and electronics.* Phys. Rev. Lett. **58** (20), (1987), p. 2059.
- [7] K. B. Blodgett. *Films built by depositing successive monomolecular layers on a solid surface.* J. Am. Chem. Soc. **57**, (1935), p. 1007.
- [8] E. Matijevic, R. J. Good. *Surface and colloid science*, vol. 12. Springer Science & Business Media (2012).
- [9] W. B. Russel, D. A. Saville, W. R. Schowalter. *Colloidal dispersions.* Cambridge university press (1992).
- [10] R. A. Jones. *Soft condensed matter*, vol. 6. Oxford University Press (2002).
- [11] H. Hamaker. *The London van der Waals attraction between spherical particles.* Physica **4** (10), (1937), pp. 1058–1072.
- [12] D. J. Shaw. *Introduction to colloid and surface chemistry.* Butterworths, London (1980).
- [13] H.-J. Butt, M. Kappl. *Electrostatic double-layer forces.* Surface and Interfacial Forces pp. 93–125.

- [14] H. Morgan, N. G. Green. *AC electrokinetics: colloids and nanoparticles*. 2. Research Studies Press (2003).
- [15] T. G. Van de Ven. *Colloidal hydrodynamics*. Academic Press (1989).
- [16] H. J. J. Verheijen, M. W. J. Prins. *Reversible electrowetting and trapping of charge: Model and experiments*. Langmuir **15** (20), (1999), pp. 6616–6620.
- [17] J. Hong, S. Ko, K. Kang, I. Kang. *A numerical investigation on ac electrowetting of a droplet*. Microfluidics and Nanofluidics **5** (2), (2008), pp. 263–271.
- [18] H. Lee, S. Yun, S. H. Ko, K. H. Kang. *An electrohydrodynamic flow in ac electrowetting*. Biomicrofluidics **3** (4), (2009), p. 044113.
- [19] F. Mugele, J.-C. Baret. *Electrowetting: from basics to applications*. J. Phys.: Condens. Matter **17** (28), (2005), p. R705.
- [20] M. Cowley, R. E. Rosensweig. *The interfacial stability of a ferromagnetic fluid*. J. Fluid Mech. **30** (04), (1967), pp. 671–688.
- [21] R. E. Rosensweig. *Magnetic fluids*. Sci. Amer. **247** (4), (1982), pp. 136–145.
- [22] R. Rosensweig. *Directions in ferrohydrodynamics*. J. Appl. Phys. **57** (8), (1985), pp. 4259–4264.
- [23] O. Lavrova, V. Polevikov, L. Tobiska. *Numerical study of the rozensweig instability in a magnetic fluid subject to diffusion of magnetic particles*. Mathematical Modelling and Analysis **15** (2), (2010), pp. 223–233.
- [24] J. Drelich, E. Chibowski, D. D. Meng, K. Terpilowski. *Hydrophilic and superhydrophilic surfaces and materials*. Soft Matter **7** (21), (2011), pp. 9804–9828.
- [25] A. S. Dimitrov, K. Nagayama. *Continuous convective assembling of fine particles into two-dimensional arrays on solid surfaces*. Langmuir **12**, (1996), p. 1303.
- [26] P. Jiang, J. F. Bertone, K. S. Hwang, V. L. Colvin. *Single-crystal colloidal multilayers of controlled thickness*. Chem. Mater. **11**, (1999), p. 2132.
- [27] C. Brinker, Y. Lu, A. Sellinger, H. Fan. *Evaporation-induced self-assembly: Nanostructures made easy*. Adv. Mater. **11** (7), (1999), pp. 579–585.
- [28] F. Meseguer. *Colloidal crystals as photonic crystals*. Colloids and Surfaces A: Physicochemical and Engineering Aspects **270**, (2005), pp. 1–7.
- [29] D. Liu, Y. Xiang, X. Wu, Z. Zhang, L. Liu, L. Song, X. Zhao, S. Luo, W. Ma, J. Shen, et al. *Periodic ZnO nanorod arrays defined by polystyrene microsphere self-assembled monolayers*. Nano Lett. **6** (10), (2006), pp. 2375–2378.
- [30] D. J. Norris, Y. A. Vlasov. *Chemical approaches to three-dimensional semiconductor photonic crystals*. Adv. Mater. **13**, (2001), pp. 371–376.

- [31] K. Davis, W. Russel, W. Glantschnig. *Settling suspensions of colloidal silica : Observations and X-ray measurements.* J. Chem. Soc. Faraday Trans. **87**, (1991), pp. 411–424.
- [32] H. Míguez, F. Meseguer, C. López, A. Mifsud, J. Moya, L. Vázquez. *Evidence of FCC crystallization of  $SiO_2$  nanospheres.* Langmuir **13**, (1997), pp. 6009–6011.
- [33] P. Segrè, F. Liu, P. Umbanhowar, D. Weitz. *An effective gravitational temperature for sedimentation.* Nature **409**, (2001), pp. 594–597.
- [34] M. Yoldi, C. Arcos, B.-R. Paulke, R. Sirera, W. González-Viñas, E. Görnitz. *On the parameters influencing the deposition of polystyrene colloidal crystals.* Materials Science and Engineering: C **28** (7), (2008), pp. 1038–1043.
- [35] M. Giuliani, W. González-Viñas. *Contact-line speed and morphology in vertical deposition of diluted colloids.* Phys. Rev. E **79** (3), (2009), p. 032401.
- [36] R. G. Shimmin, A. J. DiMauro, P. V. Braun. *Slow vertical deposition of colloidal crystals. A Langmuir Blodgett Process.* Langmuir **22** (15), (2006), pp. 6507–6513.
- [37] M. Giuliani, M. Pichumani, W. González-Viñas. *Impact of electric fields on the speed of contact line in vertical deposition of diluted colloids.* Eur. Phys. J. Special Topics **192**, (2011), p. 121.
- [38] M. Giuliani. *Colloidal crystal formation through interfacial mechanisms.* Ph.D. thesis, University of Navarra (2010).
- [39] H. Mancini, D. Maza. *Pattern formation without heating in an evaporative convection experiment.* EPL (Europhysics Letters) **66** (6), (2004), p. 812.
- [40] C. Buffone, K. Sefiane, J. Christy. *Experimental investigation of self-induced thermocapillary convection for an evaporating meniscus in capillary tubes using micro-particle image velocimetry.* Phys. Fluids **17** (5), (2005), p. 052104.
- [41] F. Doumenc, T. Boeck, B. Guerrier, M. Rossi. *Transient Rayleigh–Bénard–Marangoni convection due to evaporation: a linear non-normal stability analysis.* J. Fluid Mech. **648**, (2010), pp. 521–539.
- [42] D. C. Grahame. *The electrical double layer and the theory of electrocapillarity.* Chem. Rev. **41** (3), (1947), pp. 441–501.
- [43] J. H. Masliyah, S. Bhattacharjee. *Electrokinetic and colloid transport phenomena.* John Wiley & Sons (2006).
- [44] R. J. Hunter. *Zeta potential in colloid science: principles and applications*, vol. 2. Academic press (2013).
- [45] J. Melcher, G. Taylor. *Electrohydrodynamics: a review of the role of interfacial shear stresses.* Annu. Rev. Fluid Mech. **1** (1), (1969), pp. 111–146.
- [46] A. Castellanos. *Electrohydrodynamics*, vol. 380. Springer (2014).
- [47] D. Li. *Electrokinetics in microfluidics*, vol. 2. Academic Press (2004).

- [48] V. Lobaskin, B. Dünweg, C. Holm. *Electrophoretic mobility of a charged colloidal particle: a computer simulation study.* J. Phys.: Condens. Matter **16** (38), (2004), p. S4063.
- [49] T. Hao. *Electrorheological fluids: the non-aqueous suspensions*, vol. 22. Elsevier (2011).
- [50] Y. Solomentsev, S. A. Guelcher, M. Bevan, J. L. Anderson. *Aggregation dynamics for two particles during electrophoretic deposition under steady fields.* Langmuir **16** (24), (2000), pp. 9208–9216.
- [51] J. L. Anderson. *Colloid transport by interfacial forces.* Annual Review of Fluid Mechanics **21** (1), (1989), pp. 61–99.
- [52] A. Ramos, H. Morgan, N. G. Green, A. Castellanos. *AC electric-field-induced fluid flow in microelectrodes.* J. Colloid Interface Sci. **217** (2), (1999), pp. 420–422.
- [53] N. G. Green, A. Ramos, A. González, H. Morgan, A. Castellanos. *Fluid flow induced by nonuniform ac electric fields in electrolytes on microelectrodes. i. experimental measurements.* Phys. Rev. E **61** (4), (2000), p. 4011.
- [54] E. B. Longquan Chen. *Electrowetting, from statics to dynamics.* Adv. Colloid Interface Sci. **210**, (2014), pp. 2–12.
- [55] A. Quinn, R. Sedev, J. Ralston. *Influence of the electrical double layer in electrowetting.* J. Phys. Chem. B **107** (5), (2003), pp. 1163–1169.
- [56] X. Li, G. He, X. Zhang. *Numerical simulation of drop oscillation in ac electrowetting.* Science China Physics, Mechanics and Astronomy **56** (2), (2013), pp. 383–394.
- [57] Octave community. *GNU Octave 3.8.1* (2014).
- [58] M. Raffel. *Experimental fluid mechanics, a practical guid to particle image velocimetry.* Springer publisher in Germany .
- [59] M. Lopez-Caballero. *Large scales in a turbulent von Kármán swirling flow.* Ph.D. thesis, University of Navarra (2013).
- [60] M. Jahanmiri. *Particle image velocimetry: Fundamentals and its applications.* Tech. rep., Chalmers University of Technology (2011).
- [61] H. Hu, T. Saga, T. Kobayashi, K. Okamoto, N. Taniguchi. *Evaluation of the cross correlation method by using PIV standard images.* Journal of Visualization **1** (1), (1998), pp. 87–94.
- [62] M. Pichumani, M. Giuliani, W. González-Viñas. *One-dimensional cluster array at the three-phase contact line in diluted colloids subjected to ac electric fields.* Phys. Rev. E **83** (4), (2011), p. 047301.
- [63] Y. Hu, J. Glass, A. Griffith, S. Fraden. *Observation and simulation of electrohydrodynamic instabilities in aqueous colloidal suspensions.* J. Chem. Phys. **100** (6), (1994), pp. 4674–4682.
- [64] E. Schäffer, T. Thurn-Albrecht, T. P. Russell, U. Steiner. *Electrohydrodynamic instabilities in polymer films.* EPL (Europhysics Letters) **53** (4), (2001), p. 518.

- [65] S. H. Ko, H. Lee, K. H. Kang. *Hydrodynamic flows in electrowetting*. Langmuir **24** (3), (2008), pp. 1094–1101.
- [66] M. K. Chaudhury. *Interfacial interaction between low-energy surfaces*. Materials Science and Engineering: R: Reports **16** (3), (1996), pp. 97–159.
- [67] Y. Han. *Colloidal electrodynamics, electrohydrodynamics and thermodynamics in confined geometries*. Ph.D. thesis, The University of Chicago (2003).
- [68] D. R. Lide. *CRC Handbook of Chemistry and Physics, internet Version 2007*. CRC Press/Taylor and Francis, Boca Raton, FL **87**.
- [69] D. Hou, H.-C. Chang. *Electrokinetic particle aggregation patterns in microvortices due to particle-field interaction*. Phys. Fluids **18**, (2006), p. 071702.
- [70] L. Meng, H. Wei, A. Nagel, B. J. Wiley, L. E. Scriven, D. J. Norris. Nano Lett. **6**, (2006), p. 2249.
- [71] M. Pichumani. *Effect of External Fields on the Dynamics of Colloidal Phase Transitions*. Ph.D. thesis, University of Navarra (2013).
- [72] R. Lenormand, E. Touboul, C. Zarcone. *Numerical models and experiments on immiscible displacements in porous media*. J. Fluid Mech. **189**, (1988), pp. 165–187.
- [73] P. H. Walker, J. G. Thompson. *Some physical properties of paints*. P. Am. Soc. Test. Mater. **22**, (1922), p. 465.
- [74] A. G. Emslie, F. T. Bonner, L. G. Peck. *Flow of a viscous fluid on a rotating disk*. J. Appl. Phys. **29**, (1958), pp. 858–862.
- [75] D. Meyerhofer. *Characteristics of resist films produced by spinning*. J. Appl. Phys. **49** (7), (1978), pp. 3993–3997.
- [76] T. Rehg, B. Higgins. *Spin coating of colloidal suspensions*. AIChE J. **38**, (1992), p. 489.
- [77] D. P. Birnie III, M. Manley. *Combined flow and evaporation of fluid on spinning disk*. Phys. of Fluids **9** (4), (1997), pp. 870–875.
- [78] A. Acrivos, M. J. Shah, E. E. Petersen. *On the flow of a non-newtonian liquid on a rotating disk*. J. Appl. Phys. **31** (6), (1960), p. 963.
- [79] S. Wahal, A. Oztekin, D. E. Bornside, R. A. Brown, P. K. Seidel, P. W. Ackmann, F. T. Geyling. *Visualization of a gas flow instability in spin coating systems*. Appl. Phys. Lett. **62** (20), (1993), p. 2584.
- [80] H. Furukawa, H. Tsutsui, K. Aoi, T. Watanabe, I. Nakamura. *Visual study of variations of flow patterns around a disk in a casing: effects of edge of the disk*. J. Phys.: Conference Series **14** (14), (2005), pp. 220–227.
- [81] D. E. Bornside, C. W. Macosko, L. E. Scriven. *Spin coating: One-dimensional model*. J. Appl. Phys. **66** (11), (1989), pp. 5185–5193.

- [82] D. B. Hall, P. Underhill, J. M. Torkelson. *Spin coating of thin and ultrathin polymer films.* Polym. Eng. Sci. **38** (12), (1998), pp. 2039–2045.
- [83] N. Fraysse, G. M. Homsy. *An experimental-study of rivulet instabilities in centrifugal spin-coating of viscous Newtonian and non-Newtonian fluids.* Phys. Fluids **6**, (1994), p. 1491.
- [84] T. Ohara, Y. Matsumoto, H. Ohashi. *The film formation dynamics in spin coating.* Phys. of Fluids A **1** (12), (1989), pp. 3993–3997.
- [85] V. Cregan, S. O'Brien. *A note on spin-coating with small evaporation.* J. Colloid Interf. Sci. **314**, (2007), p. 324.
- [86] A. Mihi, M. Ocaña, H. Míguez. *Oriented colloidal-crystal thin films by spin-coating micro-spheres dispersed in volatile media.* Adv. Mater. **18**, (2006), pp. 2244–2249.
- [87] N. Sahu, B. Parija, S. Panigrahi. *Fundamental understanding and modeling of spin coating process: A review.* Indian J. Phys. **83** (4), (2009), pp. 493–502.
- [88] D. E. Bornside, R. A. Brown, P. W. Ackmann, J. R. Frank, A. A. Tryba, F. T. Geyling. *The effects of gas phase convection on mass transfer in spin coating.* J. Appl. Phys. **73** (2), (1993), pp. 585–600.
- [89] C.-C. Chang, C.-L. Pai, W.-C. Chen, S. A. Jenekhe. *Spin coating of conjugated polymers for electronic and optoelectronic applications.* Thin Solid Films **479** (1), (2005), pp. 254–260.
- [90] T. Komikado, A. Inoue, K. Masuda, T. Ando, S. Umegaki. *Multi-layered mirrors fabricated by spin-coating organic polymers.* Thin Solid Films **515** (7), (2007), pp. 3887–3892.
- [91] Y. L. Wu. *Control over colloidal crystallization by shear and electric fields.* Ph.D. thesis, Utrecht University (2007).
- [92] S. Middleman. *The effect of induced air-flow on the spin coating of viscous liquids.* J. Appl. Phys. **62** (6), (1987), pp. 2530–2532.
- [93] S. Wilson, R. Hunt, B. Duffy. *The rate of spreading in spin coating.* J. Fluid Mech. **413**, (2000), pp. 65–88.
- [94] B. G. Higgins. *Film flow on a rotating disk.* Phys. Fluids **29** (11), (1986), p. 3522.
- [95] M. Pichumani, W. González-Viñas. *Magnetorheology from surface coverage of spin-coated colloidal films.* Soft Matter **9** (8), (2013), pp. 2506–2511.
- [96] S. A. Jenekhe, S. B. Schuldt. *Coating flow of non-newtonian fluids on a flat rotating disk.* Industrial & engineering chemistry fundamentals **23** (4), (1984), pp. 432–436.
- [97] P. Jiang, M. J. McFarland. *Large-scale fabrication of wafer-size colloidal crystals, macro-porous polymers and nanocomposites by spin-coating.* J. Am. Chem. Soc. **126**, (2004), pp. 13778–13786.
- [98] L. Shereda, R. Larson, M. Solomon. *Local stress control of spatiotemporal ordering of colloidal crystals in complex flows.* Phys. Rev. Lett. **101**, (2008), p. 038301.

- [99] G. A. Ozin, S. M. Yang. *The race for the photonic chip: colloidal crystal assembly in silicon wafers.* Adv. Funct. Mater. **11** (2), (2001), pp. 95–104.
- [100] D. Xia, S. Brueck. *A facile approach to directed assembly of patterns of nanoparticles using interference lithography and spin coating.* Nano Lett. **4** (7), (2004), pp. 1295–1299.
- [101] D. Xia, S. Brueck. *Lithographically directed deposition of silica nanoparticles using spin coating.* J. Vac. Sci. Technol., B **22** (6), (2004), pp. 3415–3420.
- [102] M. Giuliani, W. González-Viñas, K. M. Poduska, A. Yethiraj. *Dynamics of crystal structure formation in spin-coated colloidal films.* J. Phys. Chem. Lett. **1** (9), (2010), pp. 1481–1486.
- [103] T. Ogi, L. B. Modesto-Lopez, F. Iskandar, K. Okuyama. *Fabrication of a large area monolayer of silica particles on a sapphire substrate by a spin coating method.* Colloids Surf., A: Physicochemical and Engineering Aspects **297** (1), (2007), pp. 71–78.
- [104] M. Pichumani, P. Bagheri, K. M. Poduska, W. González-Viñas, A. Yethiraj. *Dynamics, crystallization and structures in colloid spin coating.* Soft Matter **9** (12), (2013), pp. 3220–3229.
- [105] A. P. Bartlett, M. Pichumani, M. Giuliani, W. González-Viñas, A. Yethiraj. *Modified spincoating technique to achieve directional colloidal crystallization.* Langmuir **28**, (2012), p. 3067.
- [106] M. Pichumani, M. Giuliani, W. González-Viñas. *One-dimensional cluster array at the three-phase contact line in diluted colloids subjected to ac electric fields.* Phys. Rev. E **83** (4), (2011), p. 047301.
- [107] P. Pusey, W. Van Megen, P. Bartlett, B. Ackerson, J. Rarity, S. Underwood. *Structure of crystals of hard colloidal spheres.* Phys. Rev. Lett. **63** (25), (1989), p. 2753.
- [108] B. J. Ackerson, N. A. Clark. *Shear-induced melting.* Phys. Rev. Lett. **46** (2), (1981), p. 123.
- [109] D. Derks, Y. L. Wu, A. van Blaaderen, A. Imhof. *Dynamics of colloidal crystals in shear flow.* Soft Matter **5** (5), (2009), pp. 1060–1065.
- [110] J. de Vicente, D. J. Klingenberg, R. Hidalgo-Alvarez. *Magnetorheological fluids: a review.* Soft Matter **7** (8), (2011), pp. 3701–3710.
- [111] R. Rowe. *Interactions in the ternary powder system microcrystalline cellulose, magnesium stearate and colloidal silica, a solubility parameter approach.* Int. J. Pharm. **45** (3), (1988), pp. 259–261.
- [112] C. M. Hansen. *The universality of the solubility parameter.* Product R&D **8** (1), (1969), pp. 2–11.
- [113] J. C. Ulicny, A. L. Smith, M. A. Golden, C. A. Hayden. *Magnetorheological fluids with stearate and thiophosphate additives* (2005). US Patent 6,881,353.

- [114] A. F. Barton. *CRC handbook of solubility parameters and other cohesion parameters*. CRC press (1991).
- [115] M. J. McDonald, A. Yethiraj, L. Y. Beaulieu. *A method to characterize structure and symmetry in low-resolution images of colloidal thin films*. Meas. Sci. Technol. **23**, (2012), p. 045606.
- [116] E. Metwalli, D. Haines, O. Becker, S. Conzone, C. Pantano. *Surface characterizations of mono-, di-, and tri-aminosilane treated glass substrates*. J. Colloid Interface Sci. **298** (2), (2006), pp. 825–831.
- [117] P. P. Phule. *Magnetorheological fluid* (1999). US Patent 5,985,168.
- [118] M. Pichumani, W. González-Viñas. *Spin-coating of dilute magnetic colloids in a magnetic field*. Magnetohydrodynamics **47**, (2011), pp. 191–199.
- [119] P. Ilg, M. Kröger, S. Hess. *Magnetoviscosity of semidilute ferrofluids and the role of dipolar interactions: Comparison of molecular simulations and dynamical mean-field theory*. Phys. Rev. E **71**, (2005), p. 031205.
- [120] N. J. Wagner, J. F. Brady. *Shear thickening in colloidal dispersions*. Phys. Today **62**, (2009), p. 27.
- [121] X. Cheng, J. H. McCoy, J. N. Israelachvili, I. Cohen. *Imaging the microscopic structure of shear thinning and thickening colloidal suspensions*. Science **333**, (2011), p. 1276.
- [122] D. J. Norris, Y. A. Vlasov. *Chemical approaches to three-dimensional semiconductor photonic crystals*. Adv. Mater. **13**, (2001), pp. 371–376.
- [123] P. V. Braun, P. Wiltzius. *Microporous materials: Electrochemically grown photonic crystals*. Nature **402** (6762), (1999), pp. 603–604.
- [124] J. D. Joannopoulos. *Photonics: Self-assembly lights up*. Nature **414** (6861), (2001), pp. 257–258.
- [125] J. J. Juarez, M. A. Bevan. *Interactions and microstructures in electric field mediated colloidal assembly*. J. Chem. Phys. **131** (13), 134704.
- [126] S. van der Walt, J. L. Schönberger, the scikit-image contributors. *scikit-image: image processing in Python*. PeerJ **2**, (2014), p. e453.
- [127] S. C. Kapfer, W. Mickel, K. Mecke, G. E. Schröder-Turk. *Jammed spheres: Minkowski tensors reveal onset of local crystallinity*. Phys. Rev. E **85** (3), (2012), p. 030301.

# Index

- AC electrowetting, 13  
Atomic Force Microscopy (AFM), 59  
  
Basin of attraction, 32, 33  
Brownian force, 1  
  
Capillary number, 8  
Carbonyl iron particles, 53  
Characteristic length  $\bar{\lambda}$ , 18, 25, 34  
Cluster, 27, 34  
Columnar deposits, 35  
Compact equivalent height (CEH), 68, 70  
  
DLVO theory, 2  
Dynamic Light Scattering (DLS), 54  
  
Electric double-layer, 2, 9  
Electro-osmosis, 11  
Electrokinetic characterization, 18  
Electrokinetics, 9  
Electrophoresis, 10  
Electrophoretic effect, 31  
Electrowetting, 2  
Electrowetting effect, 32  
Electrowetting theory, 12  
Evaporation, 8  
Evaporation characterization, 19  
  
Gaussimeter, 56  
  
Hall effect, 56  
Helmholtz coils, 56  
Hybrid colloids, 64  
Hydrophilic substrates, 4, 59  
Hydrophobic substrates, 4, 61  
  
ITO substrates, 15  
  
Local bond order parameters, 75
- London-Van der Waals, 2  
Long term flows, 22, 33  
  
Magnetic field, 57  
Magnetoviscosity, 70  
Minkowski structure metrics, 78  
Mixed colloidal particles Suspension, 53  
  
Occupation factor, 64  
  
Péclet number, 8  
Photo-patterning, 58  
Piranha solution, 54  
PIV, 19  
PIV analysis, 27  
  
Reynolds number, 8  
Rosensweig instability, 3  
  
Short term flows, 22, 28  
Silanization, 61  
Spin-coater, 56, 59  
Substrates, 54  
Suspension, 15, 59  
  
Unit conversion, 18  
  
Vertical Deposition-like Configuration, 7  
Voronoi, 79



## Summary

In this work, we present experimental observations on the colloidal phase transitions (from liquid phase to solid phase) involving evaporation at different time scales. Two experimental setups have been used: vertical deposition configuration (large duration and low evaporation) and spin-coating (short duration and high evaporation) to carry out various research objectives.

(a) We study patterns formation in vertical deposition of colloids on applying weak AC fields at various temperatures. Diluted suspension of negatively charged polystyrene particles of  $1.3\text{ }\mu\text{m}$  in diameter suspended in ultra pure water are used to perform several experiments at different evaporation in external weak AC fields ( $0.8\text{ V/mm}$  to  $1.2\text{ V/mm}$  and of frequency from  $1\text{ Hz}$  to  $3\text{ Hz}$ ). At room temperature the application of AC field leads to the formation of one dimensional clusters array at the interface. The dynamical flows of the system during clusters formation in external AC fields have been studied by PIV analysis. Also, we demonstrate the effect of increasing initial particle concentration ( $0.5\%$  to  $1.1\%$  (w/w)) on the clusters evolution. At higher temperature ( $63\text{ }^{\circ}\text{C}$ ) we obtain ordered columnar deposits of these colloidal suspensions in AC fields. We study the effect of field strengths on the behavior of columns formation.

(b) We obtain polycrystals of mono-layer on photo-patterned substrates by spin-coating using concentrated colloidal suspension of  $458\text{ nm}$  diameter silica spheres dispersed in ethanol 95% of 20% (V/V) concentration. We break the axial symmetry imposed by spin axis and eliminate the emerging OCP character (6- or 4-arms). The effect of scaling spacing of surface patterning on the different structures formation of the spin-coated deposits has been studied extensively. We analyze the different structures in depth with bond order parameters and with Minkowski structure metrics. Also, we investigate the influence of external magnetic fields on the flow dynamics of mixed colloidal particles suspension (carbonyl iron and silica particles of micrometer size) by spin-coating and to manipulate the magneto-rheology in terms of occupation factor of the resulting deposits. We develop a generalized model by modifying Cregan and O'Brien model [85] to measure the change in relative viscosity of the mixed colloids in magnetic fields.

## Resumen

En este trabajo experimental, se presentan observaciones experimentales en transiciones de fase coloidales (de estado líquido a sólido) donde la evaporación a diversas escalas es relevante. Se han usado dos sistemas experimentales bien diferenciados: una configuración tipo deposición vertical (evaporación relativamente baja y larga duración del experimento) y “spin-coating” (alta evaporación y corta duración del experimento) para alcanzar los objetivos propuestos en esta tesis.

(a) Se estudia la formación de patrones en la deposición vertical de coloides a varias temperaturas con campo eléctrico alterno aplicado. Se utiliza una suspensión acuosa diluida de partículas de poliestireno de  $1.3\text{ }\mu\text{m}$  de diámetro cargadas negativamente para llevar a cabo experimentos con campos débiles y muy lentamente variables ( $0.8\text{ V/mm}$  a  $1.2\text{ V/mm}$  y con frecuencias de  $1\text{ Hz}$  a  $3\text{ Hz}$ ). A temperatura ambiente, la aplicación de los campos eléctricos citados da lugar a la formación de un arreglo unidimensional de agregados de partículas (“clusters”) cerca de la linea de contacto. Se han estudiado los flujos que aparecen en el sistema durante la formación y evolución de los agregados anteriormente nombrados mediante análisis de PIV. Además, se demuestra el efecto que tiene la concentración de partículas inicial ( $0.5\%$  a  $1.1\%$  (m/m)) en dicha evolución. A mayor temperatura ( $63\text{ }^{\circ}\text{C}$ ), pero con campo se obtienen depósitos de tipo columnata. Se ha estudiado el efecto de la intensidad del campo en el comportamiento de los depósitos obtenidos.

(b) Se obtienen monocapas policristalinas, sobre sustratos fotolitografiados, de suspensiones etanólicas ( $95\%$ ) coloidales de partículas de sílice con un diámetro de  $458\text{ nm}$  a concentración media ( $20\%$  (V/V)). El patrón que forma el sustrato rompe la simetría axial del sistema y evita la aparición de la estructura policristalina correlacionada orientacionalmente (OCP) que da lugar a la aparición de cuatro o seis brazos por reflexión de luz. El efecto de las distancias características del patrón sobre los depósitos por “spin-coating” ha sido estudiado extensivamente. Se caracterizan las estructuras a través del parámetro de orden de ligadura (“bond”) con una métrica estructural de Minkowski. Además se estudia la magnetohidrodinámica de una suspensión coloidal híbrida (Hierro carbonilo y sílice de tamaños micrométricos) por “spin-coating” y se obtienen las propiedades magnetorreológicas en función del factor de ocupación en los depósitos resultantes. Se desarrolla un modelo generalizado modificando el obtenido por Cregan y O’Brien [85] para medir el efecto de la viscosidad relativa de coloides híbridos con campos magnéticos.

